Fullerenes for Single Molecule Electronics

Gregory Ian Michael Rogers

Supervised by

Prof. G. Andrew D. Briggs, Prof. Kyriakos Porfyrakis and Dr.

Edward A. Laird

A thesis presented for the degree of

Doctor of Philosophy

Department of Materials

Wolfson College

University of Oxford

March 2017

Abstract

Fullerenes have a number of unique properties that make them interesting for use in molecular electronics. They are readily functionalized to produce a wide range of physical and chemical properties as well as creating a number of methods by which they can be combined with an electrode for electron transport. Fullerenes are also able to encapsulate atoms or clusters of atoms to further expand their properties, leading to a number of materials which show huge potential for applications in the field of quantum information. In particular the endohedral fullerene $N@C_{60}$ shows one of the longest coherence lifetimes of any molecular system, making it an ideal candidate for a qubit.

This thesis presents one method of functionalising fullerenes for combining their many attractive electronic properties with those of graphene. These functionalized fullerenes display a number of interesting properties in their own right. In particular, they show the possibility to selectively quench or sensitise the formation of singlet oxygen, which has dramatic implications for the use of fullerenes in medical applications. Electron transport measurements of the fullerene show excited vibrational states which confirm the presence of fullerene molecules. Finally, the presence of long-lived vibrational states makes fullerenes appealing for use in thermoelectrics, which is studied in detail.

Declaration

The material contained within this thesis has not previously been submitted for a degree at the University of Oxford or any other university. The research reported within this thesis has been conducted by the author unless indicated otherwise.

Publications

The publications containing material presented in this thesis are as follows:

Chapter 1

"Endohedral metallofullerenes: optical properties and biomedical applications", P. Dallas, I. Rasovic, **G. Rogers** and K. Porfyrakis in "Carbon Nanomaterials Sourcebook Vol. 1", Ed. by K. Sattler, Taylor & Francis, 2016, ISBN-13: 978-1482252682.

Chapter 3

"Charge separated states and singlet oxygen generation of mono and bis adducts of C_{60} and C_{70}", P. Dallas*, **G. Rogers***, B. Reid, R. Taylor, H. Shinohara, G. A. D. Briggs and K. Porfyrakis, Chem. Phys., 2016, 465, 28-39.

Chapter 4

"Sensitive Radio-Frequency Measurements of a Quantum Dot by Tuning to Perfect Impedance Matching", N. Ares, F. J. Schupp, A. Mavalankar, **G. Rogers**, J. Griffiths, G. A. C. Jones, I. Farrer, D. A. Ritchie, C. G. Smith, A. Cottet, G. A. D. Briggs and E. A. Laird, Physical Review Applied, 2016, 5(3), 034011.

Chapter 5

"Redox-dependent Franck-Condon blockade and avalanche transport in a graphene-fullerene nanoelectromechanical oscillator", C. S. Lau, H. Sadeghi, **G. Rogers**, S. Sangtarash, P. Dallas, K. Porfyrakis, J. Warner, C. Lambert, G. A. D. Briggs and J. Mol, Nano Letters, 2016, 16 (1), 170-176.

"Field-Effect Control of Graphene–Fullerene Thermoelectric Nanodevices", P. Gehring, A. Harzheim, J. Spièce, Y. Sheng, **G. Rogers**, C. Evangeli, A. Mishra, B. J. Robinson, K.s Porfyrakis, J. H. Warner, O. V. Kolosov, G. A. D. Briggs and J. A. Mol. Nano Letters, 2017, 17 (11), 7055-7061.

* These authors contributed equally.

Acknowledgements

I would like to use this space to thank everyone who has supported me throughout the course of my D. Phil project. In particular I would like to thank my loving partner Suzanne Jones for supporting me in this adventure and for keeping us both sane all the way to the end. I also would like to thank my friends and family for all of the help and support that they have given me.

I have had several supervisors for this project and would like to extend my thanks to all of them. Prof. Kyriakos Porfyrakis has been immensely helpful and supportive of my research, allowing me to grow as an academic from someone with very little experience in organic chemistry prior to this project. I would also like to thank Dr. Edward Laird for his help with the electronics side of the project and Prof. Andrew Briggs for his insightful advice. I have also had the pleasure of working with several other students and post-doctoral researchers, without whom this project would have been impossible. I extend my thanks to Dr. Panos Dallas for his assistance with fullerene chemistry and photochemistry and Dr. Maria Lebedeva for help with interpreting NMR spectra and electrochemistry. I would also like to thank Dr. Jan Mol for his support of my work and allowing the molecules that I have produced to be used in combination with the graphene nano-gaps that he pioneers and his groups are experts in. I would particularly like to thank Dr. Aaron Lau for taking the measurements that are seen in Chapter 5 on my molecules in graphene devices and Dr. Natalia Ares for measuring GaAs

quantum dots with my electronic circuits.

Finally I would like to thank EPSRC for providing the funding which has made this project possible.

Contents

1 Introduction

1.1 Fullerenes

Fullerenes are a class of carbon nanomaterials that, in combination with bulk materials, graphene and carbon nanotubes, constitute the full range of carbon allotropes. Just as carbon nanotubes can be imagined by rolling graphene sheets into a tube, fullerenes can be imagined by scrunching graphene sheets into a ball and were first discovered in the soot from laser vapourised graphite Kroto Full. Fullerenes can now be produced in a range of sizes and with a range of encapsulated atoms or clusters of atoms to produce the materials known as endohedral fullerenes. Between the different fullerene cage sizes and encapsulated atoms it is possible to observe a range of different properties and reactivities.

1.1.1 Reactivity

The reactivity of fullerenes was first studied in the more abundant empty cage fullerenes, primarily C_{60}. This has led to the discovery of a range of chemical pathways to functionalize the outside of the fullerene, which is known as exohedral funtionalization, to incorporate a wide range of chemical functionality into the molecules. The most common methods of fucntionalizing the fullerene cage are the Prato reaction[2], Bingel-Hirsch reaction[3] and Diels-Alder reaction[4], all of which can be extended to endohedral fullerenes. However, some endohedral fullerenes display additional reactions compared to the empty cage fullerenes,

while others are inert to reactions that take place with empty cages.

A reaction which highlights the different reactivities of different endohedral cages in addition to the difference between endohedral cages and empty cages is the photochemical disilylation reaction. The first successful functionalization of an endohedral fullerene was carried out by this reaction in 1995[5], during which the fullerene La@C_{82} was reacted with a disilirane, see Figure 1 a. This resulted in the formation of a monoadduct under illumination from a tungsten-halogen lamp, as had been observed with empty cage fullerenes. However, the reaction was also found to proceed when the reactants were heated to 80°C, which is not observed with the empty cage fullerenes. This is explained by looking at the redox potentials of La@C_{82} and noting that it is both a stronger electron donor and acceptor than the empty cage fullerenes due to its first oxidation and reduction potentials, see Table 1.

It was later shown that cations of the endohedral fullerenes M@$C_{82}{}^{+}$ (M = Y, La, Ce) would react with the disilirane at room temperature in darkened conditions while anions would not react with disilirane at elevated temperatures or under photochemical excitation [6].

The Bingle-Hirsch reaction was first performed on an endohedral fullerene in 1999, where solutions of the fullerene and diethyl bromomalonate were reacted with sodium hydride at room temperature, yielding a monoadduct [7]. However, the first fullerene functionalized in this way for a specific application was the

Molecule	$^{Ox}E_1$/ eV	$^{Red}E_1$/ eV	Thermal activity with disilirane	Photochemical activity with disilirane
C_{60}	+1.21	-1.12	N	Y
C_{70}	+1.19	-1.09	N	Y
$N@C_{2v}$-C_{60}	+1.21	-1.12	N	Y
$Y@C_{2v}$-C_{82}	+0.07	-0.42	Y	Y
$[Y@C_{2v}$-$C_{82}]+$	+1.07	+0.10	Y	Y
$[Y@C_{2v}$-$C_{82}]-$	-0.37	-1.34	N	N
$L@C_{2v}$-C_{82}	+0.08	-0.41	Y	Y
$Ce@C_{2v}$-C_{82}	+0.07	-0.39	Y	Y
$Gd@C_{2v}$-C_{82}	+0.09	-0.39	Y	Y
$La_2@I_h$-C_{80}	+0.22	-0.36	Y	Y
$Sc_3N@I_h$-C_{80}	+0.62	-1.22	N	Y
$Sc_2C_2@C_{3v}$-C_{80}	+0.16	-0.95	N	Y

Table 1: Redox potentials (V vs. Fc+/Fc) and reactivity with disilirane for various fullerenes and endohedral fullerenes [6].

addition of malonate groups, which were subsequently hydrolysed to carboxylic acid groups, to solubilise the fullerene $Gd@C_{60}$ for use as an MRI contrast agent. In this reaction $Gd@C_{60}$ was reacted with an excess of diethyl bromomalonate and different alkali metal hydrides in THF to add up to ten malonate groups, which were confirmed by mass-spectroscopy. These could then be hydrolysed to produce the water soluble $Gd@C_{60}(C(CO_2H)_2)_{10}$ [8]. Until recently, the Bingel-Hirsch reaction has been unsuitable for the functionalization of $N@C_{60}$ due to the high degree of spin loss, indicating that the nitrogen atom is escaping the fullerene cage. However, successful Bingel-Hirsch reactions on $N@C_{60}$ which retain in excess of 90% of the spin signal, as measured by EPR spectroscopy, have recently been reported [9]. This result was achieved by using a stoichiometric ratio of diluted DBU as a base, see Figure 1 b. A mechanism was also proposed for the escape of the nitrogen atom from the fullerene cage [9].

The first successful functionalization of a trinitide templated (TNT) endohedral fullerene was performed in 2002 using the Diels-Alder reaction [10]. In this reaction $Sc_3N@C_{80}$ was refluxed in TCB with an excess of 99% ^{13}C labelled 6,7-dimethoxyisochroman-3-one, yielding a single monoadduct, see Figure 1 c. ^{13}C nuclear magnetic resonance showed that the methylene carbons were in identical environments, while ^{1}H spectra showed that the protons were not, implying a symmetry plane passing through the pyrrolidine ring and therefore that the reaction took place on a [5,6] ring of the I_h isomers of $Sc_3N@C_{80}$. X-ray crystallography showed that the Sc_3N cluster was displaced away from the addition side, showing that the cluster has some influence on the reactivity of the cage [10].

When looking at purely metallic endohedral fullerenes, it is possible to note several interesting discrepancies from the TNTs. To typify these differences we select the reaction between $La@C_{82}$ and cyclopentadiene, see Figure 1 d [11]. In this reaction, an excess of cyclopentadiene was added to a degassed solution of $La@C_{82}$ in toluene, allowing the room temperature reaction to be monitored by EPR, showing the formation of a single monoadduct with a yield of 44%. The retro-Diels-Alder reaction also occurs at room temperature in this system, in contrast with C_{60} which must be heated. The fact that purely metallic endohedral fullerenes are more reactive in the Diels-Alder reaction than TNT endohedral fullerenes has been used to assist in the purification of TNT endohedral fullerenes from mixed fullerene soot [12].

The final reaction to be discussed is the one used to functionalize fullerenes in this thesis, the 1,3-diploar cycloaddition reaction, which is often known as the Prato reaction, as it was the work of Prato et. al that first showed the reaction could be applied to fullerenes, see Figure 1 e [2]. The Prato reaction has been of particular use for the functionalization of $N@C_{60}$ as, until recently, it was one of a few reactions that did not lead to a significant loss of the endohedral nitrogen during the reaction, see above. The first such reaction was performed in 2006 by attaching functional groups of varying size to the cage. EPR studies were then used to determine the change in zero-field splitting of the nitrogen atom, demonstrating that there is a trend of increased splitting with increasing size of ring bound to the surface of the fullerene. This is explained by the ability of the functional group to withdraw electron density from the fullerene and so disturb its symmetry [13].

1.1.2 Applications

Fullerenes have both a high electron affinity and a high electrical conductivity, making them extremely good electron acceptors for use in solar cells [16]. In addition to this, a number of functionalized fullerenes exhibit extremely fast photoinduced charge transfer, with a back action that takes place on time scales which are orders of magnitude longer [17]. This has allowed organic solar cells based on fullerenes to increase to over 10% power-conversion efficiency (PCE) in recent

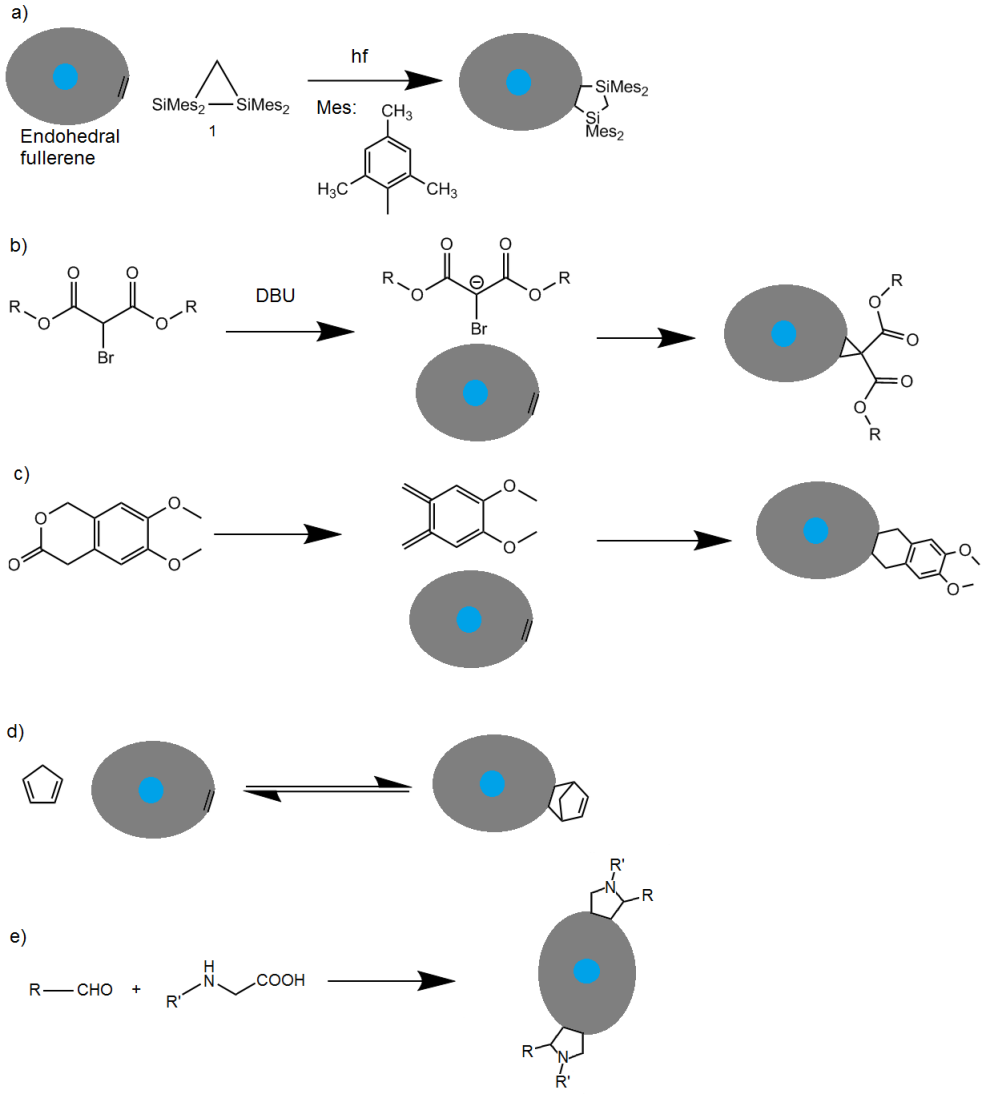

Figure 1: a) Photochemical reaction of an endohedral fullerene with a disilirane. The fullerene cage is simplified to show only the pertinent chemical bond for this reaction. b) The Bingel-Hirsch reaction between a generic reactant and an endohedral fullerene. Diels-Alder reaction with c) 6,7-dimethoxyisochroman-3-one and d) cyclopentadiene as the reactant. e) Prato reaction generalised for any reagent.

years [18]. However, this is still small compared to the 25% PCE observed in silicon solar cells. This difference in PCE is more than mitigated for large-scale applications as organic solar cells are cheaper, can be mass-processed and can be incorporated into flexible plastics for ease of use.

Fullerenes have also found a number of uses in the field of bio-medicine as both therapeutic and diagnostic tools. For therapeutic purposes the primary mechanism proposed for using fullerenes is in photodynamic therapy. This is where the molecule absorbs visible light to produce a long-lived triplet state, sensitising the production of the singlet oxygen radical to kill cells, for example cancerous cells [19]. However, this has not yet entered commercial viability due to the extensive nature of medical testing. Of more immediate application are endohedral fullerenes for use as MRI contrast agents. Paramagnetic gadolinium(III) complexes make good MRI contrast agents as the seven unpaired, isotropically distributed 4f electrons dramatically reduces the T_1 relaxation time for nearby water protons, leading to increased contrast in images [20]. This is advantageous over Gd-chelate complexes as there is a much lower risk of the toxic Gd atoms escaping the fullerenes and causing harm in the body. It is notable that, for any bio-medical application, it is necessary to find controllable methods of functionalizing fullerene molecules. The reasons for this are two-fold, first it is necessary to make these molecules water, and therefore blood, soluble. Secondly, it is necessary for this solubilisation to be controllable as only very well defined molecules can

be approved for medical trials.

Finally, the application most relevant to this thesis is the potential for fullerenes to be used in molecular electronics and quantum information. Simple examples of fullerenes being used in this field can be found in switchable molecular wires consisting of a porphyrin chain functionalized with fullerene molecules. When UV light is applied to the wire, electrons enter excited states on the fullerene, promoting a charge transfer from the porphyrin to the fullerene and leaving the porphryin chain able to conduct through the holes left in place of the electrons [21]. Fullerenes should also be ideal candidates for a quantum information architecture as individual atoms can remain in a superposition of states for long times and have the potential to be built into scalable systems. There are several endohedral fullerene molecules where the endohedral atom or cluster is spin active, with an electron and/or nuclear spin, which could be exploited for a number of technological applications, including quantum information [22]. It is also possible to functionalize fullerenes, through a variety of chemical techniques, such that they can be incorporated with other carbon nanomaterials. This has been demonstrated previously for carbon nanotubes [23], but this thesis extends the range of systems to graphene nanogaps [24], unlocking a greater range of possibilities for experimentation and technological advancement. However, in order to understand the results of these devices it is necessary to understand single electron transistors.

1.2 Single Molecule Electronics

Achieving single molecule electronics, where you are able to perform electrical measurements on individual molecules, is not trivial. However, several methods have demonstrated their ability to do so. These include the techniques of STM break junctions, mechanically controlled break junctions and electro-burned graphene nanoaps.

1.2.1 STM Break junctions

STM break junctions are prepared in a similar way as a conventional STM investigation of a surface, with an atomically sharp electrically conducting tip controlled with piezoelectric actuators above a surface decorated with the molecules of interest. These can either be adsorbed on the surface on in a solution on the surface. For measurements to be carried with molecules adsorbed on the surface, the tip is intentionally crashed into the surface, contacting several molecules, before being pulled away. As it is pulled away there will be the situation where only a single molecule attached to the tip, where it is closest to the surface, will be in electrical contact with both the tip and surface, allowing for electrical measurements to be carried out, see Figure 2 [25]. This allows rapid measurements to be made, allowing for large data sets for statistical studies of the electronic properties of molecules. However, there are some severe limitations on the practical application of STM break junctions due to the sheer size of the STM apparatus, preventing

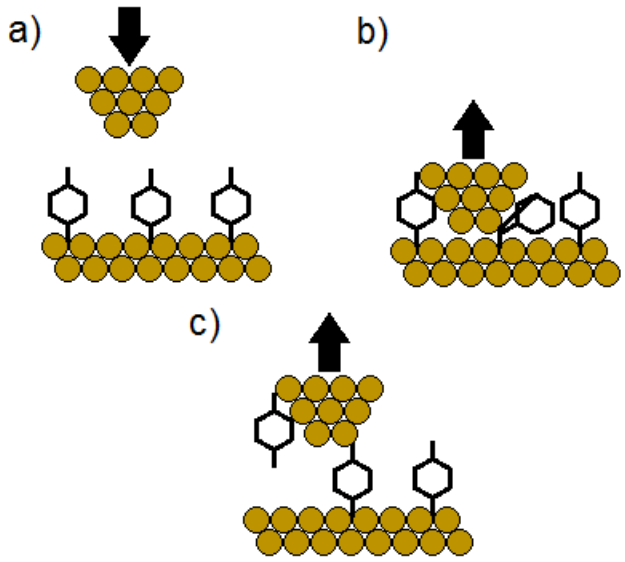

Figure 2: The formation of an STM break junction. a) The STM tip approaches a metallic surface decorated with molecules of interest before b) the tip crashes into the surface, contacting several molecules in the process. c) The tip is withdrawn until only one molecule is able to electrically contact both the STM tip and the surface.

the incorporation of molecules into commercial electronics. It is also not possible to electrostatically gate the molecule, making it impossible to probe the full range of its electrical properties.

1.2.2 Mechanically Controlled Break Junctions

Mechanically controlled break junctions (MCBJ) apply a mechanical force to produce electrodes with a controllable separation of the order of nanometers. In a typical MCBJ a notched metallic wire is fixed to a flexible substrate such that it is suspended over the substrate. A mechanical force is then applied to the flexible substrate using a three-point bending geometry, where the ends of the substrate

are fixed in place and a piezoelectric pushing rod bends the substrate. As the wire is attached to the substrate this acts to deform the wire. When sufficient force is applied the wire breaks at the notch, creating a nanometer scale gap in the wire, see Figure 3. By monitoring the tunnelling current and adjusting the displacement of the pushing rod it is possible to control the separation between the two newly formed electrodes [26].

Molecules can be introduced into the experiment by decorating the wire with them prior to the formation of the break junction. This leads to monolayer coverage of the two electrodes upon formation of a nanogap. Just as careful tuning of the gap size while monitoring the tunnelling current was able to lead to control over the properties of the nanogap, the same monitoring and control can be used in a system containing molecules to form and to identify a single molecule junction [27].

One of the advantages of MCBJs is that the electrodes are formed in-situ, creating exceptionally clean contacts, regardless of the methods used to fabricate the device. The gaps created are also extremely stable, and the ability to quickly control the junction allows for statistically meaningful data sets to be produced. However, MCBJs share many of the disadvantages of STM break junctions. Piezoelectric components are large, making the miniaturisation of this technology for practical applications impossible. It is also extremely difficult to incorporate a gating electrode into a MCBJ. Attempts have been made to incorporate a back-

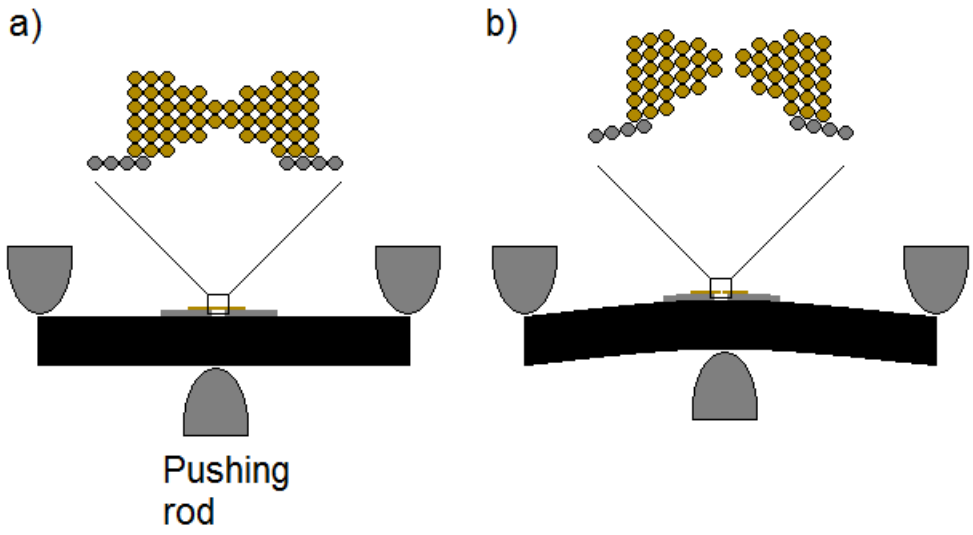

Figure 3: Formation of a MCBJ with a notched wire suspended on a flexible substrate with a) no applied force from the pushing rod and b) a force applied to the rod causing a small break junction to form.

gate into the substrate, which encounters problems due to a huge reduction in mechanical control over the properties of the break junction. These devices typically required additional techniques to be applied to create the break junctions due to the lack of mechanical control [28].

1.2.3 Electroburned graphene nanogaps

The method employed in this thesis to measure the electrical properties of functionalized fullerne molecules that I produced was Feed-back controlled electroburning[91]. This is able to reliably produce gaps between graphene electrodes of the order of nanometers. To create the graphene nano-gaps described here, single-layer graphene was deposited onto a silicon chip pre-patterned with Cr/Au electrodes.

This graphene was then patterned into a notched ribbon shape using electron-beam lithography and oxygen plasma etching, see Figure 4 a through d.

Once this notched ribbon of graphene contacted by metal electrodes has been achieved electroburning can be performed, which takes place on an automated probe station in ambient conditions. A voltage (V) is applied across the devices which is increased at a rate of 0.75 V/s, while recording the current (I) at a sampling rate of 200 ms. The feedback condition is a decrease in I within the past 150 mV. When this condition is met the voltage is rapidly decreased to zero at a rate of 225 V/s [91]. At the end of each feedback event, the resistance of the graphene ribbon is measured and the process is repeated until the resistance exceeds a set value. The results of this process are a large number of graphene ribbons with a small gap cut between them, initial experiments yielded 307 devices of which 94.8% displayed nanogaps with an estimated size between 0.5 and 2.5 nm [91]. The creation of a nanogap at the site of the graphene constriction can be understood by considering the current density through the device during the electroburning process. The site of the constriction will experience the greatest current density and therefore the greatest Joule heating, leading to thermally activated oxidation and ablation of the carbon atoms from the constriction [91]. Molecules can then be incorporated into the device by exploiting π-π stacking interactions with the graphene. If it is possible to functionalize the molecule of interest with two π-conjugated functional groups then it will be possible for those

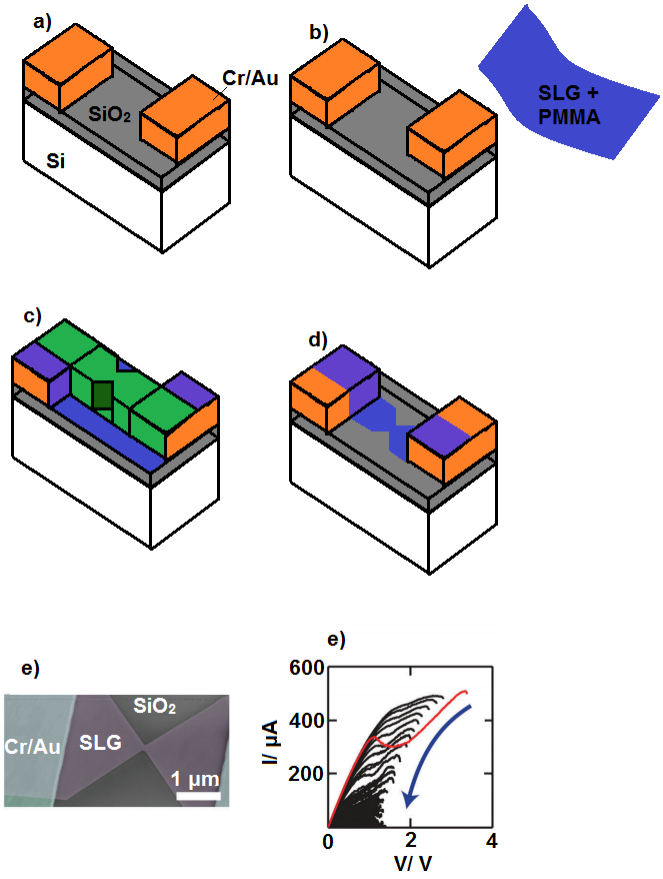

Figure 4: a)–d) Schematics for the process of device fabrication up to the electoburning stage. a) Cr/Au electrodes are deposited using standard lithographic techniques. b) SLG protected by PMMA is placed over the entire wafer which fabrication is occurring on. c) A notched ribbon of resist is created over the junction using electron-beam lithography. d) The PMMA and graphene that is not covered by resist is etched away leaving a notched ribbon of graphene and PMMA. e) SEM image of the junction, showing the graphene notched ribbon and Cr/Au electrodes. f) Current–voltage (I–V) traces recorded during the feedback-controlled electroburning process. The trace in red is the first voltage sweep, subsequent voltage sweeps show more ohmic behaviour with increasing resistance after each sweep.

groups to bind to the graphene electrodes either side of the gap.

The advantages of this technique over the previous methods of STM break junction and MCBJs is that it address the issues of size and gating. Because the gaps are created electrically, removing the requirement for bulky piezoelectric components, the device can be produced where its largest dimensions are of the order of micrometers, with 540 gaps produced on a 1cm by 1 cm Si/SiO_2 chip. The use of a Si/SiO_2 chip make the incorporation of a backgate comparatively simple allowing for a much greater range of electrical properties to be explored. However, the experimental requirements to measure such devices are significantly more complicated, requiring ultra-cold and UHV conditions to perform the sensitive measurements on molecular electronic states. It is also impossible to produce the volumes of measurements that can be attained in STM break junctions or MCBJs. While it is possible to produce hundreds of nanogaps on each chip it is not possible to measure all of these in the same experiment, necessitating long delays between measurements and making the collection of large datasets for statistical analysis impossible.

1.3 Single Electron Transistors

A single-electron transistor consists of a quantum dot (QD) between two electrodes, the source and drain, separated by tunnel barriers. In addition to these there is a third electrode, the gate, which is capacitively coupled to the QD.

Therefore, when a potential, V_g, is applied to the gate it changes the energy of electrons on the QD so that there can be a greater or smaller number of electrons on the dot. This gives rise to Coulomb blockade of the transistor, as a current can only flow when V_g increases such that an additional electron state is available on the QD. The distance between peaks is proportional to the addition energy, E_{add}, the energy difference between there being n and n+1 electrons on the QD, see Figure 5 a [29].

However, it is also possible to lift the Coulomb blockade by applying a bias between the source and drain electrodes, V_{SD}, which allows for tunnelling to occur through any electron state on the molecule present in this 'bias window' between the source and drain. This usually leads to a stability diagram being measured of conductance, or differential conductance, as a colour map while sweeping both V_g and V_{SD}, see Figure 5 b [29]. A quantum dot is the simplest system that can be imagined between the two tunnel barriers to form the single electron transistor. However, it is just as valid to imagine a single molecule connected to the electrodes by a chemical or physical interaction, allowing for the electronic states of individual molecules to be probed. In addition to finding the electron states of the molecule, such stability diagrams can also be sensitive to excited states of the molecule which enter the bias window, making this a powerful method for exploring the electronic structure of molecules [29]. Finally, being able to fill and empty individual electron states in a molecule has enormous potential in several

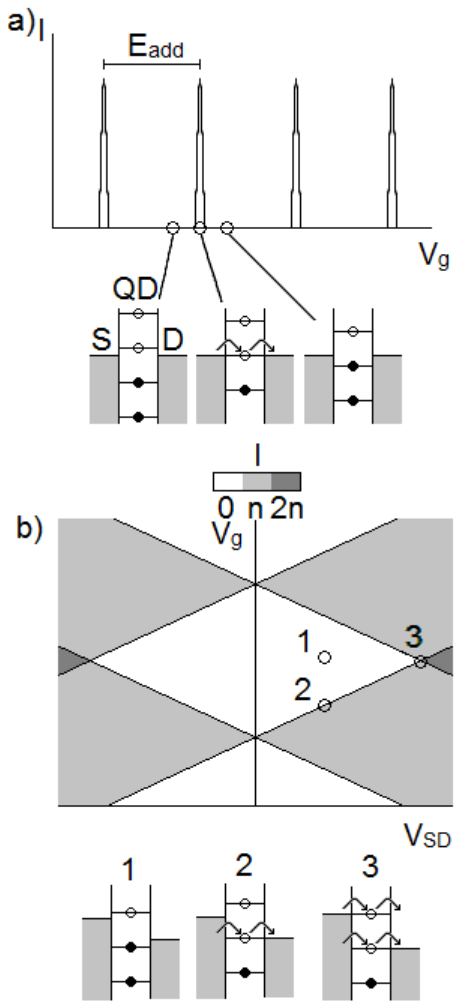

Figure 5: a) Current profile as V_g is varied for $V_{SD} = 0$. Current can only flow when an electron state on the quantum dot is exactly aligned with the Fermi level of the electrodes. b) Stability diagram for an idealised quantum dot where both V_g and V_{SD} are varied.

technological applications such as quantum information [30] and thermoelectrics.

1.4 The Thermoelectric Effect

The thermoelectric effect is most easily understood by looking at a system with a hot source and cold sink contacted by an n-type semi-conductor. Near to the hot

source carriers move quickly compared to the cold sink, this difference in carrier speed means that carriers build up at the cold sink, creating a potential difference between the contact near the hot source and the contact near the cold sink, leading to a current and so an electrical power due to the temperature difference, see Figure 6 a. The efficiency of a material to create a potential difference from a temperature difference is given by the Seebeck coefficient, $S = -\frac{\triangle V}{\triangle T}$. It is often valuable to consider the thermoelectric efficiency of a device, $z = \frac{S^2 G}{\kappa}$, where G is the electrical conductivity and κ is the thermal conductivity, which in thermoelectric materials is dominated by phonon conductivity. However, $G = ne\mu$, where n is the carrier concentration, e is the electronic charge and μ is the carrier mobility, allowing us to say that $z = (S^2 n)(\frac{\mu}{\kappa})e$. In conventional materials each bracket contains terms which are inversely proportional, for doped semiconductors the Pisarenko relation dictates that S and n are inversely proportional, while engineering defects in the crystal structure of the material to reduce κ also reduces μ [31]. However, by moving to low dimensionality materials it is possible to improve the situation dramatically. This is achieved by exploiting band-structure engineering of electrons and modified phonon dispersion relations to increase the thermopower by several orders of magnitude [32].

When moving to a molecular device it is again useful to consider the simplified model of a series of electron energy states contacted by a source and a drain which are now thermally broadened. This difference in thermal broadening leads to two

separate bias windows opening up. At high energies there are occupied energy states in the hot contact at the same energy as empty states in cold contact, allowing for transport, while the converse is true at low energies, see Figure 6 b. This gives rise to a variation of Seebeck coefficient with V_g as seen in Figure 6 c, which can be estimated from the current generated by the Landauer-Buettiker formalism,

$$I_{sd} = \frac{2e}{h} \int [f_H(E) - f_C(E)] T(E), dE \tag{1}$$

where $f_H(E)$ is the Fermi distribution in the hot contact, $f_C(E)$ is the Fermi distribution of the cold contact and $T(E)$ is the transmission probability through the junction [33].

1.5 Experimental Details

For the reaction carried out in this work C_{60} (99% purity), was purchased from the MER corporation, all other reagents were purchased from Sigma Aldrich and used as received. For a typical experiment pyrene-1-carboxaldehyde (30.3 mg, 132 mmol, 2 eq.), N-methylglycine (24.1 mg, 270 mmol, 4 eq.) and C_{60} (47.3 mg, 65.7 mmol, 1 eq.) were dissolved in toluene (90 ml). The reaction mixture was then extensively degassed with N_2, and heated to 110°C under a N_2 atmosphere for 30 hours. 0.5 ml aliquots were taken out of the reaction mixture at regular intervals,

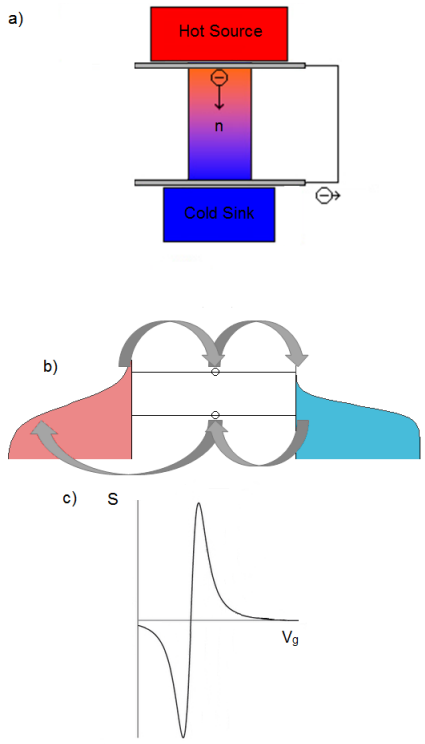

Figure 6: a) A hot source and cold sink contacted by an n-type semiconductor, this leads to a build up of charge and so a thermopower. b) How a thermopower is generated by a single molecule or quantum dot. c) The variation in the Seebeck coefficient for a quantum device as an energy level passes through the two bias windows created by the different thermal broadening experienced by each contact.

diluted with 1.5 ml of pure HPLC (High Performance Liquid Chromatography) grade toluene, and analysed by HPLC in order to record the progress of the reaction. Upon completion, the reaction mixture was dried under a reduced pressure and sonicated in methanol (200 ml). The resulting suspension was passed through a PTFE filter, and the precipitate was thoroughly washed with excess methanol (200 ml) to remove the majority of the unreacted pyrene-1-carboxaldehyde. The crude product was then dissolved in toluene again (100 ml) under sonication, concentrated to 20 ml, and separated by preparative HPLC [14].

The isolation of isomerically pure bisadducts is extremely difficult as the regioisomers have very similar physical properties [34]. The main technique used to isolate the regioisomers was HPLC, using a Japan Analytical JC-9103 recycling preparative HPLC and a COSMOSIL Buckyprep-M column, 20 X 250 mm, with toluene as the mobile phase at a flow rate of 16 ml/min, giving rise to the chromatogram in Figure 7 a. The products are eluted in order of polarity, with the more polar higher adducts (tris- and higher) eluted first (4-5.1 min), then the bis-adducts (5.1-7.8 min), monoadduct (7.8-9 min) and finally the least polar unreacted C_{60} (9-10 min). The bisadducts were then split into three fractions (F1, F2 and F3, Figure 7 a and 7 b). These were recycled to determine their isotopic purity, with those found to contain multiple isomers separated into isomerically pure fractions by a process of continuously recycling the peak and removing the tail (Figure 7 c and 7 d).

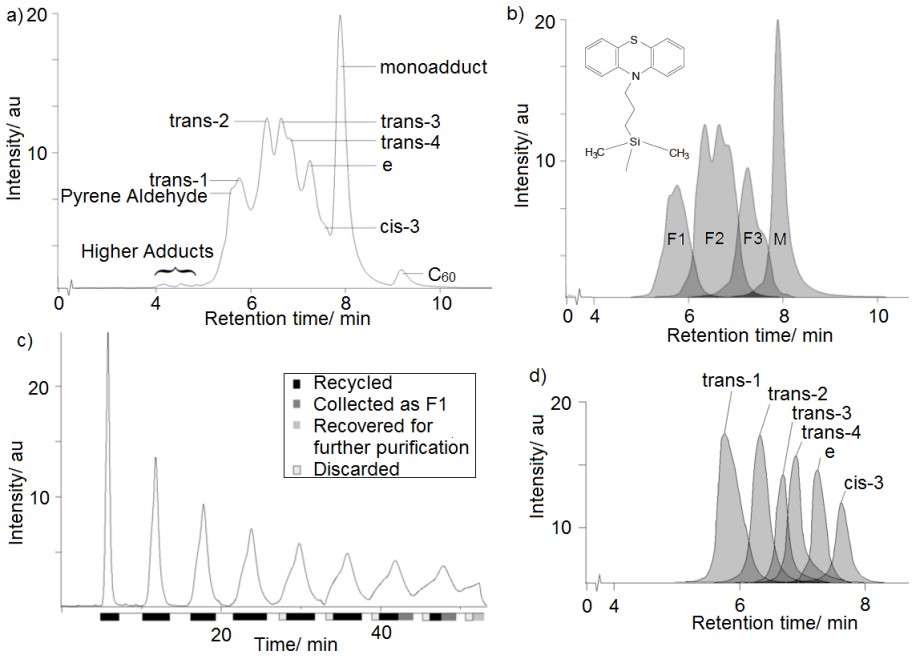

Figure 7: HPLC traces of a) a typical reaction mixture between C_{60}, pyrene-1-carboxaldehyde, and N-methylglycine after 30 hours; dashed lines indicate the first crude separation step of the bis-adduct; b) each of the crudely separated bis-adduct fractions F1, F2 and F3; inset, the chemical composition of the COMOSIL Buckyprep-M. c) Separation of the fraction F1 by recycling HPLC; and d) each of the six isolated regioisomers confirming the purity of each sample.

UV-Visible spectra were recorded in toluene solutions on a Jasco 570 spectrometer using quartz cuvettes. ^{1}H, ^{13}C and Heteronuclear Single Quantum Coherence (HSQC) Nuclear Magnetic Resonance (NMR) spectra were recorded in deuterated chloroform on a Bruker AVII 500 spectrometer with ^{13}C cryoprobe. Matrix-assisted laser-desorption ionisation time-of-flight mass spectra (MALDI-TOF MS) were obtained on a Bruker Ultraflex III MALDI-TOF spectrometer in negative ionisation mode using DCTB as a matrix. Excitation dependence photoluminescence maps and steady state spectra were recorded on a Jasco FP6200 and an ISA Fluoromax-2 Fluorimeter in both toluene and chloroform solutions.

The concentrations used for the Photoluminescent and ultraviolet–visible abosp-

tion measurements, which were used to estimate the quantum yield, are as follows. Pyrene: 10^{-6} g/ml in either toluene or ethanol, pristine C_{60}: $3x10^{-5}$ g/ml, pristine C_{70}: $0.67x10^{-5}$ g/ml, C_{60} monoadduct: $3x10^{-5}$ g/ml, C_{70} monoadduct: $3.16x10^{-5}$ g/ml and the quantum yield of C_{60} and its derivatives were recorded against pyrene. Based on the well-known pyrene quantum yield of 0.65 in ethanol it was possible to calculate the quantum yield in toluene to be 0.19 and then, based on this value, it was possible to estimate the quantum yields under 335 nm excitation as in [15]. For fullerenes the quantum yield value of $2.2x10^{-4}$ for C_{60} and $5.4x10^{-4}$ for C_{70} under 520 nm excitation were taken as references and a correction using the refractive index of ethanol and toluene was performed [15]. The following spectral ranges were used. pyrene in toluene: 325–346 nm, pyrene in ethanol: 325–346 nm, pristine C_{60}: 500–650 nm (exc. 520 nm), pristine C_{70}: 421–540 (exc. 520 nm), C_{60} monoadduct: 325–346 nm (exc. 335 nm), 500–650 (exc. 520 nm), C_{70} monoadduct: 325–346 nm (exc. 335 nm), 421–540 (exc. 520 nm).

2 Functionalization of Fullerenes

In order to apply fullerenes to the full range of applications discussed above it is necessary to chemically functionalize them so that they will bind to an electrode. The nature of this binding and the functionalization of the fullerene will influence the properties of the fullerene cage, allowing for some fine-tuning of those properties to optimise the fullerene for various applications. In this chapter I will present the reaction used to functionalize fullerenes with the pyrene group, which acts as an anchor to graphene electrodes through π-π stacking interactions. I also study the kinetics of the reaction, in order to optimise the production of bisadducts for incorporation into graphene nanogaps, and the regioisomerism of the products which is novel irrespective of the applications of these molecules.

2.1 Introduction

The addition of pyrene to fullerenes makes for extremely versatile molecules which display a variety of applications from the photosensitising of oxygen radicals, see Chapter 3 [14], to their incorporation into electronic devices, see Chapter 5 [24]. However, to best make use of these molecules and to extend the reaction to more exotic fullerenes it is necessary to fully understand the reaction, its products and its kinetics. The 1,3 dipolar cycloaddition reaction has been studied extensively with the fullerenes C_{60} and C_{70} previously [2]. However, the selective synthesis of particular bisadduct regioisomers, regioselectivity, is extremely difficult with

the few examples in the literature relying on tethered addition [35] while the best alternative is the isolation of bisadducts from a reaction mixture which requires laborious purification [14]. For this reason the synthesis, purification and characterisation of all of the isomeric products of a cyclco-addition reaction on C_{60} has only been reported with small, simple functional groups and in only a few cases. Previously, Hirsch et al [36] isolated and characterised seven different isomers of bis-(ethoxycarbonyl)methylene-C_{60} and Kordatos et al [34] made a similar study on the reaction between triethylene glycol mono methyl ether amino acid, paraformaldehyde and C_{60}, isolating and characterising eight bis isomers. In order to study the products of the reaction I decided to first try to understand the kinetics of the reaction.

2.2 Kinetics

To form a kinetic model of the reaction it was necessary for me to split the complete reaction into multiple coupled reactions, see Figure 8.

Here P stands for pyrene-1-carboxaldehyde, S for sarcosine, Y for the ylide intermediate, F for the pristine fullerene, M for the monoadduct, B for the bisadducts and $k_{1,2,3}$ are the rate constants of reaction 1, 2 or 3 respectively. These coupled reactions give rise to the equations (2) to (5) with the additional constraints displayed mathematically in equations (6) and (7).

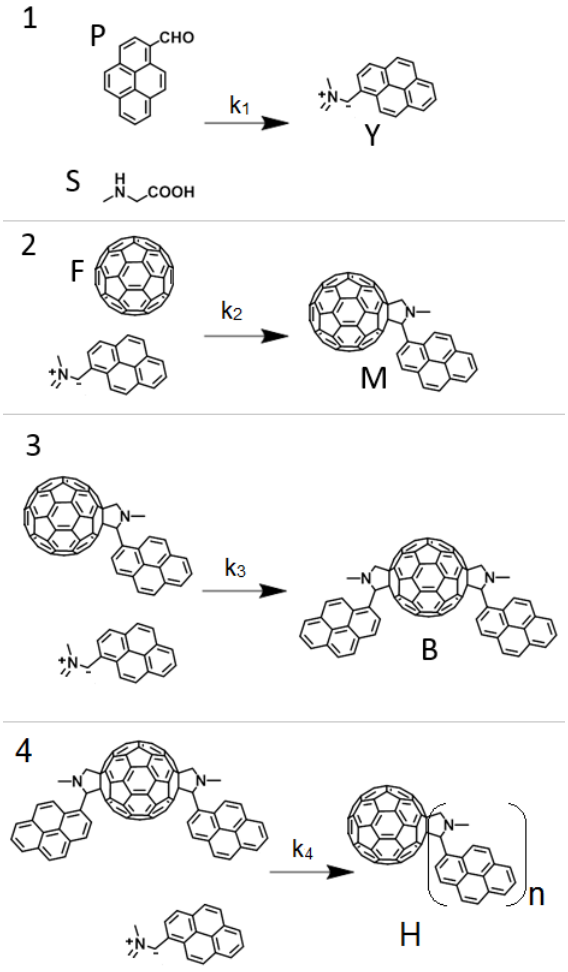

Figure 8: The Prato reaction broken down into four coupled reactions, the first to produce the reactive ylide species, in the second the ylide reactions with a pristine fullerne to form a monoadduct, in the third a ylide reacts with a monoadduct to form a bisadduct and in the fourth it reacts with a bisadduct to form a higher adduct.

$$[Y]' = -k_1[P][S] \tag{2}$$

$$[F]' = -k_2[F][Y] \tag{3}$$

$$[M]' = k_2[F][Y] - k_3[M][Y] \tag{4}$$

$$[B]' = k_3[M][Y] - k_4[B][Y] \tag{5}$$

$$[M]_0 = [B]_0 = 0 \tag{6}$$

$$[Y]' \approx 0,\ t > 0 \tag{7}$$

Here [X] is the concentration of X (where X = P, S, Y, F, M or B), $[X]_0$ is the initial concentration of X and $[X]'$ is the first derivative of the concentration of X with respect to time. Equation (6) is a statement that when the reaction first starts there will be no products in the reaction mixture, so the initial concentration of ylide, monoadduct and bisadduct are defined as zero. Equation (7) is a statement of the steady state approximation [37], where it is assumed that the ylide being produced will almost immediately go on to react with the pristine fullerene or the monoadduct. The ylide will therefore be generated and depleted at the same rate and so the concentration of this reactive intermediate will be approximately constant throughout the reaction. This is not strictly true as the ylide will have a bi-exponential profile, similar to the monoadduct. It will reach an appreciable concentration early in the course of the reaction before the concentration slowly decays as [P] and [S] decrease. However, this approximation is good for the case that $k_1[P][S] \ll k_2[F] + k_3[M]$, which is true for this reaction at all but the earliest reaction times.

The steady state approximation allows me to treat [Y] as a constant, allowing me to find solutions for the equations 3, 4 and 5 in turn, substituting the solution of the previous equation for the variable which is not the subject of the differential equation. These yield the solutions:

$$[F](t) = [F]_0 e^{-k_2[Y]t} \tag{8}$$

$$[M](t) = [Y]^2 k_2 [F]_0 (k_3 - k_2)(e^{-k_2[Y]t} - e^{-k_3[Y]t}) \tag{9}$$

$$[B](t) = [Y]^3 k_3 k_2 [F]_0 (k_3 - k_2)((k_4 - k_2)[Y] e^{-k_2[Y]t}$$

$$-(k_3 - k_2)[Y]e^{-k_3[Y]t} - ((k_4 - k_2) - (k_3 - k_2))[Y]e^{-k_4[Y]t}) \tag{10}$$

By fitting these equations to experimental data, as in Figure 9 a, I was able to determine values for [Y]k_2, [Y]k_3 and $\frac{k_2}{k_3}$, which are summarised in Table 2 for the reactions with C_{60} and C_{70}. In both cases the reaction stoichiometry and concentration was identical with the reagents mixed in a ratio of 4:2:1 of sarcosine,

	$[Y]k_2/mol^{-1}\ dm^3\ min^{-1}$	$[Y]k_3/mol^{-1}\ dm^3\ min^{-1}$	$\frac{k_2}{k_3}$
C_{60}	$3.506 \pm 0.127 \times 10^{-3}$	$8.2 \pm 2.5 \times 10^{-4}$	4.14 ± 1.41
C_{70}	$1.658 \pm 0.493 \times 10^{-3}$	$4.735 \pm 1.56 \times 10^{-4}$	3.49 ± 2.19
$\frac{C_{60}}{C_{70}}$	2.115 ± 0.705	1.732 ± 1.099	n/a

Table 2: Rate constants as derived from reaction data. Both reactions proceed approximately twice as fast with C_{60} compared to C_{70} and in both cases the reaction to produce the monoadduct is approximately four times as fast as the reaction to produce the bisadduct.

pyrene-1-carboxaldehyde and fullerene under the conditions described in Chapter 1 for a total of 24 hours.

I then further investigated the effect of stoichiometry on the reaction with C_{60} by performing a series of reactions. This was done with the aim of finding the rate determining step for this reaction and so to inform future reaction stoichiometries, optimising the production of mono or bisadducts. These reactions were carried out according to the conditions described in Chapter 1 for 10 hours to yield the results shown in Figure 9. This data shows that the reaction is zero-order with respect to the concentration of amino acid, while it is first order with respect to the concentration of aldehyde. This implies that the rate determining state involves only the aldehyde and so it is this reagent which should be varied to control the rate of the reaction. These kinetic studies provide information about the rate of formation of the bisadducts in general. The intended application of these materials requires the bisadduct of the reaction, so it is necessary to optimise the reaction for their formation. However, there are many possible isomers of the bisadducts which must be investigated in greater detail if they are to be understood.

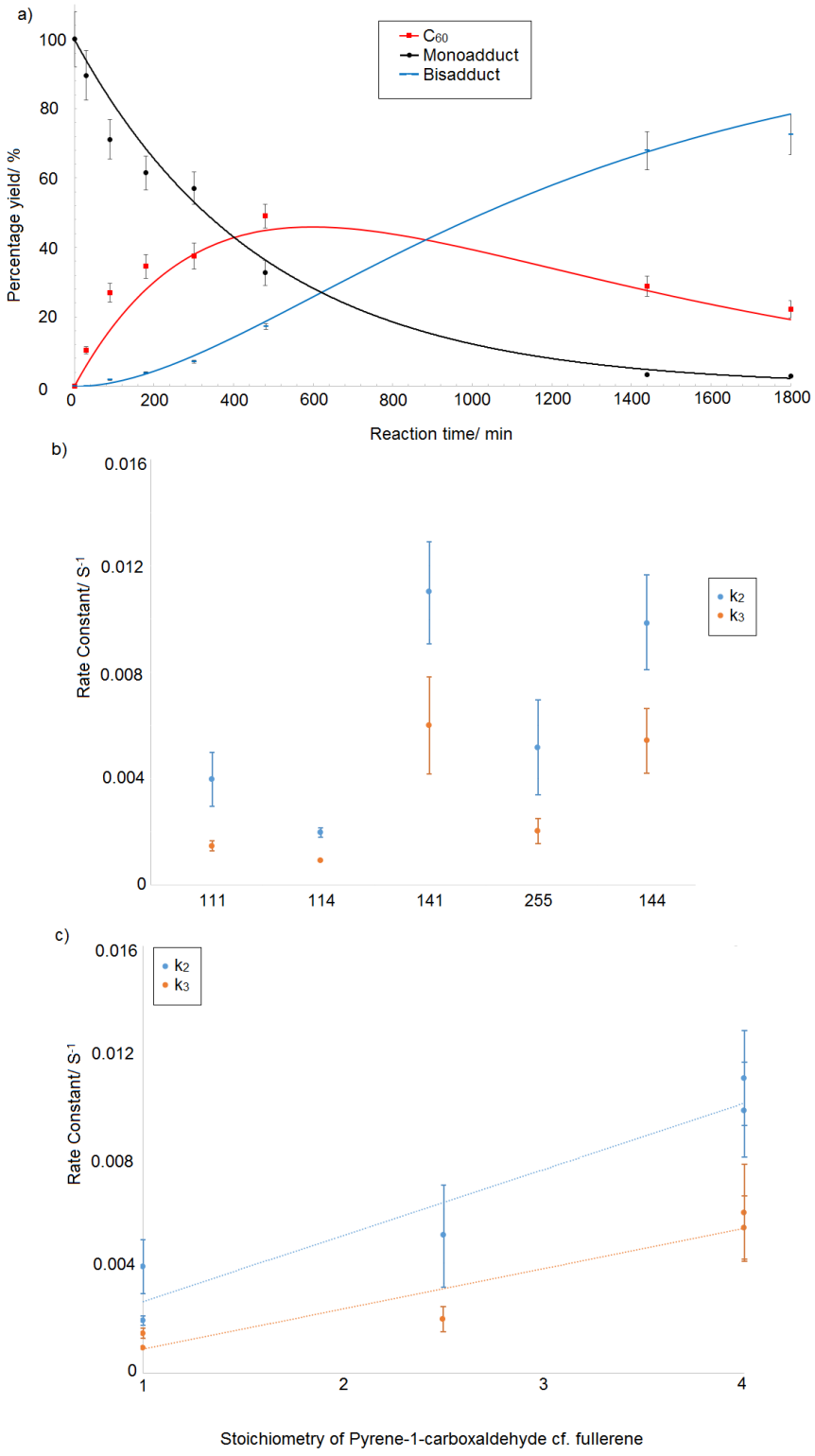

Figure 9: a) An example of a reaction which was performed where the quantity of C_{60}, mono and bisadduct are plotted as a function of reaction time and fitted to the integrated rate equations (11), (12) and (13) to find the values of k_2 and k_3. b) The values of the rate constants k_2 and k_3 as determined experimentally for different stiochiometies of fullerene: pyrene-1-carboxaldehyde: sarcosine. c) The relationship between the rate constants k_2 and k_3 compared to the stoichiometry of pyrene-1-carboxaldehyde.

2.3 Optimisation

In order to produce a large quantity of each regioisomer, which will be discussed shortly, it was necessary to optimise the reaction for the production of the bisadduct. There are several reaction conditions which can be changed to maximise the yield of the bisadduct, including temperature, reaction duration and reaction stoichiometry. In addition to optimising the yield of the bisadduct it would also be advantageous to optimise the duration of the reaction to increase the quantity of material that can be produced in total.

I found that the temperature had no effect on the yield of the bisadduct over the course of the reaction. However, cooling the temperature from 110°C slowed the rate of reaction, while increasing the temperature above 110°C had very little effect on the reaction at all. Therefore, I decided to keep the reaction temperature at 110°C.

The reaction stoichiometry and reaction duration are closely linked as, for a higher ratio of aldehyde and amino acid, there will be a large quantity of bisadduct produced in a short space of time, while for a lower ratio of aldehyde and amino acid the reaction will have to proceed to completion in order to achieve a high yield of the bisadduct. This trend can be seen in Table 3, where a reaction with a 1:4:8 ratio produces greater quantities of the bisadduct at earlier reaction times. However, as the reaction proceeds the greatest observed yield is significantly lower. This is because at later reaction times the bisadduct is converted into

Reaction Time/ min	60	120	180	300	480	1320
Reaction Stoichiometry						
1:2:2	2.45	5.12	6.21	8.54	13.2	42.1
1:2:4	2.58	5.36	6.57	9.09	14.8	50.9
1:4:8	4.51	9.23	11.84	16.54	22.54	31.42

Table 3: The percentage yield of the pyrene containing bisadduct at different reaction times and for different reaction stoichiometries of fullerene: pyrene-1-carboxaldehyde: sarcosine.

tris- and higher adducts for this reaction, while reactions with a reduced quantity of aldehyde and amino acid, even when run to completion, only exhibit a small quantity of higher adducts. When looking at the reaction with a 1:2:2 ratio, there are lower observed yields at all reaction times compared to the 1:2:4 reaction. This is because the aldehyde used, sarcosine, is fairly insoluable in toluene, and so a slight excess needs to be used in order to achieve the optimum stoichiometry, meaning that even when then 1:2:2 reaction is run to completion there is still a significant quantity of unreacted monoadduct remaining in the reaction mixture. Having produced a large quantity of the bisadduct, with more than 500mg produced in a typical reaction, it is then possible to further isolate the different regioisomers to study them in greater detail.

2.4 Regioisomerism

The C_{60} cage is very symmetrical, displaying I_h symmetry, and so all of the [6,6] bonds are chemically equivalent and they can all be attacked by the reactive ylide group during cyclo-addition. This equivalence of the chemical bonds means that

it is only possible to generate a single regioisomer of the monoadduct. However, once the first reaction has occurred the I_h symmetry of C_{60} is reduced to C_{2v} and the remaining [6,6] bonds are split into 8 sets which are no longer equivalent. Therefore, 8 possible regioisomeric bisadducts can be observed [38]. The positions of the two joining groups relative to each other allows the regioisomers to be classified, see Figure 10 a [36]. To date, it has only been possible to observe all 8 of these regioisomers for a C_{60}-pyrrolodine derivative that has unfunctionalized CH_2 groups creating the pyrrolidine ring [34].

The C_{70} cage has D_{5h} symmetry, which is much lower, and leads to the existence of 4 sets of non-equivalent reactive [6,6] bonds in the pristine fullerene and so the monoadduct has 4 different regioisomers, see Figure 10 b [44]. To further complicate matters, the 4 bonds display a markedly different reactivity, with the equatorial bonds, where the curvature is the lowest, (bonds 1 and 2 on Figure 10 b) displaying lower reactivity than the polar bonds (3 and 4, Figure 10 b), which are considerably more reactive. Each of the 4 non-equivalent monoadducts will then go on to create their own distinct family of bisadducts, leading to a grand total of 38 possible regioisomers of the bisadduct. The yield of each of these will be determined by a complex interaction of the sterics of each relative orientation of the functional group as well as the individual reactivity of each chemical bond [44]. For these reasons it was not possible to accurately isolate or characterise the regioisomers of the C_{70} reaction. For an example of the additional complexity in

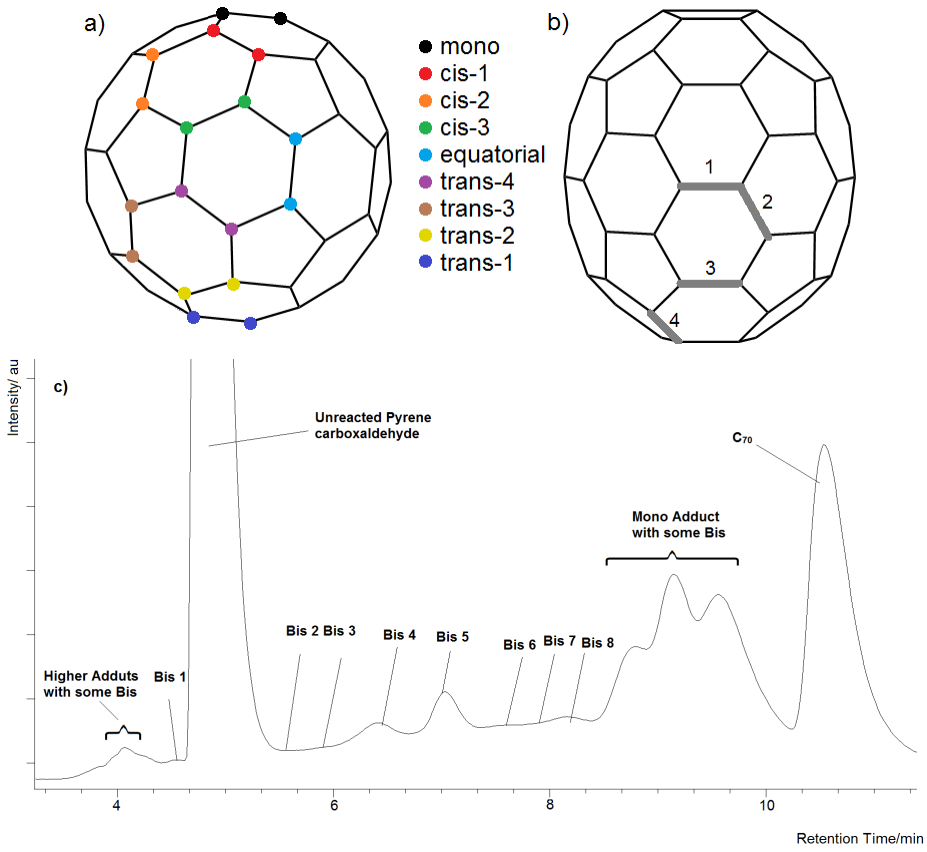

Figure 10: Schematic representation of a) the C_{60} fullerene cage showing the relative positions of the reactive [6,6] double bonds which can participate in the Prato cycloaddition reaction, and the nomenclature of the corresponding C_{60}-Prato bisadducts. b) The C_{70} fullerene cage showing the position of the 4 non-equivalent reactive [6,6] double bonds which can participate in the Prato reaction, yielding 4 regioisomeric monoadducts. c) The HPLC of a completed C_{70} reaction, showing at least 8 bisadduct peaks and 3 distinct monoadduct peaks.

the C_{70} reaction the HPLC trace of a completed, unfiltered, reaction can be seen in Figure 10 c, showing at least 8 bisadducts. Further analysis of the spectrum reveals additional bisadducts in the higher adduct and monoadduct portions of the spectrum as well as finding additional shoulders within the bisadduct peaks, giving rise to at least 15 regioisomers which are observable in this reaction.

2.4.1 Characterisation

The first information I used to identify the different bisadducts was their elution order during HPLC. This is because compounds elute from the Buckyprep-M column in reverse polarity order, which implies the order trans-1, trans-2, trans-3, trans-4, equatorial, cis-4, cis-3, cis-2, cis-1. This order has been observed for the products of similar reactions with smaller, less bulky functional groups [34, 38, 39]. In contrast to reactions with less sterically demanding functional groups, it was only possible to isolate 6 different regioisomers of the 8 which are known to be possible from symmetry considerations [34]. This indicates that the bulky and aromatic pyrene groups interfere with the reaction to form particular regioisomers, most likely those where the pyrene groups would be least spatially separated on the cage, the cis-1 and cis-2 isomers, preventing the formation of appreciable quantities of these isomers. However, the elution order is insufficient to determine the identity of each fraction, further information is needed which is summarised in Table 4.

UV-Vis spectroscopy was the principal method that I used to identify the different regioisomers, all of these absorption spectra were recorded in toluene solutions. Below 400 nm the spectra primarily shows the absorption of the two pyrene units, with maxima at 396 nm, 375 nm and 365 nm [14]. The visible region of the spectra displays features from the fullerene cage, which are of a much lower intensity than the highly photo-active pyrene unit. However, it is

Molecule	HPLC fraction	t_R, min*	UV-Vis features/ nm	1H NMR /ppm			Molecular Weight/ amu
				CH_3	CH_2	CH	
Mono	mono	8.00	433	2.78	4.21-4.47	5.08-5.11	977.12
Trans-1	1	5.75	480, 540, 577, 624, 657	2.34-2.70	3.61-4.99	5.47-5.84	1232.22
Trans-2	2.1	6.34	460, 495, 650-720	2.46-2.92	4.11-5.37	5.42-5.70	1232.23
Trans-3	2.2	6.64	420, 460, 491	2.40-2.91	3.87-5.26	5.72-6.10	1232.22
Trans-4	2.3	6.84	457, 490, 648, 705	2.26-2.88	3.81-5.20	5.43-6.00	1232.22
Equatorial (e)	3.1	7.26	422, 449	2.10-2.90	3.65-4.89	5.31-5.90	1232.23
Cis-3	3.2	7.55	415, 433, 447, 464, 642, 715	2.57-3.07	4.21-4.57	5.12-5.38	1232.22

Table 4: Structural characterisation data for each of the regioisomeric C_{60}-pyrene bisadducts isolated by recycling HPLC.
*Retention times on the Buckprep-M column eluted in toluene at a flow rate of 16 ml/min.

possible to detect a weak fullerene transitions in the range 400-750 nm, which can be used to characterise each regioisomer. It is worth noting that fullerene features closest to the pyrene signal, in the region 400-450 nm, appear as shoulders of the significantly more intense pyrene absorption as opposed to well isolated peaks. Previous work has observed the maximum absorption features for each regioisomer and, by comparision to these measurements, important information was gained as to the identity of each fraction.

It was thus possible for fractions 3.1 and 3.2 to be unambiguously identified as the equatorial (e-) and cis-3 isomers respectively. The strong absorption bands at 422 and 449 nm displayed by fraction 3.1 are characteristic of the equatorial isomer (See Figure 11 e and Table 4) [38, 34, 45]. In a similar way it was possible

to identify fraction 3.2, which is unique in exhibiting two sharp absorption peaks at 642 and 712 nm, which are characteristic of the cis-3 isomer. Additionally, a set of weak transitions were observed at 415, 433, 447 and 464 nm (See Figure 11 f) [45].

Fractions 1, 2.1, 2.2 and 2.3 all display absorption spectra with similar shape. However, subtle variations in the position of peaks makes it possible for them to be identified as the regioisomers trans-1, trans-2, trans-3 and trans-4 respectively. Fraction 2.3 displays two strong absorption features at 457 and 490 nm, as well as two broad, weak transitions at 648 and 705 nm, all of which are typical for the trans-4 isomer (See Figure 11 d) [39, 45]. Likewise, fraction 2.1 displays two broader peaks at 460 and 495 nm, as well as a series of weak, ill-defined absorptions in the range 650-720 nm, which are all typical for the trans-2 isomer (See Figure 11 c) [38, 34, 45]. Fraction 2.2 displays a transition at 420 nm and two broad, overlapping transitions at 460 and 491 nm, similar to fraction 2.1 but lower in intensity and much broader, which is typical for the trans-3 isomer (See Figure 11 b) [38, 34, 45].

Finally, I identify fraction 1 as the trans-1 isomer (See Figure 11 a). This assignment based on the UV-Vis spectra is in good agreement with my initial estimation of the content of each fraction as determined from their elution order in HPLC, allowing me to be confident in the assignments that I have made. Both the isomers cis-1 and cis-2, which have particularly characteristic absorption

signatures, making their misidentification unlikely [45], are not observed. This implies that my initial thoughts regarding these sterically crowded structures and their favourability is likely to be correct and I conclude that these products are formed in insufficient quantities to isolate or identify them from the mixture. Fluorescence measurements under two different excitations, λ_{exc}=330; 480 nm, indicated minor differences in the light emitting properties of the bisadducts (See Figures A1 and A2).

I then studied each isomer further using ^{1}H and ^{13}C NMR spectroscopies, as well as HSQC 2D NMR spectroscopy. It has been shown that there is a consistent change of the chemical shift of N-methyl and methylylidene group ^{1}H NMR resonances in fullerene pyrrolidines [36, 38]. Additionally, the relative position of each functional group around the fullerene cage changes the symmetry group of the molecule, giving rise to different numbers and multiplicities of signals in both ^{1}H and ^{13}C NMR. However, the interpretation of the resultant NMR spectra from C_{60}-pyrene bisadducts is significantly more complicated than those reported previously. This is due to the position of the pyrene group attached to the methylylidene carbon of the pyrrolidine ring, it both lowers the symmetry of the molecule and makes it possible for further stereoisomerism to present itself. Case in point, the most symmetric of the regioisomers, trans-1, is present as two disastereomers as there are two possible relative orientations of the pyrene groups (Figure 12 a). By a similar mechanism, the less symmetric trans-2, trans-3, trans-4, e-,

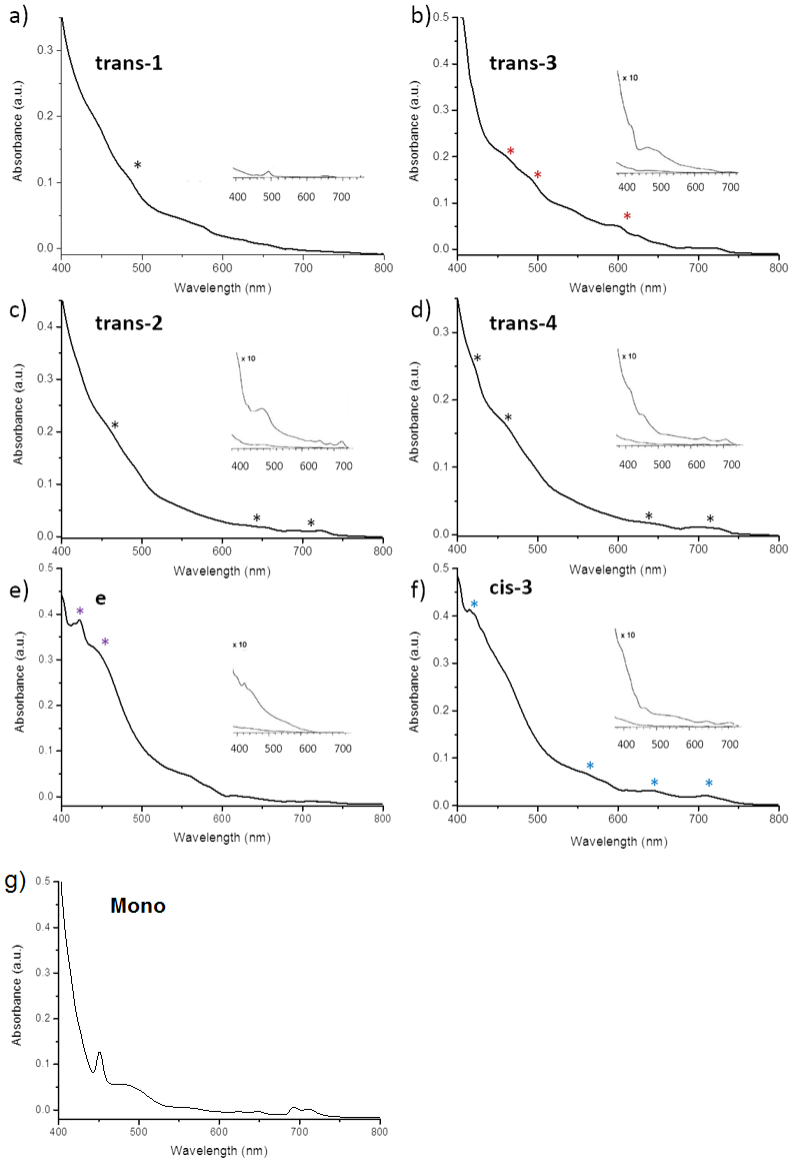

Figure 11: UV/vis absorption spectra of the isolated regioisomeric C_{60}-pyrene bis-adducts recorded in toluene solutions. The insets show absorption spectra of the corresponding cage isomers of bis-N-m-TEG fulleropyrrolidines reported previously. The asterisks mark the characteristic absorption bands of each isomer observed in both this work and previous reports which were used to characterise my samples.

and cis-3 isomers display several diastereomers (Figure 12 b). To further complicate matters, the pyrrolidine ring is non-planar. Therefore, the pyrene group and hydrogen atom can be in either the axial (a-) or equatorial (e-) positions on the pyrrolidine ring, giving rise to a second form of stereoisomerism. By once more looking at the isomer trans-1.1, it is possible to create three stereoisomers in which the pyrene groups are in the configuration where both are equatorial to the pyrrolidine ring (e,e-trans-1.1), both axial (a,a-trans-1.1), or there is one in each orientation (a,e-trans-1.1) (Figure 12 c). Similarly, each of the other isomers display this stereoisomerism. The ^{1}H NMR spectra of each of these many different stereoisomers marginally differ, giving rise to an extremely complicated ^{1}H NMR spectrum for each of the regioisomeric bisadducts, seen as a number of closely overlapping peaks in each case, an example of which can be seen in Figure 13. ^{1}H NMR spectra for each regioisomer can be seen in Figures A3 - 8.

Therefore, it is only possible to glean a small amount of structural information from the ^{1}H NMR spectra of these molecules. However, this led to a huge amount of time and effort being invested in producing large quantities of ultra-pure regioisomers from HPLC to try to improve the quality of the NMR spectra which were produced. This included a comprehensive study of the effect of solvents on the NMR data. For samples of more than 2 mg of fullerene solvated in 0.7 ml of a chosen deuterated solvent I always observed sedimentation of the sample when left undisturbed for any length of time. I thought that precipitation may be af-

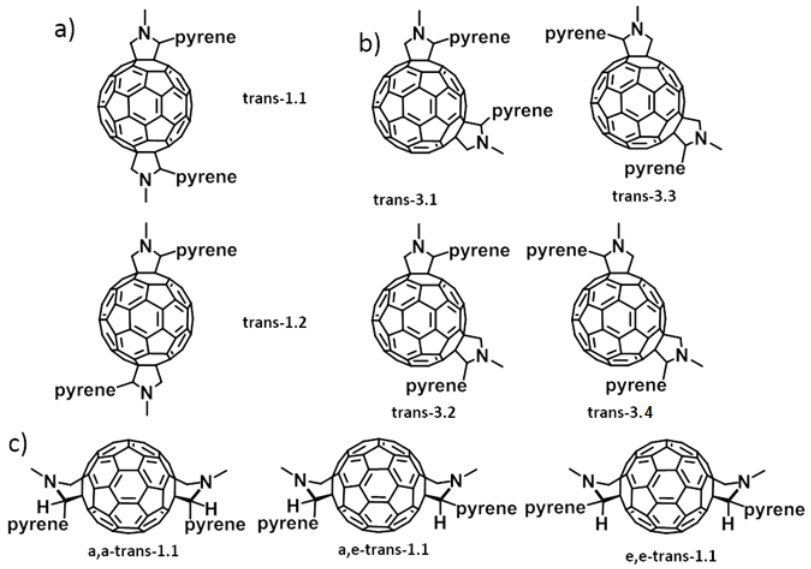

Figure 12: Possible diastereomers of a) trans-1 and b) trans-3 C_{60}-pyrene bisadducts, and c) pyrrolidine ring stereoisomers in a trans-1.1 adduct.

fecting my NMR specra, as this would broaden signals and thus reduce the signal to noise. I tried a mixture of CS_2 for high solubility with deuterated chloroform, deuterated toluene or deuterated benzene to create a lock signal. Additionally, I tried using pure deuterated toluene and benzene. Unsurprisingly, as isomerism was the responsible for the poor results, none of these dramatically improved the NMR spectra, deuterated toluene was significantly worse than either of the other solvents and deuterated benzene left solvent signals in the middle of my region of interest, making it unsuitable for studying these particular molecules.

As with the ^{1}H NMR spectra, the number of stereoisomers in each structure gives rise to a much greater number of peaks in ^{13}C NMR than is to be expected from the symmetry group of the regioisomer. Each ^{13}C NMR spectra displays a veritable forest of over 100 peaks in the range 120 to 160 ppm corresponding to the

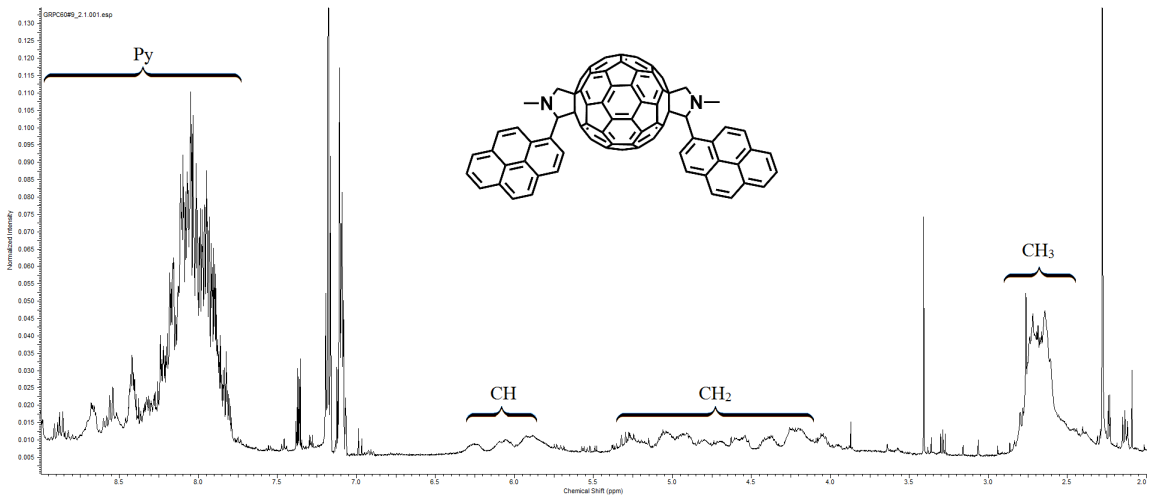

Figure 13: ^{1}H NMR Spectra of the trans-1 isomer. As can be seen there are far more peaks than would be expected without additional isomerism in the molecule. This is the regioisomer which created the simplest NMR spectra. However, it was still not possible to assign individual peaks to protons in the sample.

sp^2 carbons of the fullerene cage as well as the sp^2 carbons of the pyrene group. There are also a large number of closely overlapping signals in 60-80 ppm region, corresponding to the sp^3 carbons on the fullerene cage and pyrrolidine ring (Figure A9). As with the ^{1}H spectra, the wide variety of stereoisomers makes it unfeasible for me to draw structural conclusions based on the ^{13}C NMR spectroscopy.

2.4.2 Regioisomer yield

Having identified each of the regioisomers it was possible for me to investigate the rates of formation of each of the regioisomers over the course of the reaction as well as the ultimate yield for each regioisomer. In order to achieve this, aliquots of the reaction mixture were taken at regular time intervals and the content was evaluated by HPLC. In each case the HPLC trace was approximated to a sum of Gaussian peaks, to prevent inaccuracies due to overlapping peaks, in order

to determine the peak area of each component. It should be noted that the extinction coefficient is assumed to be constant between the regioisomers for the detector wavelength of 312 nm and so the area of HPLC peaks is assumed to be representative of the molar yield. Figure 14 displays the yield of each regioisomer from the start of the reaction up to a time of 30 hours. The traces in 14 a are used to calculate the data used in Figures 14 b and c, the latter of which shows the evolution of each of the regioisomers over the course of the reaction. From this I determine that the relative yield of the trans-2 and trans-3 regioisomers are largely unchanged over the duration of the reaction, whereas the regioisomers trans-1 and cis-3 increase over the course of the reaction. For the cis-3 isomer this is explained by the difficulty in isolating this minor product in the very low quantities present at early reaction times. However, this is not sufficient to explain the increasing yield of the trans-1 isomer. Where this is the isomer with the greatest separation between bulky pyrene groups, it is thought that this increased concentration is due to the less favourable regioisomers being broken down to form the trans-1 isomer over long reaction times. Conversely, the trans-4 and equatorial isomers are seen decreasing in abundance over the course of the reaction. Part of this decrease will be due to the misidentification of the cis-3 isomer at early reaction times. The remaining reduction is thought to be these less favourable regioisomers breaking down to form the more favourable trans-1 isomer over long reaction times.

By examining the yields of each regioisomer (Table 5), it can be seen that

the isomers produced in the greatest quantities are the trans-1 (18.8 ± 2.2 %) and trans-2 (18.9 ± 2.2 %) isomers, closely followed by trans-4 (16.7 ± 2.1 %). Curiously, the trans-3 isomer shows a yield of just 8.2 ± 1.8 %. The yield increases slightly when moving to the e- isomer to 10.8 ± 1.6 % and finally the cis-3 isomer displays the lowest yield of 3.5 ± 1.4 %. As mentioned previously, neither the cis-2 or cis-1 isomers are detected in this reaction. When I carried out the reaction at different temperatures there was little deviation from these yields over the course of the reaction, confirming that the variation in yield observed is thermodynamic rather than kinetic in origin (see Figures A10 and 11). For later comparisons to be made on the reactivity of formation for each isomer, it was necessary for me to normalise the yield to take account of the number of possible reaction sites which can lead to the formation of each isomer. For isomers trans-2, 3, 4, equatorial and cis-2 there are 4 equivalent [6,6] reactive sites which contrasts with the trans-1 isomer, where there is only 1 possible reaction site. This means that to normalise the yield of the isomer trans-1 it is necessary to multiply the observed yield four-fold compared to the other isomers, which have identical normalised and observed yields, see Table 5.

2.4.3 Discussion

By considering the information presented in Figure 15 and Table 5 it can be seen that for the bulky and planar aromatic pyrene, the formation of the trans- isomers

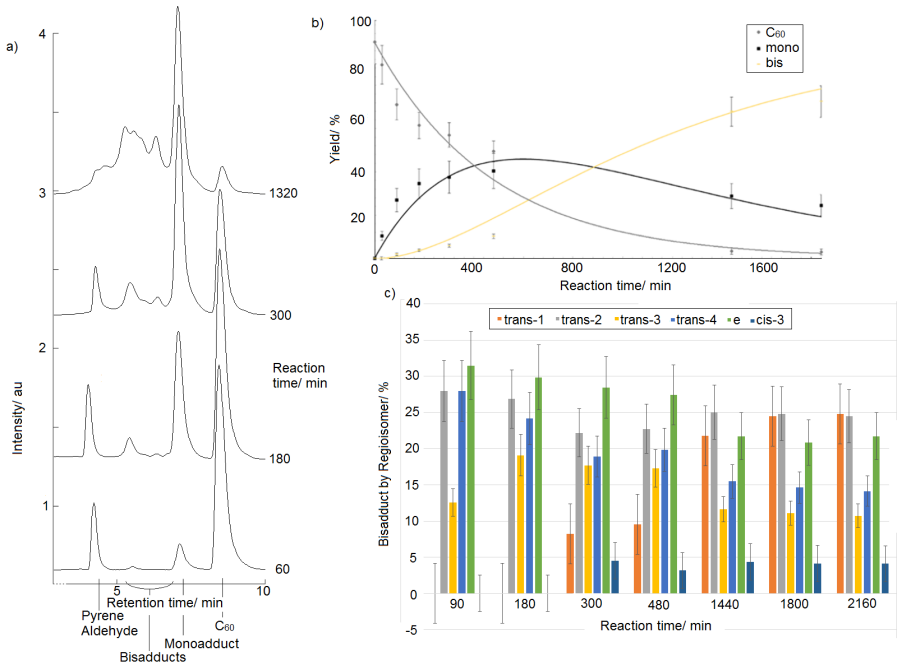

Figure 14: a) The chromatographic profile of the reaction between C_{60}, 1-pyrene carboxaldehyde and N-methylglycine at regular time intervals. b) The corresponding kinetic curves for the C_{60}, mono- and bisadducts. c) The percentage of the total bisadduct signal comprised of each of the regioisomers trans-1, trans-2, trans-3, tarns-4, e and cis-3.

Isomer	Distance /no. of bonds	Yield[1] at 30hrs/%
Trans-1	9	18.8 ± 2.2[2]
Trans-2	8	18.9 ± 2.2
Trans-3	6	8.2 ± 1.8
Trans-4	6	16.7 ± 2.1
e	5	10.8 ± 21.6
Cis-3	4	3.5 ± 1.4

Table 5: The observed and normalised yield of each isomer after the reaction has proceeded for 30 hours. Also displayed are the number of carbon-carbon bonds between the site where the first and second functional groups are attached.
[1]Determined by HPLC peak area ratios approximating each HPLC trace to be a sum of Gaussian peaks and assuming the extinction coefficient at the detector wavelength (312 nm) is the same for each of the isomers. Each entry is an average of 3 runs.
[2]Corresponding to a normalised yield of 75.2 $\pm$ 8.8% for 4 equivalent reactive carbon-carbon bonds.

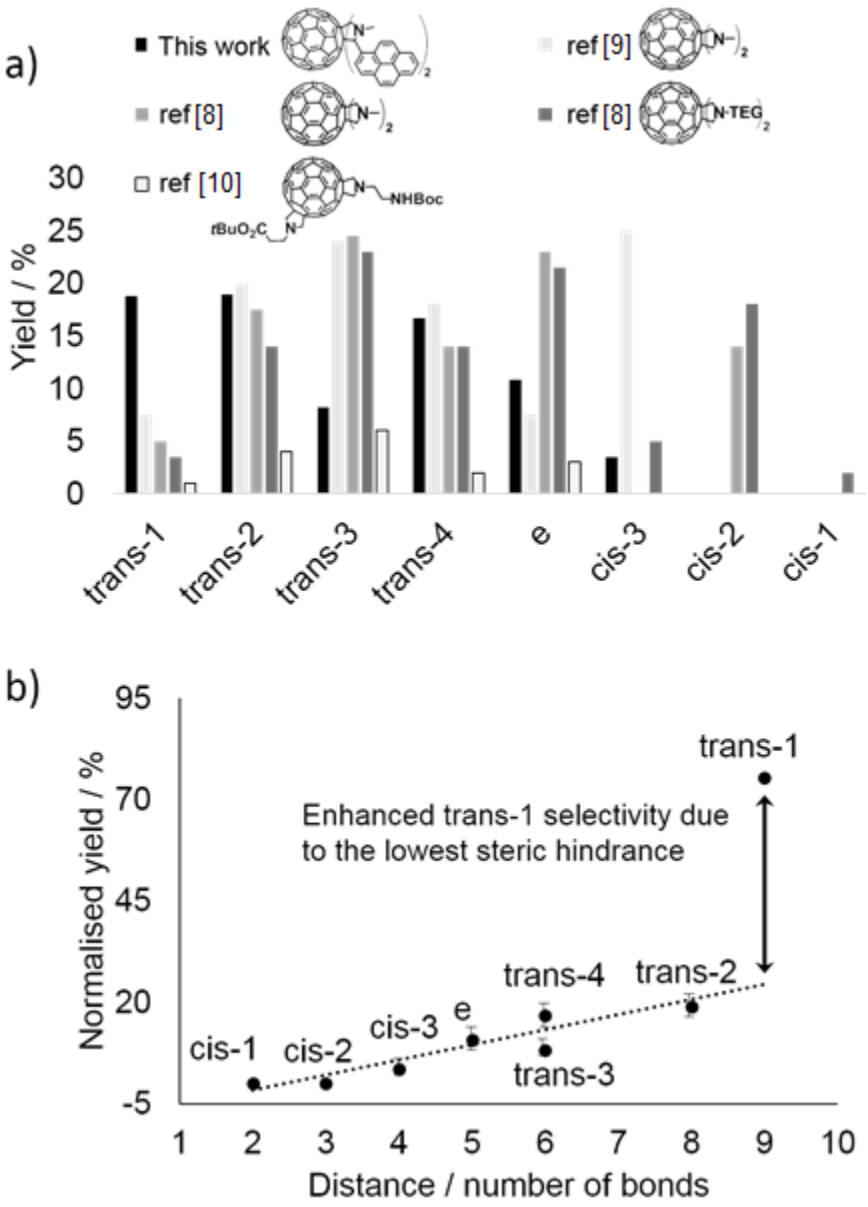

Figure 15: a) The yields of each of the regioisomers in the Prato reaction containing bulky pyrene groups in comparison with the similar reactions with smaller substituents reported previously (N-Methyl [34, 38], N-tetraethyleneglycol (TEG) [34], and a mixed N-substituted derivative [39]. b) A correlation between the distance between the addends on the C_{60} cage (displayed as the smallest number of bonds) and the corresponding regioisomer yield, showing a near linear trend.

are preferred. I assume this to be because the pyrene groups are well spaced and there is the least steric hinderance. The normalised yield of the trans-1 isomer is particularly remarkable, especially in light of the fact that previous studies report trans-1 as a minor product with one of, if not the, lowest yields of all of the regioisomers (Figure 15 a). This is attributed to the steric influence of the bulky pyrene groups enhancing the stability of this isomer where those groups are most separated. The converse is true for the equatorial and cis-3 adducts, which are usually one of the major products of the reaction but are observed in a much lower yield due to the steric repulsion of the bulky pyrene groups, thus demonstrating a degree of regioselectivity for well separated functional groups [34, 38]. Curiously, the yield of the trans-3 isomer is also markedly reduced from that observed in previous reactions. This cannot be explained by only considering the relative positions of the bulky pyrene groups and so there must be some additional effect controlling the relative yield of different regioisomers.

For this reaction there is a positive correlation between the normalised yield of the regioisomer and the distance between the functional groups on the fullerene cage, as displayed in Figure 15 b. A good agreement is observed for a linear correlation between normalised yield and the distance between functional groups for the isomers cis-1, cis-3, cis-3, e, trans-4 and trans-2. However, the trans-1 isomer displayed a dramatically enhanced normalised yield compared to the linear correlation, which can be understood by considering the origin of the positive trend

line. Steric hindrance is the dominant factor in determining the normalised yield in these isomers, which also goes a long way towards explaining the selectivity towards the trans-1 isomer. Again, the isomer trans-3 displays lower yields than the trend predicts, necessitating a closer look at this isomer to determine the reasons that the yield would be lower than has been observed previously and is predicted from our consideration of the sterics of the reaction. To this end, DFT modelling was carried out by Dr. G Volonakis on the isomers to determine if there was any difference in the predicted stability of these molecules (see A1 for further details). The most significant result of this modelling was that a shorter, and so less reactive, [6,6] bond is predicted at the trans-3 site compared to the other trans isomers. This change in bond length could explain a change in the reactivity of the trans-3 site and so a markedly different yield of the trans-3 isomer. All isomers except for the trans-3 and cis-3 display the same bond length, confirming that sterics are the main factor governing the product distribution in this reaction rather than the bond reactivities.

2.5 Endohedral fullerenes

Having studied the reaction to attach two pyrene groups to C_{60}, it would be beneficial to extend that reaction to endohedral fullerenes in order to create materials with more novel and exotic properties. There is ample evidence for successful 1,3 dipolar cyclo-addition reactions on both the endohedral fullerenes $Sc_3N@C_{80}$

[40, 41, 42] and $Sc_3C_2@C_{80}$ [43] under similar reaction conditions to those described above; namely as a one-pot reaction in toluene or ortho-dicholorobenzene (O-DCB) refluxed at between 110°C and 130°C. I chose these fullerenes to provide two molecules of similar size and mass but drastically different electron paramagnetic resonance (EPR) properties, with $Sc_3N@C_{80}$ being a spin silent molecule while $Sc_3C_2@C_{80}$ is spin active with unpaired electrons in the central cluster. However, the signal of these unpaired electrons is split by a hyper-fine coupling to each scandium atom which has a nuclear spin of I = 7/2, see Figure 16. There are 22 lines as each scandium atom contributes I = 7/2 for a total of I = 21/2 and in EPR there are a number of lines, L = 2I + 1. From the fullerene I expect to see only 22 equally spaced lines which increase and decrease with a Gaussian distribution. However, in Figure 16 a I also observe additional features at a lower magnetic field as well as a change in the distribution of the peaks. The additional lines at lower fields can be explained by a copper impurity which has been observed in other samples in our laboratory. This also goes a long way towards explaining the change in distribution of the lines seen. However, simulations show that this is not sufficient to explain the perturbation. It is believed that, in addition to the copper, there are small impurities in the fullerene sample in the form of other scandium containing fullerene cages such as $Sc@C_{82}$.

The highly symmetrical nature of the $Sc_3C_2@C_{80}$ EPR signal is due to the fact that the spin density is equally distributed between all of the scandium atoms.

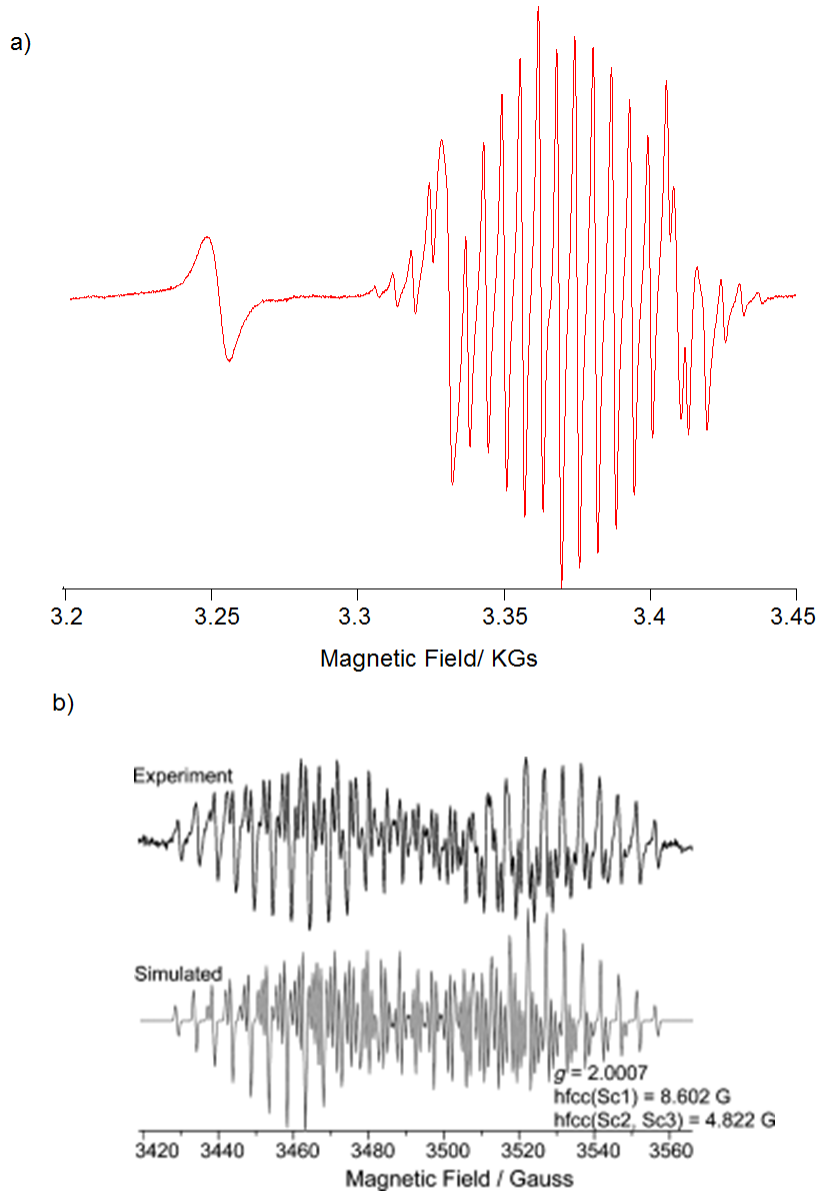

Figure 16: a) The 22 EPR lines which I observe in a sample of unreacted $Sc_3C_2@C_{80}$ are recorded in toluene solution at 298 K (9.862435 GHz frequency, 0.0003170 mW microwave power, 0.0022 G modulation amplitude, 10.00 kHz modulation frequency, 4 scans). b) The observed and simulated EPR spectrum for a mono-functionalized $Sc_3C_2@C_{80}$ molecule, showing different hyperfine coupling constants.

However, if these fullerenes are to be used in devices then it is necessary for them to be functionalized. For a monoadduct of $Sc_3C_2@C_{80}$ functionalized by the prato reaction with very simple reagents, the spin density remained localised entirely on the scandium cluster, with none delocalised into the fullerene cage. However, the functionalization did lead to distortions of the cage, changing the molecules symmetry from C_{3v} to C_{2v}, leading to a re-distribution of spin density between the scandium atoms, with an enhanced spin density on the scandium atom at the greatest distance from the functional group and the distortion to the fullerene cage [47]. This change in spin density at one of the scandium atoms leads to a significant change to the EPR spectrum of the molecule. This is because the hyper-fine coupling constant (hfcc) experienced by each scandium atom depends on the spin density at the scandium atom, giving rise to two different hfcc values of 8.602 G for one scandium atom and 4.822 G for the other two, this is in contrast to the 6.256 G observed for all scandium atoms in the unfunctionalized cage [47, 48].

It is also believed that the free rotation of the Sc_3C_2 cluster within the fullerene cage assists in creating the highly symmetrical EPR spectrum of pristine $Sc_3C_2@C_{80}$ [48]. The inhomogeneous distribution of spin density, which is caused by the position of the functional group, is believed to be compounded by the functional group preventing free rotation of the endohedral cluster. This prevents the spin density from being re-distributed equally across all of the scandium atoms on the EPR timescale, giving rise to the different hfccs and so the splitting pattern seen.

This contrasts with EPR measurements that have been made on another functionalized endohedral fullerene cage where the prato monoadduct of $Y_3N@C_{80}$ was shown to be EPR active with a similar hfcc pattern of 6.26 G (two nuclei) and 1.35 G (one nucleus), which is again due to the chemical functionalization causing spin density to be distributed away from the functional group [49]. However, in this molecule the spin was shown to be delocalized across both on the fullerene cage and the internal Y_3N cluster [49], which would have major implications for the use of this molecule in spintronic applications as the well isolated spin is what makes endohedral fullerenes so appealing for use in this field.

All literature suggests that the endohedral fullerenes should have extremely similar reactivity to each other and to the empty cages, so I first attempted the reaction with the same reagents and stoichiometry as with empty cages on the fullerene $Sc_3N@C_{80}$ in the solvent O-DCB. This reaction was able to successfully produce a bis-functionalized product only once the stoichiometry was increased to 1:8:20 for the fullerene:aldehyde:amino acid and allowed to proceed for just 90 minutes. Extending the reaction length only led to an increase in the yield of multiadducts while reducing the quantities of the aldehyde and amino acid prevented the reaction from proceeding [38, 39, 45]. By optimising the reaction conditions it was possible to achieve a production of the bisadduct with approximately 25 % yield, the bisadduct was confirmed by mass spectrometry, see Figure 17 a.

However, when I extended the reaction to the fullerene $Sc_3C_2@C_{80}$ it was not

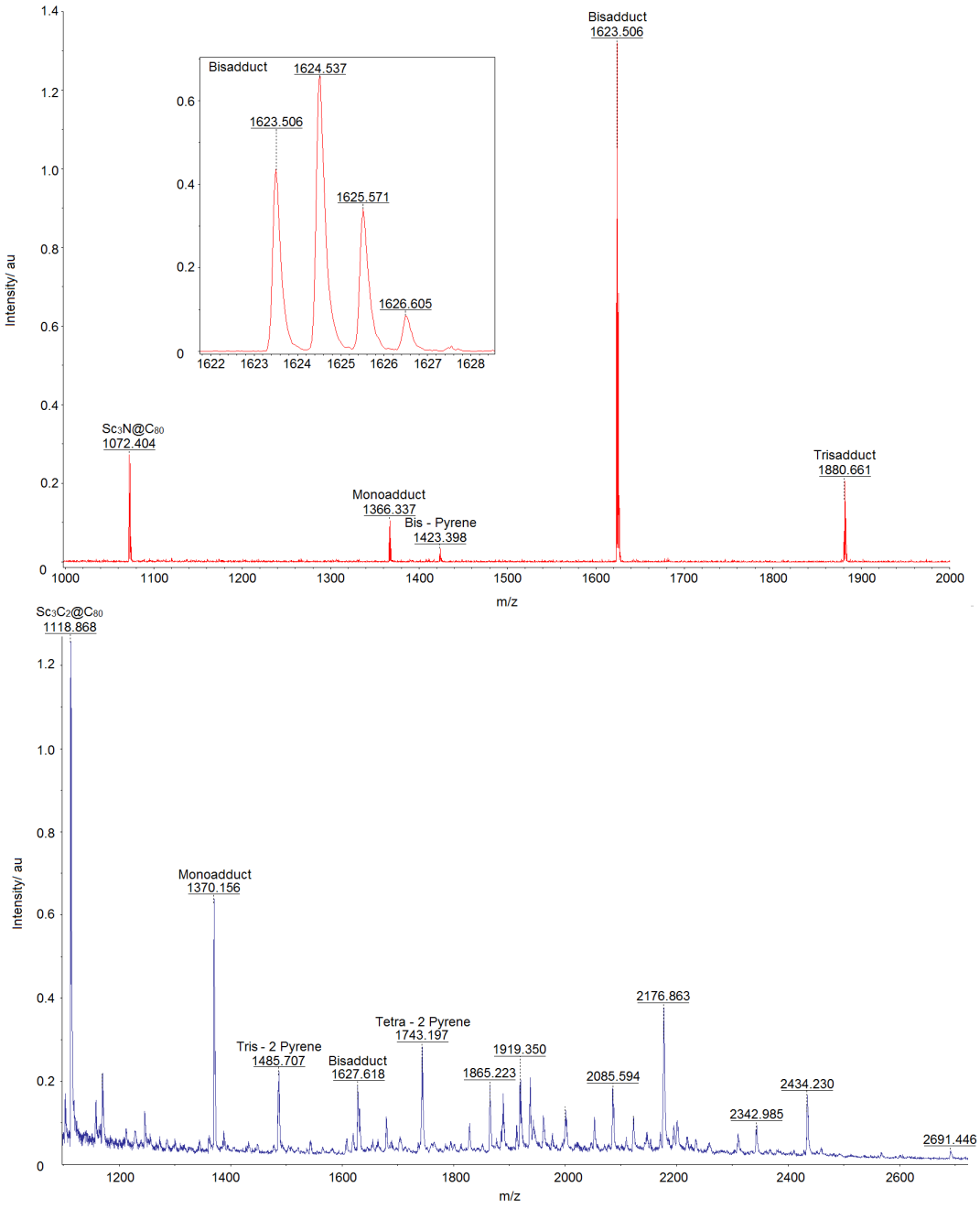

Figure 17: Mass spectra of the products from the reaction between pyrene-1-carboxaldehyde, and N-methylglycine and a) $Sc_3N@C_{80}$ and b) $Sc_3C_2@C_{80}$.

successful. The greatest yield of bisadduct was seen after running the reaction for 96 hours and at this time the most intense peak seen in the mass spectra was still the unfunctionalized fullerene. In addition to there being a low yield of the bisadduct there were also a large quantity of products observed with a mass greater than that of the bisadduct, see Figure 17 b. It is clear that some of these peaks are due to fullerenes that have had more than two additions to the cage. However, either the pyrene group has broken off due to the intense conditions of the mass-spectrometer, which can be observed in Figure 17 a as well, or there have been additions to the cage that have taken place in the absence of the pyrene group, potentially due to reagents breaking down over the long duration of the reaction. When comparing the mass spectra between the two reactions it is clear that there is a much greater degree of fragmentation in the $Sc_3C_2@C_{80}$ reaction than the $Sc_3N@C_{80}$ reaction, which leads me to conclude that the reagents have broken down over the course of the reaction and I decided not to assign the peaks with a m/z in excess of 1800.

Cyclic voltammetry (CV) is an electrochemical technique which is used to measure the oxidation and reduction potentials of a molecule relative to a known electrochemical potential, allowing us to determine information about the energy levels close in energy to the HOMO and LUMO levels of the molecule. The molecule under examination is solvated with Ferrocene, the known reference potential, and the electrolyte $[NaBu_4][BF_4]$ in dicholoromethane. A voltage is then

applied to the solution which is ramped, at a constant rate, first up then down and back to the starting voltage, see Figure 18 a. The current is measured throughout this voltage sweep and, when the voltage aligns with an oxidation or reduction potential, the magnitude of the current increases as electrons pass to or from the molecules. CV was used to examine the products of the successful functionalization of the $Sc_3N@C_{80}$ cage to determine what, if any, change occurs in the energy of the molecular orbitals of the molecule upon functionalization. The changes were observed on functionalization to a monoadduct and then to a bisadduct, with the current for these compared to the unfucntionalized $Sc_3N@C_{80}$ shown in Figure 18 b. The CV experiment shows five clear features. Starting at the right-most feature I observe the known ferrocene signal, which will be used as a reference for all other observed features. There are then four more reduction peaks, including one which was observed in the background trace with only ferrocene present, thus I assign 3 reduction potentials which are due to the endohedral fullerene bisadduct. The position of these peaks for the unfunctionalized $Sc_3N@C_{80}$as well as the pyrene functionalized monoadduct and bisadduct are summarised in Table 6.

The reduction potentials are summarised in Table 6 for all of the molecules that I investigated by CV and are broadly in agreement with previous studies on the electrochemical properties of functionalized $Sc_3N@C_{80}$. I observe a small, but consistent, shift in the reduction potentials upon functionalization [50]. However, the shift seen is very minor, indicating that the energy of the LUMO, LUMO-1

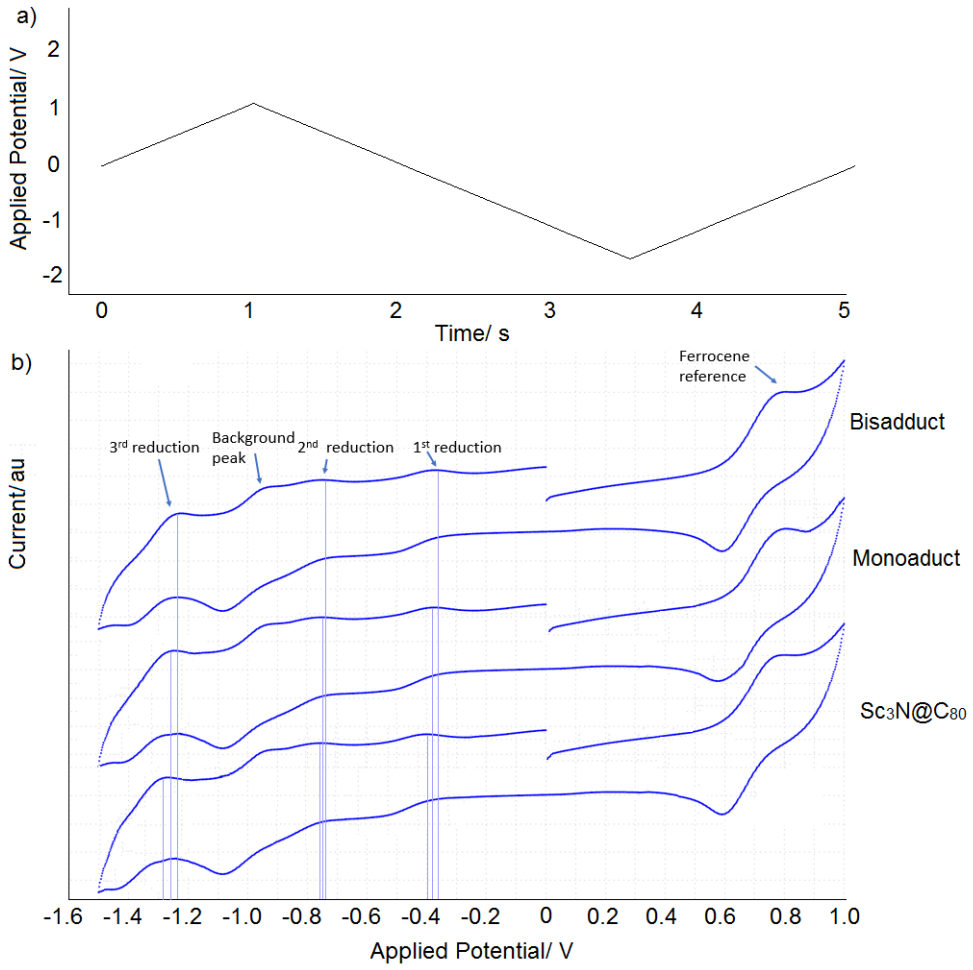

Figure 18: a) The voltage sweep at 0.1 V/s for the CV experiment performed in b) on the unfunctionalized $Sc_3N@C_{80}$as well as the pyrene functionalized monoadduct and bisadduct. This shows a small but consistent change in each of the redox features of the molecule which the background and ferrocene peaks remain unchanged.

Molecule	Reduction potential /V vs Fc/Fc^+		
	1st	2nd	3rd
$Sc_3N@C_{80}$	-1.215	-1.545	-2.280
$Sc_3N@C_{80}$ Monoadduct	-1.195	-1.550	-2.125
$Sc_3N@C_{80}$ Bisadduct	-1.165	-1.555	-2.010

Table 6: Position of electrochemical features of the pristine, mono-functionalized and bis-functionalized endohedral fullerene $Sc_3N@C_{80}$.

and LUMO-2 levels does not change to a great extent upon functionalization, even if the spatial distribution of electron density does change upon functionalization. The changes to the molecular orbitals are all to decrease how negative in energy they are, in agreement with previous studies, showing a reproducible trend on functionalization of the [5,6] bonds in $M_3N@C_{80}$ fullerenes [50].

Because of the difficulties experienced producing large quantities of the bis-pyrene functionalized $Sc_3C_2@C_{80}$ with sarcosine as the amino acid I decided to move to amino hexadecanoic acid (AHDA). AHDA has a long alkyl group, which makes it significantly more soluble in organic solvents than sarcosine and will thus lead to significantly more soluble final products. The reaction was successfully performed on the fullerene C_{60} in order to better understand the changes in reactivity of fullerenes with ADHA and to confirm that AHDA does increase the solubility of the products. However, when I extended the reaction to the fullerene $Sc_3N@C_{80}$ it was not possible to get the reaction to proceed with either toluene or O-DCB as the solvent or at a wide range of temperatures. Due to time constraints it was not possible for me to continue to investigate the reaction with AHDA.

2.6 Conclusion

I have studied the 1,3 dipolar cycloaddition reactions between pyrene-1-carboxaldehyde, sarcosine and the fullerenes C_{60} and C_{70} with the bulky planar aromatic pyrene group, which is significantly bulkier than has been studied previously in this reaction.

For the reactions carried out on C_{60} and C_{70} with identical stoichiometry, the data supports the commonly held trend that larger fullerene cages are less reactive than smaller fullerene cages, with both k_2 and k_3 being approximately half as large in C_{70} as in C_{60}. This is understood by a decrease in the bond strain in larger fullerenes due to them having less curvature. The ratio between the reaction rates for the formation of mono and bisadducts are equal, within experimental tolerance, so the change in reactivity between the two cages can be assumed to be identical for both the formation of mono and bisadducts.

For the reactions on C_{60} with varying stoichiometry I found that the quantity of sarcosine had very little effect on the value of the rate constants. However, the rate constants increase in a linear fashion with increasing quantity of pyrene-1-carboxaldehyde. Within experimental error both k_2 and k_3 appear to be first order with respect to the pyrene-1-carboxaldehyde.

I have synthesised six novel regioisomeric [60]fulleropyrrolidine bisadducts containing pyrene functional groups and isolated them by extensive HPLC and thoroughly characterised them, primarily by UV-Vis spectroscopy. The functional

group used in this research is significantly bulkier than reported in any previous studies and consequently steric hindrance has a significant effect on the distribution of products and the reaction times at which different products are generated. The most favourable product, the trans-1 isomer was produced at greatest quantities at long reaction times while the percentage of trans-4 and equatorial isomers in the bisadduct peak decreased. This is thought to be because long reaction times favour the decay of less favourable regioisomers into the most favourable trans-1 isomer. The final yield of the reaction favours the formation of the trans-1 isomer, where there is the greatest distance between pyrene groups. This is in contrast with the previous studies which report the trans-3 or cis-3 isomers as the most abundant. This hypothesis is corroborated by a low observed yield of the trans-3 and cis-3 isomers, and a complete absence of cis-2 and cis-1 isomers, all of which have significantly closer pyrene groups.

An anomalously low yield of the trans-3 isomer cannot be explained by sterics and is instead understood by noting a shorter simulated bond length for the trans-3 reaction site, which implies that thermodynamics has an effect on the distribution of regioisomers, as well as the more dominant steric effects. It is necessary to comprehend and control regioselectivity in bis-additions on the fullerene cage if this class of materials is to be of use in the fields of photovoltaics, electronic devices and sensors. The pyrene functional group makes an ideal candidate for studying this reaction as it both provides functionality in and of itself but

also acts as a model to better understand the bis-addition patterns with other bulky functional groups. These include, but are not limited to, transition metal complexes, redox and magnetically active organic units and radicals. All of these would allow for the creation of novel materials with potentially unique and useful properties.

3 Properties of functionalized fullerenes

Having studied the kinetics of the reaction and produced a range of regio-isomers it is possible to study the properties of the functionalized fullerenes. They were found to display a range of interesting photochemical properties. Of particular note is the ability to tune the photosensitising of the singlet oxygen radical, which has implications for the use of fullerenes for biomedical applications.

3.1 Introduction

It is essential to attach functional groups to the surface of fullerene cages to alter or enhance their properties in addition to expanding their range of applications. Examples of this vary dramatically from the necessity to create water-soluble fullerenes for medical applications [51] to tuning the properties of the fullerene in solar cells [16].

As discussed in Chapter 2, the reaction used produces a range of fulleropyrrolidines, with the exact nature of the final product dictated by the choice of amino acid and aldehyde. I chose the amino acid sarcosine for its simplicity and the properties of the final product were influenced by using pyrene-1-carboxaldehyde. I chose the pyrene functional group so that the fullerene, once functionalized with two such groups, could successfully bridge a graphene nano-gap using π-π stacking interactions, see Chapter 5. However, the molecule and the reaction were found to be interesting in their own rights.

Fullerenes and their derivatives have been employed for their electron accepting properties [16] and are known to form donor–acceptor complexes [52] and dyads [53, 54, 55] which exhibit photoluminescence emissions of low intensity, and an intersystem crossing (ISC) to a triplet state. Such donor–acceptor dyads as fullerene-porphyrins [54] and fullerene-pyrenes [55] have been studied in detail. DFT studies of pyrene monoadducts indicate that the HOMO level of the molecule is localised to the pyrene donor and, conversely, that the LUMO level is localised to the fullerene acceptor [56]. Therefore, the act of functionalizing the fullerene has a profound effect on the photophysical properties of the system, resulting in charge separated states as well as changes to the intersystem crossing (ISC) lifetimes and singlet–triplet populations. The ability to influence and control these properties is crucial for a number of applications. For example, the charge separated states of donor–acceptor dyads can find use in cell membrane potentials and ion transport control [57]. It is also know that the ISC is crucial in making fullerenes the most efficient known photosensitisers for the generation of the excited singlet oxygen state $^1O_2$, as the triplet excitation can transfer from the fullerene to the oxygen ground state [58].

During the course of studying this reaction I was also able to make several observations on the kinetics of the reaction, see Chapter 2. By then studying the NIR photoluminescence (PL) spectra of C_{60} and C_{70} mono and bisadducts, along with the singlet oxygen generation, I was able to observe dramatic differences.

UV-Visible absorption was used to confirm that there was no unreacted pyrene-1-carboxaldehyde in the sample and also showed that the C_{70} bisadduct has the greatest disruption to the conjugation of the fullerene molecule. High energy PL was performed to study the florescence of the pyrene unit and shows a difference arising from symmetry reduction between the C_{60} mono and bisadducts, with the former favouring an intra-level transition while the later favours an inter-level transition. Similar behaviour was also observed in low energy PL which targeted the fullerene emission. All functionalized fullerenes also displayed lower quantum yields for the pyrene fluorescence than the precursor molecule when targeting the pyrene emission. However, when targeting the fullerene emissions an opposite effect is observed between C_{60} and C_{70}, with a four-fold enhancement of the quantum yield observed in the C_{60} monoadduct versus the pristine fullerene as opposed to a quantum yield which is half that of the pristine fullerene for the C_{70} monoadduct.

Because of these differences I decided to study the PL lifetimes of the different molecules. C_{60} mono and C_{70} bisadducts displayed a single pathway decay mechanism and a reduced singlet oxygen generation compared to C_{60} bis and C_{70} monoadducts, which had a two pathway decay mechanism and a greater singlet oxygen production [14]. I attribute these differences to the formation of either locally excited or charge separated states. Fullerenes are known to be sensitisers for the generation of singlet oxygen. When the ability of the functionalized fullerenes

to generate singlet oxygen was studied, it was found that the C_{60} mono and C_{70} bisadducts displayed a dramatic reduction in singlet oxygen generation. As singlet oxygen is harmful to the human body [59], these could be of huge importance for the application of fullerenes to medical research.

3.2 Photochemistry

The properties observed are primarily a variety of photochemical properties. However, this constitutes a range of behaviours as will be seen in this chapter.

3.2.1 UV-Visible Absorption

From UV-Visible (UV-Vis) absoption, information about the conjugation of the fullerene cage can be deduced. In particular, the monoadducts of C_{60} display a characteristic signal at 430 nm. The spectra of the fullerenes, their monoadducts, bisadducts and the pyrene-1-carboxaldehyde precursor, using the concentrations listed in Chapter 1, are displayed in Figure 19. The pyrene features at 396 nm, 375 nm and 365 nm are blue-shifted for all of the functionalized fullerenes due to the interaction between the pyrene unit and the fullerene cage. This interaction is better understood by considering the PL data below.

The 396 nm peak is missing in all cases, demonstrating that the only pyrene groups present are those chemically bonded to the fullerene, ie. that there are no physisorbed pyrene molecules in the sample. The C_{60} monoadduct displays a peak at 430 nm, which is typical of mono-functionalized C_{60} molecules [60] and

both functionalized C_{60} molecules show the fullerene peak blue shifted due to the extension of the π conjugated system on functionalization. The C_{70} adducts show the greatest deviation in the 472 nm fullerene peak and the greatest quenching of the fullerene peak is seen in the C_{70} bisadduct, while the monoadduct shows a slight enhancement of this peak. This fullerene peak is known to be enhanced by interactions with triplet oxygen, implying that the C_{70} bisadduct will be a poor photosensitiser for singlet oxygen while the monoadduct may be a better photosensitiser than the pristine fullerene [61].

3.2.2 High Energy Photoluminescence Spectroscopy

I chose PL spectroscopy at high energy (300-450 nm) excitations to target the absorption of the pyrene unit. The pyrene spectrum is extremely complicated and depends on the choice of solvent, functionalization of the molecule and the dielectic environment. It is possible to observe both the excited dimer, D_e, and the excited monomer D_m with both radiative, rate k_r, and non-radiative, rate k_n, processes affecting these states. These are heavily influenced by nearby molecules, for example surfactants in micellar sollutions [62]. In the pyrene-1-carboxaldehyde PL spectra, see Figure 20 a and b, the D_m to ground transition is observed with an emission wavelength of 425 nm while D_e to ground is observed with an emission wavelength of 490 nm.

For the pyrene containing fullerene compounds I observed significant differ-

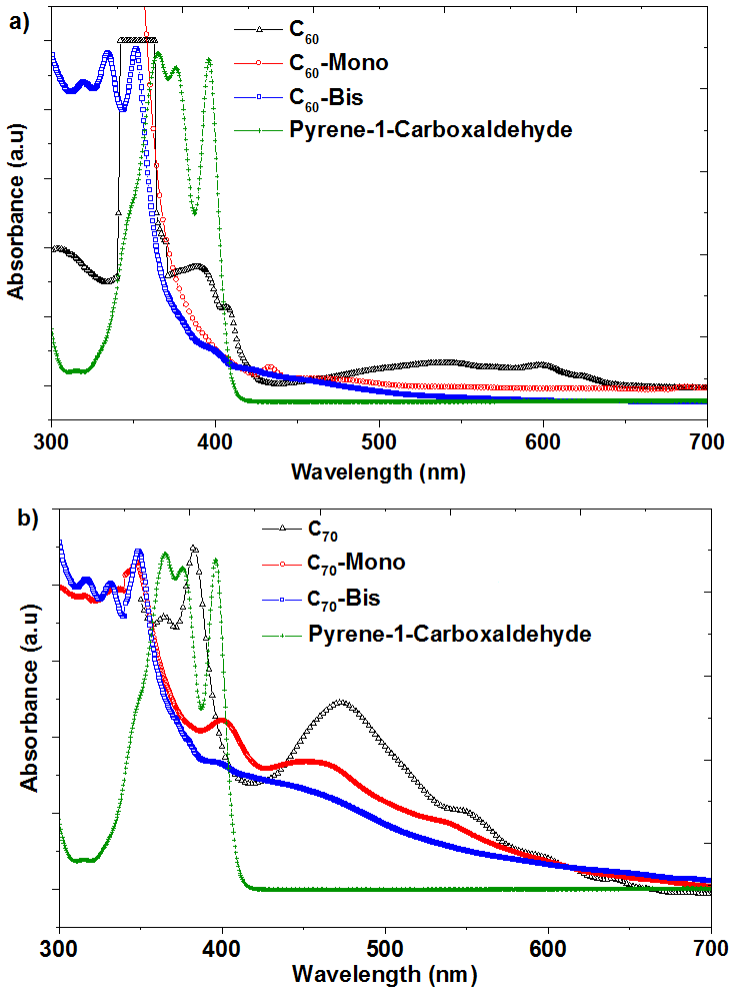

Figure 19: UV-Vis absorbance spectra of the mono and bisadducts of (a) C_{60} and (b) C_{70}, in toluene solutions. Shown in green, the spectrum of the pyrene-1-carboxaldehyde precursor molecule. The spectra of the precursor molecule can also be seen in the solvents ethanol and toluene in Figure A12.

ences. Both C_{60} mono and bisadducts show double peaks, indicating a vibronic influence on the spectrum. This effect is opposite for the two adducts with the monoadduct showing greatest intensity for the higher energy peak while the bisadduct shows a greater intensity for the lower energy peak. The vibronic effects can be explained by a reduction in symmetry of the molecule on functionalization with a fullerene. This leads to an intra-level transition for the monoadduct, which has been observed previously [68], and an inter-level transition for the bisadduct, as shown in Figure 20 c. C_{70} features are better observed in the red region and are discussed in Chapter 3.2.3 below. The quantum yield of the pyrene emission is reduced dramatically in all fullerene functionalized molecules as displayed in Table 7.

3.2.3 Low Energy Photoluminescence Spectroscopy

I carried out measurements with lower energy excitations, in the range 450 nm to 530 nm, to target the absorption of the fullerene cage. Fullerene photochemistry is dominated by long-lived radiative transitions with an ISC to a triplet state. These typically give weak emissions and low quantum yields [65]. On the addition of pyrene groups, the C_{60} S_1- S_0 transition narrowed and both the absorption and emission were shifted, from 495 nm and 715 nm in C_{60} to 470 nm and 711 nm for the monoadduct and 467 nm and 719 nm for the bisadduct, see Figure 21 a. Similar shifts been reported for functionalized fullerene molecules in prior work

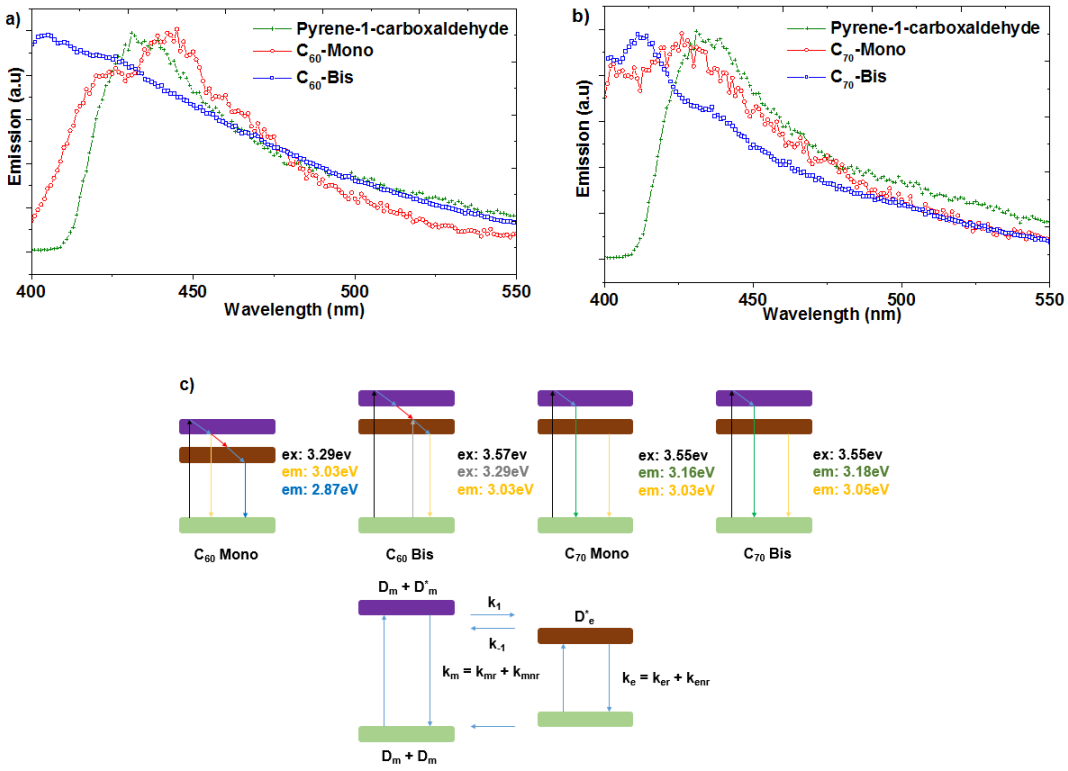

Figure 20: Normalized photoluminescence spectra when excited at 345 nm for a) C_{60} derivatives b) C_{70} derivatives. c) Both the excitation and decay pathways for all fullerene adducts and a suggested scheme of the excimer formation in pyrene where D_e is the excimer, D_m the monomer, and k_r and k_n the radiative and non-radiative decay constants respectively.

Reference (excitation)	Quantum yield/ %	Sample (excitation)	Quantum yield/ %
Pyrene in ethanol (335 nm)	65	C_{60} mono (335 nm)	1
Pyrene in toluene (335 nm)	19	C_{70} mono(335 nm)	0.12
C_{60}(520 nm)	0.022	C_{60} mono (520 nm)	0.09
C_{70}(520 nm)	0.054	C_{70} mono (520 nm)	0.03

Table 7: A summary of the quantum yields for two different excitation wavelengths where 335 nm targets the pyrene unit and 520 nm targets the fullerene cage.

[66]. The increase in fluorescence intensity on the addition of pyrene groups is explained by a reduction in symmetry of the fullerene from I_h for the pristine C_{60} to C_{2v} for monoadducts to C_1, C_2 or C_s for bisadducts. This reduction in symmetry leads to a reduced rate constant for the ISC due to an increased favourability for intramolecular charge transfer [67]. This charge transfer has been previously demonstrated from the first excited singlet state of the pyrene donor molecule to the S_1 state of the fullerene in a fullerene-pyrene monoadduct [68].

Functionalized C_{70} is comparable to C_{60}, displaying similar electronic structure as well as singlet and triplet levels. Both mono and bis-functionalized C_{70} display a red-shifted S_1- S_0 transition at 707 nm compared to the pristine fullerene at 667 nm and, as in C_{60}, the absorptions were also shifted to lower wavelengths, see Figure 21 b. The quantum yield of the C_{70} monoadduct is half that of the pristine fullerene, while the opposite effect is seen in the C_{60} monoadduct, with a quantum yield quadruple that of the pristine fullerene, as seen in Table 7.

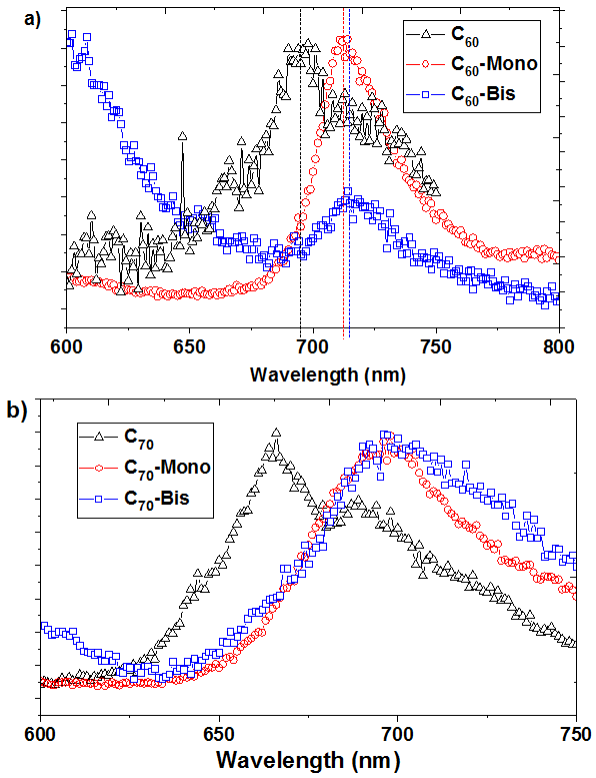

Figure 21: Photoluminescence spectra under 488 nm excitation for the a) C_{60} derivatives and b) C_{70} derivatives.

3.2.4 Time Resolved Photoluminescence

In order to better understand the differences between the photochemistry of these molecules I measured the the photoluminescence lifetimes with an excitation wavelength of 395 nm. In all cases higher wavelength emissions displayed lower intensities as well as longer emission lifetimes. For C_{60}, the monoadduct displays a monoexponential decay profile and has a shorter decay lifetime than the bisadduct, which has a biexponential decay profile. The opposite trend is displayed in C_{70}, with the monoadduct displaying a biexponential decay profile and a longer lifetime than the bisadduct with a monoexponential decay profile. These decays are shown in Figure 22 and summarised in Table 8.

The biexponential decay means that there are two decay mechanisms occurring, with prior work suggesting that the additional pathway is due to a long-lived charge separated state in addition to the locally excited state which is present in all cases [64], as shown in Figure 22 e. The differences between the two fullerenes are attributed to the different energy levels and symmetry of each fullerene. These differences also affect the favourability of the charge separated state, leading to it being present with two pyrene groups in C_{60} but only one in C_{70}.

The PL lifetime of the unreacted pyrene-1-carboxaldehyde displayed an additional weak fluorescence at 552 nm with a lifetime of 14 ns which was absent in all fullerene containing molecules. This confirms that an intramolecular charge transfer occurs from the pyrene to the fullerene as opposed to an ISC which occurs

Sample	t1/ ns	t2/ ns	Sample	t1/ ns	t2/ ns
C_{60} mono 430 nm	1.43	n/a	C_{70}mono 452 nm	0.27	1.71
C_{60}mono 459 nm	1.50	n/a	C_{70}bis 430 nm	1.44	n/a
C_{60}mono 500 nm	1.68	n/a	C_{70}bis 460 nm	1.47	n/a
C_{60}bis 462 nm	0.54	2.54	C_{70}bis 490 nm	1.62	n/a
C_{60}bis 502 nm	0.63	2.89			
C_{60}bis 550 nm	0.64	3			

Table 8: The lifetime values of the different derivatives as estimated by time resolved fluorescence spectroscopy. The shorter lifetime corresponds to the locally excited state [64].

in the pyrene unit.

3.2.5 Singlet Oxygen Sensitising

Oxygen radicals, such as $^1\Delta_g$, also known as singlet oxygen, are potent biocides [59]. Control over singlet oxygen generation is therefore vital if fullerenes are to find use in various medical applications, either by eliminating their photosensitising power or by directing the singlet oxygen to cancerous cells [69]. It was necessary to record these measurements in the solvent CS_2 rather than toluene as the oxygen radical is quenched by toluene, leading to the formation of toluene radicals. The singlet oxygen generation is studied in these experiments by observing the phosphorescence of the oxygen radical at 1270 nm in the NIR (Near infra-red) region. The singlet oxygen signal is measured with high intensity for both the C_{60} and C_{70} fullerenes [14].

The PL maps in Figure 23 were generated by exciting the samples of a known concentration with a range of wavelengths and measuring the emission spectrum

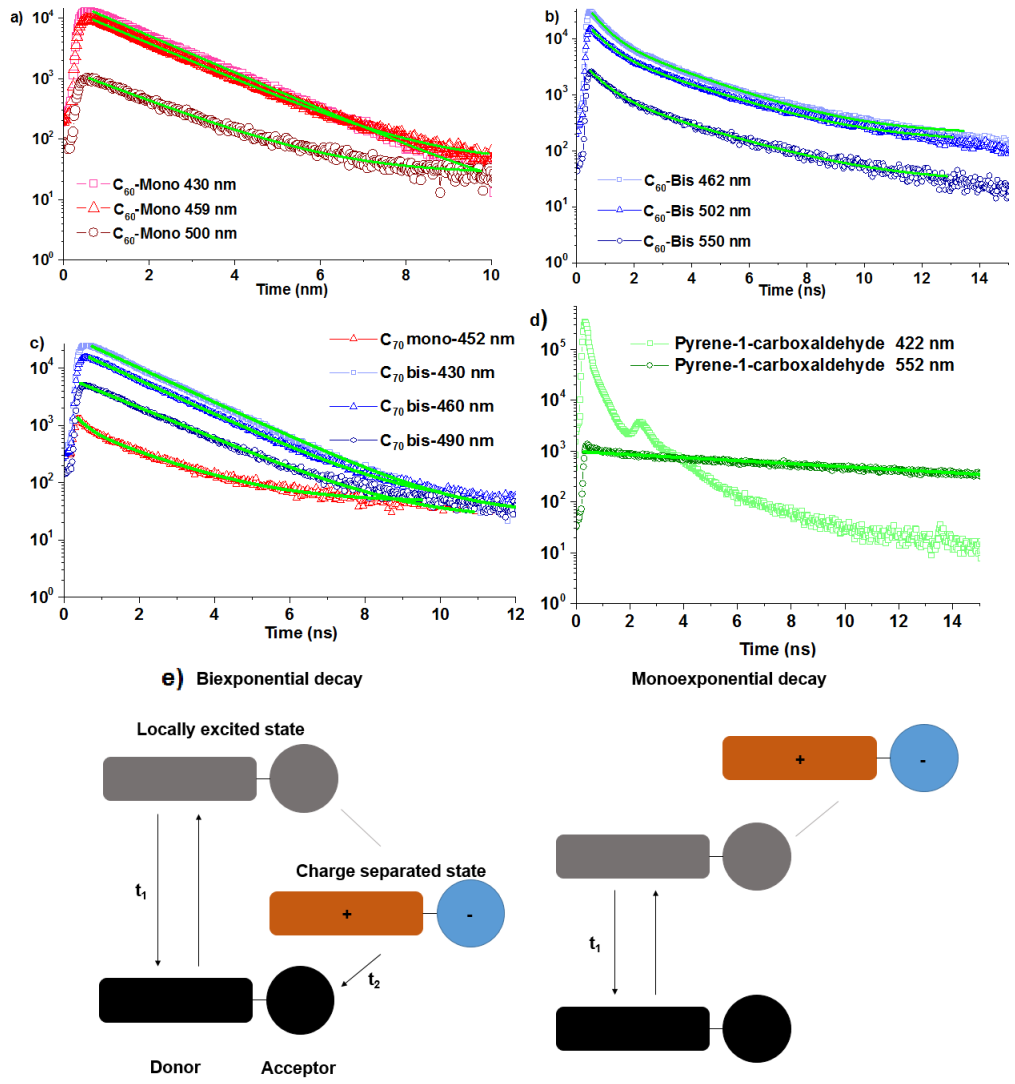

Figure 22: Photoluminescence lifetime measurements under 395 nm laser excitation for a) the C_{60} monoadduct, b) C_{60} bisadduct, c) C_{70} mono and bisadduct and d) pyrene-1-carboxaldehyde. In the C_{60} bisadduct and the C_{70} monoadduct we observe biexponential decay and so derive two different decay lifetimes. For the C_{60} monoadduct and the C_{70} bisadduct we instead observe a monoexponential decay mechanism. The monoexponential decay was fitted with the equation $y = A_1 e^{-(x/t_1)}$ and the biexponential decay was fitted to $y = A_1 e^{(-x/t_1)} + A_2 e^{(-x/t_2)} + y_0$ with the fitted curves shown as green lines. e) The proposed decay mechanisms which lead to biexponential and monoexponential decay. In the former, both the locally excited and charge separated states can emit a photon to return to the ground state. Whereas, in the latter, the charge separated state can only decay to the locally excited state by non-radiative processes and the decay from the locally excited state to the ground state is the only radiative process.

at each. The measurements in Figure 23 a and b, II to V, use samples of identical concentration, $3x10^{-5}$ g/ml, while the sample in I is twice this concentration, $6x10^{-5}$ g/ml. These measurements allowed me to see both the wavelengths that the sample can emit at and the corresponding excitation wavelength required to produce this for a range of samples. When studying the C_{60} monoadduct at a concentration of $3x10^{-5}$ g/ml in Figure 23 a I, it was not possible to see any emission from the singlet oxygen at 1270 nm, it was only by moving to a more concentrated sample, Figure 23 a II, that this emission could be seen, showing that the C_{60} monoadduct is a poor sensitiser for singlet oxygen. The C_{60} bisadduct and the C_{70} monoadduct (Figure 23 a III and IV) show strong signals at 1270 nm, suggesting that they are good sentitisers of singlet oxygen. The C_{70} bisadduct does display a visible signal at 1270, Figure 23 a V, though it is considerably less intense than the C_{60} bisadduct or the C_{70} monoadduct, showing that the C_{70} bisadduct is a comparatively poor sensitiser of singlet oxygen. By looking at Figure 23 b it is possible to see that the C_{60} monoadduct and bisadduct and the C_{70} monoadduct all require excitation at the same wavelength of 460 nm to cause the singlet oxygen emission. However, the C_{70} bisadduct requires an excitation at 560 nm, suggesting that there may be some differences in the mechanism by which the C_{70} bisadduct sensitises the singlet oxygen radical.

Previous studies have shown that charge separated states in similar fullerene complexes can result in saturation of the triplet state from charge recombination

[70]. The photosensitising of singlet oxygen takes place via energy transfer through the triplet state, therefore a strong singlet oxygen signal is associated with a charge separated state that has a long lifetime, while the opposite behaviour is associated with forbidden intersystem crossings and a high quantum yield of the S_1 - S_0 transition.

For the C_{60} mono and bisadducts as well as the C_{70} bisadduct the maximum intensity of the singlet oxygen emission is observed for an excitation wavelength of 474 nm. For the C_{70} monoadduct the maximum intensity is observed at an excitation wavelength of 556 nm indicating that the process of oxygen sensitising is only changed in the C_{70} monoadduct.

3.3 Conclusion

The optical and photosensitizing properties of fullerene pyrollidines were found to vary with the number of pyrene groups attached to the molecule in addition to the size and shape of the fullerene cage, which I observed with C_{60} and C_{70}. The first evidence for this is found in the UV-visible spectra of the molecules, with differences in the intensity of the fullerene peak implying that, for C_{70}, the monoadduct will be a superior photosensitiser of singlet oxygen than the bis-adduct. When studying the emission of the pyrene group it is found that the quantum yield is reduced for all functionalized fullerenes compared to the pyrene

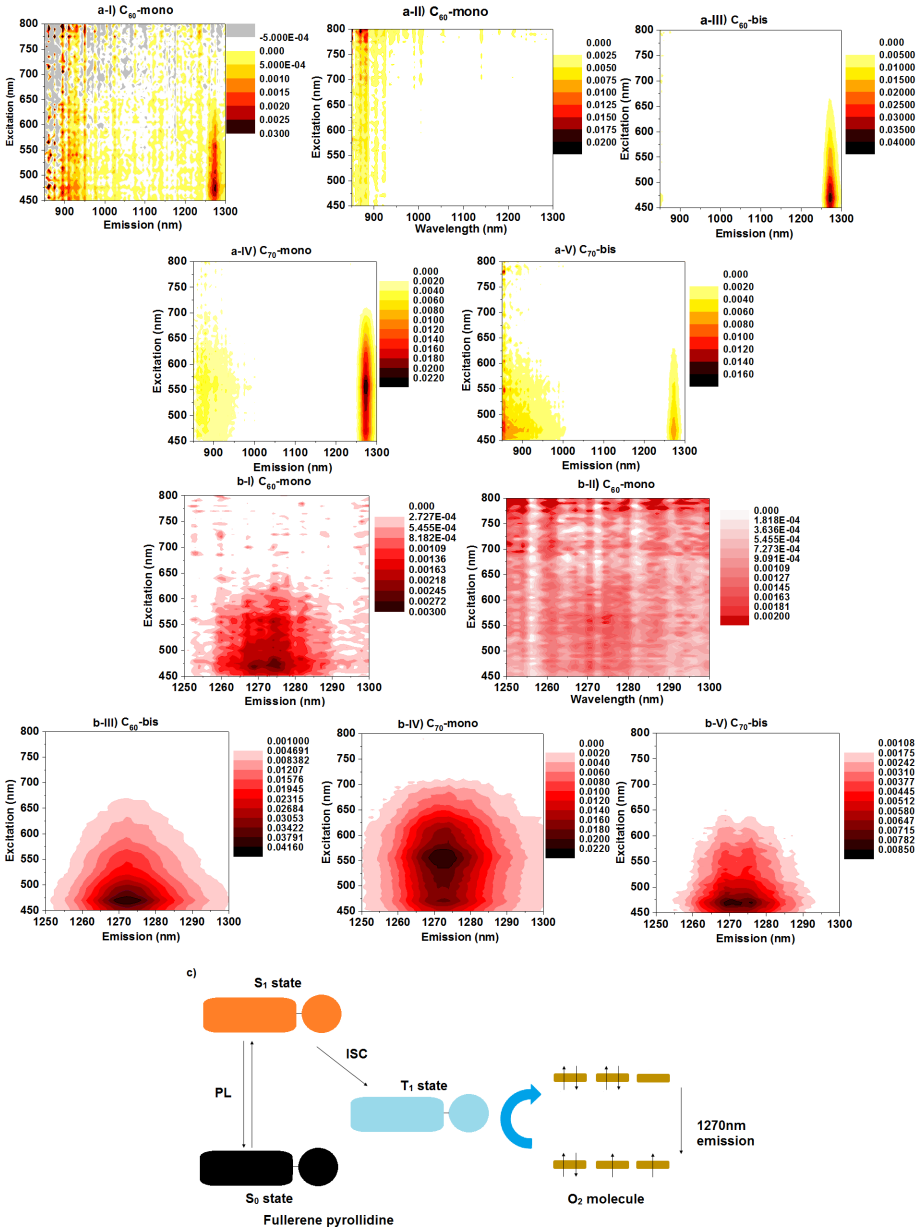

Figure 23: a) Photoluminescence excitation spectroscopy maps for each of the samples. I) and II) show the C_{60} monoadduct in two different concentrations, where the sample I) was twice as concentrated as the sample II). III) Shows the C_{60} bisadduct IV) the C_{70} monoadduct, which is also a good sensitiser for singlet oxygen and V) the C_{70} bisadduct. b) a magnification focusing on the 1250-1300 cm^{-1} region, where the singlet oxygen emission takes place. The contour map colour of figures b) corresponds to different relative heights and so uses a different colour palette. Figure b) I) and III) and V) all show that an excitation of 460 nm is required to cause an emission at 1270 nm, compared to b) IV) which shows an excitation at 560 nm is required. b) II) shows that there is no meaningful emission in this region, confirming the data in a) II). c) The transitions through the fullerene pyrollidine and to the O_2 molecule which results in both the NIR and singlet oxygen emissions.

precursor molecule. When moving from the C_{60} monoadduct to the bisadduct I observe that the emission spectrum goes from two peaks to just one, which is attributed to the presence of the extremely stable charge-transfer excimer in the bisadduct, suppressing the emission of the intra-level transition in the bisadduct. This change is attributed to a reduction in the symmetry of the fullerene centre on addition of a second pyrene group. When moving to the emission of the fullerene a similar trend is observed, with the bisadduct showing the greatest quenching of the fullerene emission due to the creation of a charge separated excimer.

However, when looking between the monoadducts of the two fullerenes, C_{60} and C_{70}, the former shows an enhancement of the fullerene emission while the fullerene emission is quenched for the latter, demonstrating a major difference between the two fullerenes. This difference between the fullerenes is further probed by studying time-resolved PL, which shows mono-exponential decay profiles for the C_{60} monoadduct and C_{70} bisadduct, which corresponds to the S_1 - S_0 emission of the complex. In contrast, the C_{70} monoadduct and C_{60} bisadduct show bi-exponential decay profiles, which I ascribe to a stable charge-separated state in the molecule, which is in agreement with my previous information on C_{60}. This is possible as the lifetime of the additional decay pathway is considerably longer than the S_1 - S_0 transition, which is consistent with a triplet to singlet transition. Upon the addition of a second pyrene unit significant differences were observed in the fluorescence lifetimes associated with both the pyrene and the fullerene. These

differences between the fullerenes is attributed to the influence of the fullerene cage on both the intramolecular electron transfer and the formation of locally excited and charge separation states, where different fullerene cages require different numbers of functional groups to achieve the same effect.

The competition between locally excited and charge separated states was further confirmed by mapping the NIR photoluminescence to observe the photosensitising of singlet oxygen. These measurements displayed the same trends, with the C_{60} monoadduct and C_{70} bisadduct both displaying a quenching of the singlet oxygen signal, while the C_{60} bisadduct and C_{70} monoadduct both acted as strong photosensitisers for the singlet oxygen radical. This provides further evidence for my assignment of the two decay pathways as the charge separated triplet state of the fullerene molecule is what interacts with oxygen to produce the singlet oxygen radical, in agreement with my prior postulation on C_{70}. If this triplet state is not stable, as demonstrated by the absence of a triplet to singlet emission lifetime in the C_{60} monoadduct and C_{70} bisadduct, then it cannot interact with oxygen to generate toxic singlet oxygen radicals.

4 Radio-Frequency Electronics

Having produced molecules which are capable of entering a graphene nanogap for single molecule measurements it is then necessary to develop methods of measuring those single molecules. There are multiple tight constraints on a measurement system which it is necessary to achieve in order to make single molecule electronics possible. The method which was pursued in order to achieve these measurements was radio-frequency electronics.

4.1 Radio-frequency reflectometry

In order to measure the electronic properties of single molecules there are several key requirements. First, the measurement needs to be sensitive enough to detect the transfer of single electrons on and off the molecule. Second, the measurement needs to be fast so that it is possible to detect the presence of the single electrons well within the length of time that the electron occupies the molecule. If the presence or absence of an electron on the molecule can be associated with a change in electrical impedance, then the technique of radio-frequency (RF) reflectometry can be used. Not only can this technique be sufficiently fast and sensitive but, for measurements on quantum states, it is also non-invasive [71]. RF reflectometry is based on the tank circuit. In such a circuit, energy oscillates between the capacitor and the inductor according to simple harmonic motion which can then be damped by a resistor, introducing a quality factor to broaden the res-

onance. Such a resonance is then extremely sensitive to changes in resistance, inductance or capacitance. However, to achieve the highest possible sensitivity in these measurements, it is necessary to have the device being measured and the external circuit impedance matched [72, 73]. This is not trivial, single molecules typically display a large resistance, of the order of MΩ [74], compared to the normal line resistance of 50 Ω and is further complicated by the highly variable nature of parasitic capacitances.

Dr. E. A. Laird designed a measurement circuit with multiple tunable capacitors such that is possible to impedance match an arbitrary device and measurement circuit with the line resistance, regardless of parasitics [75, 76]. It is also possible to change the values of the capacitors once the device has been mounted and cooled, meaning that impedance matching can be achieved under the exact measurement conditions. This is demonstrated in Figure 24, where the effect of tuning each varactor on the simulated reflection coefficient, Γ, can be seen with typical device parameters [77]. This technique has been demonstrated to achieve perfect impedance matching, allowing for a sensitivity of 1.6 $\frac{\text{aF}}{\sqrt{\text{Hz}}}$ with a bandwidth of 18 MHz to be achieved in a quantum dot device [77].

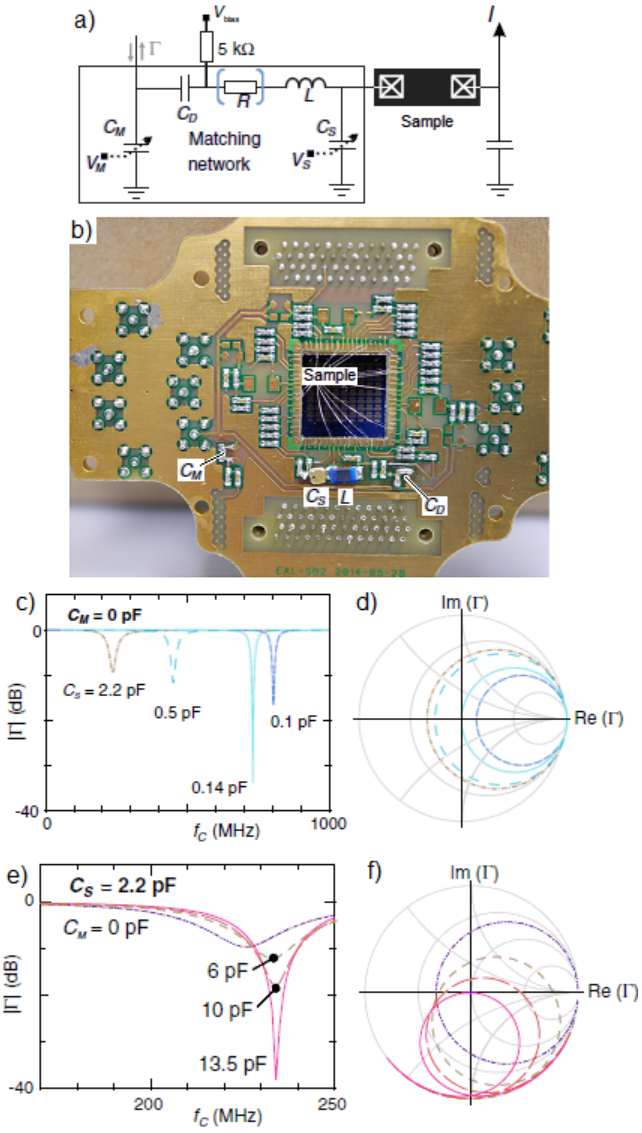

Figure 24: a) A sample is connected to the impedance matching network which is made up of an inductor L = 223 nH, variable capacitors C_S and C_M and a fixed capacitor C_D = 87 pF. The various parasitics in the circuit are characterised with a single resistance, R = 20 Ω and the device resistance is assumed to 1 GΩ. Also shown is the actual sample board b) with the components from a) and the sample position. Γ is shown as a function of frequency in c) and as a Smith chart [78] in d) for a circuit with no matching capacitor. Perfect matching occurs when Γ crosses the origin of the Smith chart ie. $|\Gamma| = 0$. For this set-up perfect matching can only be achieved when C_S = 0.14 pF, which is less than the typical parasitic values of the circuit which are included in C_S. If C_M is increased perfect matching can be achieved for realistically large values of C_S, as is shown in e) and f). For C_M = 13.5 pF, C_S can be as large as 2.2 pF and still obtain perfect matching which is well within the range of values for typical parasitics.

4.2 Radio-frequency demodulation

In RF reflectometry a signal is sent to the tank circuit and it is the reflected signal which is studied. However, to extract useful information from the reflected wave it must be processed by demodulation. The demodulation circuit to be discussed is configured as in Figure 25, with each part of the circuit performing a distinct role. The area in the green box amplifies the reflected signal and filters some unwanted noise from it. The area in the blue box tunes the phase shift between the reflected wave and the carrier wave to maximise the output signal or to study the phase shift of the reflected wave. The area in the red box contains a mixer and a low-frequency low-pass filter. The carrier and reflected wave are input to the mixer which produces the sum and beat-frequencies at twice the carrier-frequency and direct current (DC) respectively. The filter then removes all signals which are not comparable in frequency to DC, and the filtered signal is measured to find the amplitude or relative phase of the reflected wave. Carrier waves are generated at the frequencies where the sample and tank circuit, see Figure 26 a, cause a large absorption. The properties of the resonance are monitored by looking at the beat-frequency of the carrier wave and the reflected wave.

I built and tested this circuit using a sample board containing several varactors as well as two inductors, see Figure 26 a. The shunt and series varactors, C3, C4 and C5, were tuned to maximise the reflected signal observed with a RIGOL DSA815 spectrum analyser. During this optimisation, the sample varactors C1

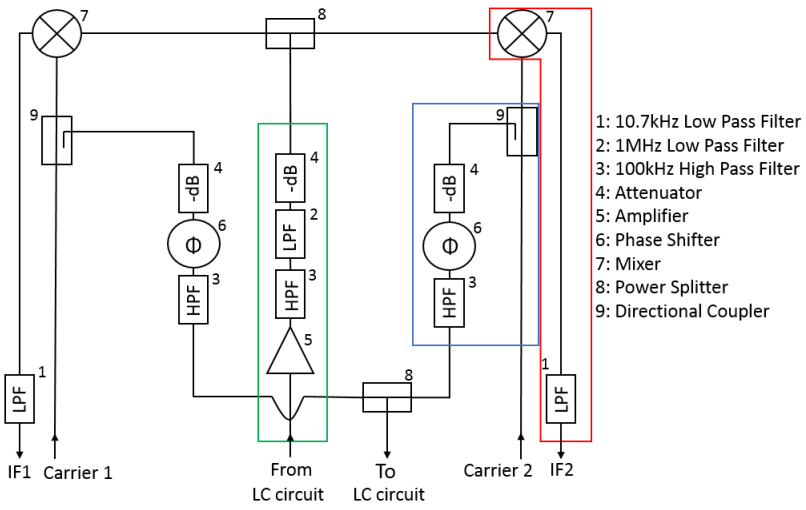

Figure 25: Schematic diagram of the demodulation circuit with a list of parts and particular sections marked with coloured boxes to describe their function.

and C2 were fixed at 4 V of applied bias, which corresponds to a capacitance of 355.8 fF. The observed reflected signal is seen in Figure 26 b as well as the reflection from a 50 Ω terminator. As can be seen the resonances are very clear, sharp and well separated.

I then tested the sensitivity of this resonance in a variety of ways. The first test was to observe the change to the resonance on changing the voltage applied to the varactors C1 and C2, see Figures 26 c and d. This was to mimic a small change in capacitance, such as the change associated with a singlet-triplet transition in a molecule. It is clear that the circuits are sensitive to changes in capacitance of the order 1 fF and, as the change in capacitance associated with a singlet-triplet transition can be as large as 10 fF, it is very likely that the system will be able to measure these changes.

Having shown that it is possible to tune the position of the resonances using

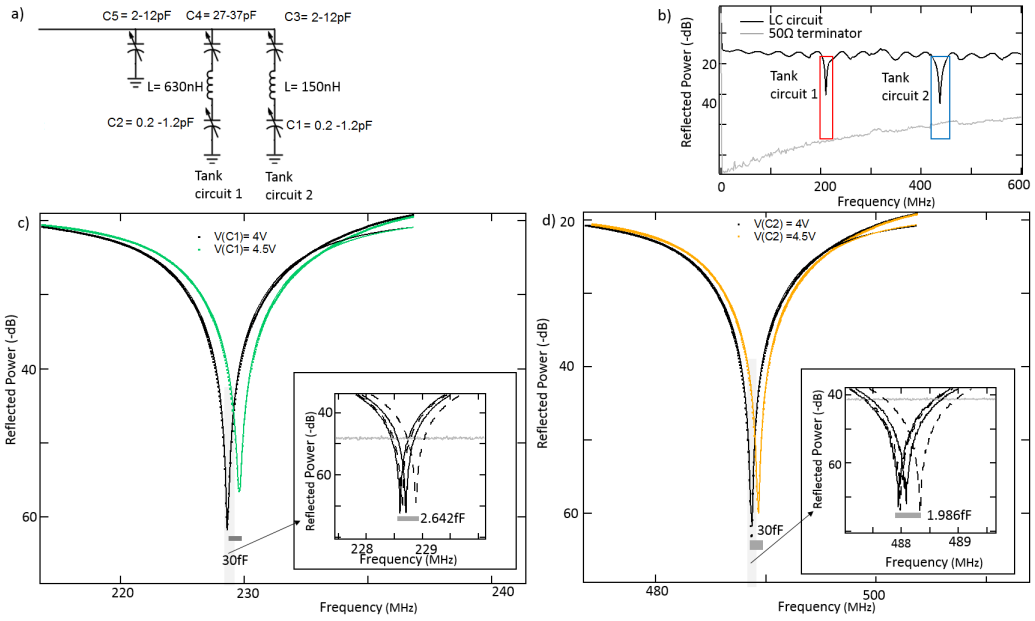

Figure 26: a) The sample board which was used to test the sensitivity of the capacitance sensing measurements. The varactor C5 is called the matching varactor as it moves all of the reflected signals, the varactors labelled C3 and C4 are called the decoupling varactors and the varactors C1 and C2 are the sample varactors. b) The reflected signal of the resonant circuit, black, compared to the reflected signal from a 50 Ω terminator, grey. The two LC resonances are clearly seen and have been labelled according to which part of the circuit in figure a) they correspond to. c) The area in red from figure b) has been expanded for two voltages applied to C1, shown with dots in black and green. The lines have also been fitted to a lorentzian profile (solid lines) to find the Q-factor of the resonance to be 42. The inset shows a further zoom on the area shaded grey with increasing applied voltages from 4 V. d) The area in blue from figure b) has been expanded for two voltages applied to C2, shown with dots in black and orange. The lines have also been fitted to a lorentzian profile (solid lines) to find the Q-factor of the resonance to be 49. The inset shows a further zoom on the area shaded grey with increasing applied voltages from 4 V. As can be seen in c) and d) the resonances are of a higher quality than indicated in b). The reflected power drops well below that measured for a 50 Ω terminator, which should display perfect reflection. It is assumed that this is because of imperfections in the 50 Ω terminator and the spectrum analyser. This indicates that the tank circuits are exceptionally well impedance matched to the rest of the circuit due to tuning the varactors.

the varactors, the resonant circuit was connected to the demodulation box and the output was displayed on a RIGOL DS1204B digital oscilloscope. An amplitude modulation was then applied to each input signal, creating a sine wave and a square wave as seen in Figures 27 c, d and e, which demonstrates that there is little cross-talk between the two halves of the demodulation box. This experiment also showed that the demodulation box is capable of responding to changes in capacitance of the order 1 fF at a frequency of the order 10 kHz. This shows the validity of using varactors to tune the resonance as well as the ability of RF demodulation to perform fast and sensitive measurements of the kind that will be necessary for detecting single electron charges in devices.

In order to make sensitive measurements on real devices low electron temperatures are necessary. This is so that the thermal broadening of electron states is smaller than the energy separation between the levels, and is achieved by a process known as thermalization. This involves maximising the thermal conductivity to the mixing chamber of the refrigerator, while minimising the thermal conductivity to room temperature. This is problematic as electrical measurements of the device will be taken, necessitating wires to room temperature. It is also essential to have an electrically insulating connection to the grounded mixing chamber plate. This requires the use of an electrical insulator, which are poor thermal conductors, to prevent a short circuit to ground within the fridge. To mitigate the issue of hot wires their electrons are cooled by a series of heat sinks to cold plates. For

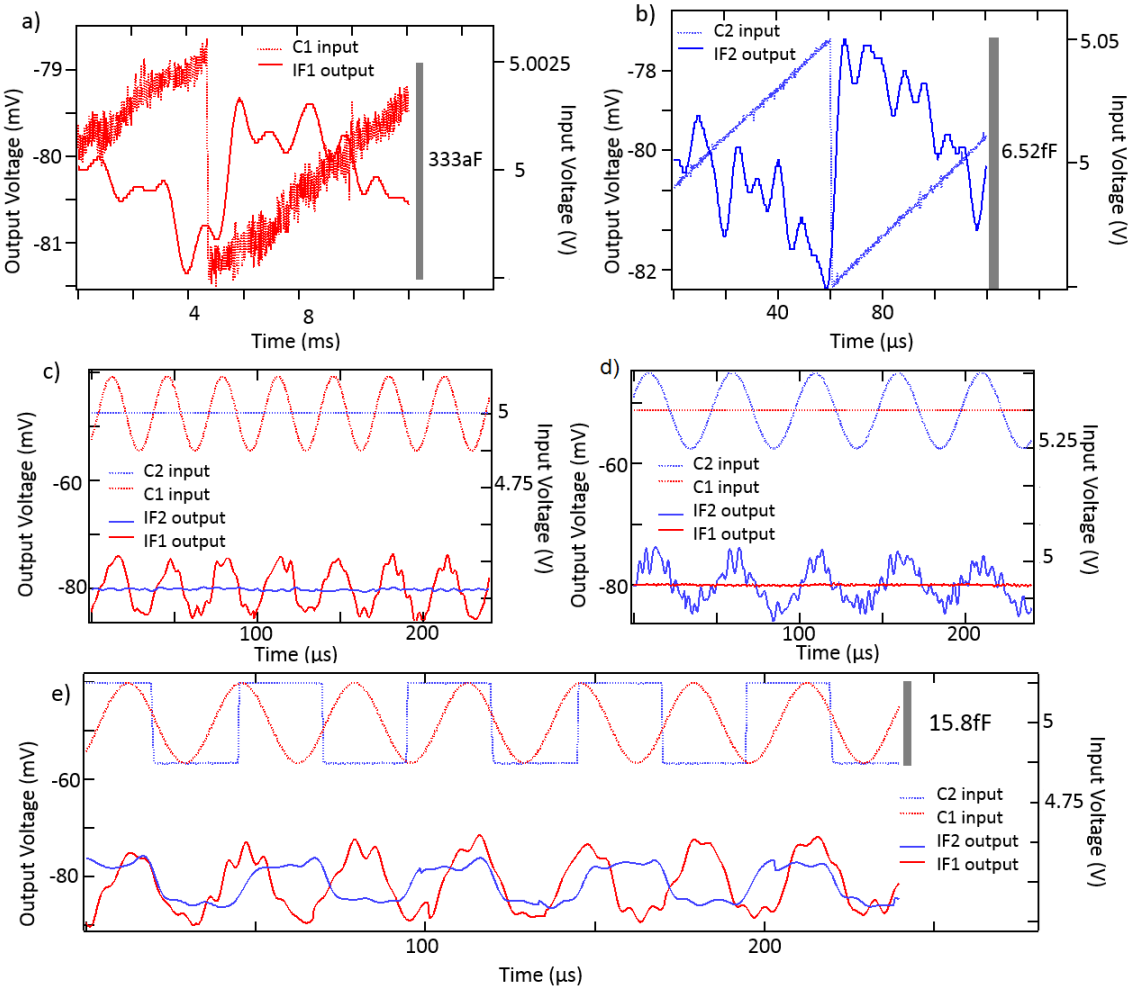

Figure 27: a) and b) show the effect of an asymmetric ramp function being applied to C1 and C2. As can be seen, the output measured on the IF lines of the demodulation box mirrors the applied function and can be sensitive down to the order 100 aF for ms measurement times. c) A 30 kHz sine wave of amplitude 500 mVrms and offset 5 V is applied to varactor C1 while a constant voltage of 5 V is applied to C2. As can be seen a near constant signal is measured in the output of IF2 while the sine wave is reproduced reliably in IF1. d) A 50 kHz sine wave of amplitude 500 mVrms and off-set 5 V is applied to varactor C2 while a constant 5 V signal is applied to varactor C1. The sine wave is reproduced again in the output of IF2 and a constant signal is measured for IF1. e) A 50 kHz sine wave of amplitude 500 mVrms and offset 5 V is applied to varactor C1 while a 20 kHz square wave signal of amplitude 500 mVrms and offset 5 V is applied to C2. The sine and square wave signals are reproduced once again in the measured output with little cross-talk observed.

these to be effective there must be good thermal conductivity between the wires and the plates. However, most thermal conductors are also electrical conductors, which would short-circuit the electronics. The best choice of material therefore is a crystalline insulator such as sapphire, see Figure 28. Such materials are electrical insulators due to their lack of free electrons, but relatively good thermal conductors due to their lack of disorder, allowing for long phonon mean free paths [79]. It is necessary that electrons take a long path across this cold sapphire so that much of their energy can be lost to the sapphire. This is characterised by a resistance of $1\,\mathrm{k}\Omega$ which is achieved by defining meanders of metal on the sapphire. Gold is chosen as the main metal as it is chemically inert and has a high electrical conduction. However, gold has a very poor adhesion to most surfaces, so a thin sticking layer of chrome or titanium must be used. Due to an improved performance seen in prior work with a chrome sticking layer it was decided that chrome would be used [79].

The processes followed to create the heat sinks are described here. First the samples are cleaned by sonicating them in piranha etch (a 3:1 mixture of concentrated H_2SO_4 and H_2O_2) for twenty minutes, then acetone for ten minutes, before spraying with isopropanol and drying with nitrogen. A thermal evaporator is used to deposit 30 nm of chrome followed by 300 nm of gold. The samples are then spin coated with Shipley Microposit S1813 resist at 170 rpm for 15 seconds, before ramping to 4000 rpm for 60 seconds, and the resist is then baked

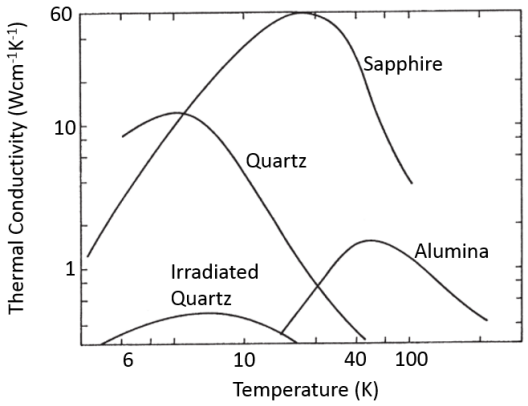

Figure 28: The thermal conductivity of several crystalline insulators as a function of temperature. As can been seen, sapphire has a relatively high thermal conductivity even at very low temperatures. Not shown are electrical conductors, which typically have values of thermal conductivity of the same order magnitude (eg. at 10 K $\kappa_{Cu} \approx 10\ \mathrm{WCm^{-1}K^{-1}}$), or amorphous insulators, which typically have thermal conductivity several orders of magnitude smaller (eg. at 10 K $\kappa_{glass} \approx 10^{-3}\ \mathrm{WCm^{-1}K^{-1}}$) [80].

for 90 second at 95°C. After baking, the resist is exposed to UV radiation of an intensity 7 mW/cm^2 for 10 seconds with the mask seen in Figure 29 a to define the meander lines. The resist is baked in the same conditions a second time before being developed in MF-319 for 90 seconds. Oxygen plasma is used to further etch the resist for 10 seconds before the metals are etched in their respective standard etching solutions for approximately 60 seconds each. This produced a heat sink similar to that seen in Figure 29 b. These heat sinks were then tested for use at cryogenic temperatures measuring their electrical resistance before and after being dipped into liquid nitrogen. When this was done, twelve of the thirteen line resistances remained identical on returning to room temperature. However, the resistance of one line changed from 1.3 kΩ to 4.1 kΩ, see Figure 29 c.

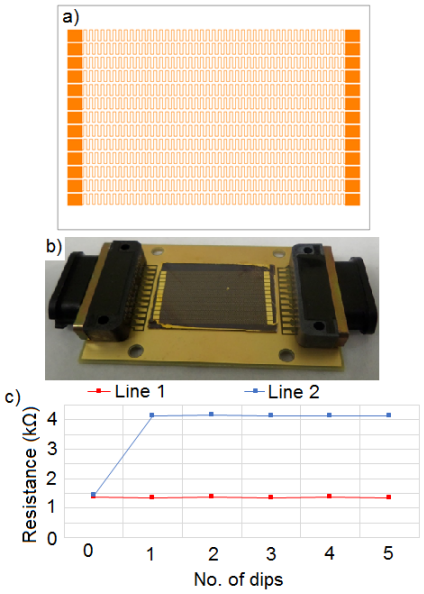

Figure 29: a) An image of the pattern used to create the gold meanders on the sapphire heat sinks. b) A photo of one of the finished sapphire heat sinks put on the circuit board that it will be fixed to when placed in the dilution refrigerator. c) The change in resistance of two lines on a sapphire heat sink after sequentially cooling to 77 K with liquid nitrogen. Line 1 is typical of the other 11 lines. However, line 2 shows a worrying rise in resistance.

4.3 Measurements on a quantum dot

The circuits that I built and tested were then used by other members of the group to measure semiconductor quantum dots which further demonstrate that the circuits would be able to measure single molecule devices [77]. The device presented here is a GaAs/AlGaAs quantum dot patterned with Ti/Au gate [82], see Figure 30 a. The device was mounted on a printed circuit board, along with the necessary impedance matching electronics, and was inserted into a dilution refrigerator. At the temperatures found in the fridge, $T_{MC} < 1$ K, thermal broadening of the electronic states in the quantum dot will be small enough that single electron behaviour can be observed, for example by being able to create a Zeeman splitting between electron spin states greater than the thermal broadening. The quality of the impedance matching was determined by comparing the powers input to and output from the demodulation box to the sample circuit S_{21}, which is at ports 1 and 2 in Figure 30 a and is proportional to Γ, the complex impedance coefficient. Figure 30 b shows the effect of tuning the voltage V_S, which controls varactor C_S, while keeping C_M constant at approximately 14 pF. As V_S increases so too does the resonance frequency, confirming the change in C_S. The impedance matching depends heavily on C_S, with an optimum seen for $C_S = 2.78$ pF. Using the information obtained it is also possible to plot Γ on a Smith chart, see Figure 30 c, and see that as V_S is tuned, Γ crosses the origin, confirming that we do indeed observe perfect matching at a frequency $f_c \sim 211$ MHz.

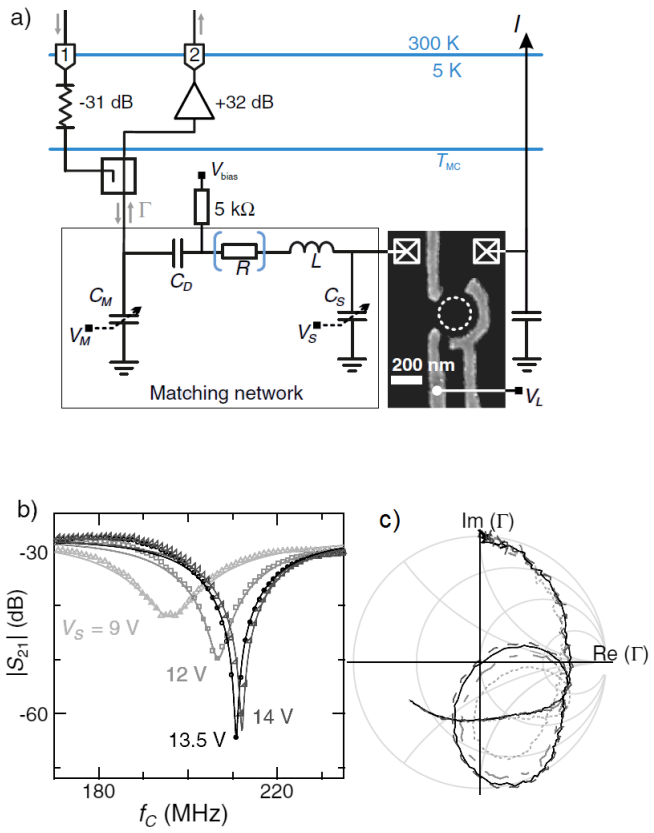

Figure 30: a) Experimental set-up showing an SEM image of the quantum dot, with the ohmic contacts symbolised with boxes. This is connected to the impedance matching network and tested by inputting an RF signal from the demodulation box, see Figure 25, to port 1. The reflected signal is then amplified and output to the demodulation box again at port 2. b) Reflectometry measurements as a function of frequency for different values of V_S, with constant V_M, showing the magnitude of S_{21}. The data points, symbols, are fitted to a circuit model, curves. c) The data from b) has been converted to a reflection coefficient and plotted as a Smith chart, perfect matching is observed at $V_S = 13.5$ V.

The reason that so much effort is made to tune the reflection to perfect matching is that it gives the most sensitive response to changes in capacitance. This sensitivity was characterised by applying a sinusoidal modulation to V_S with root mean squared (rms) amplitude $V_m = 2$ mV_{rms}, creating a change in capacitance δC, and frequency $f_m = 1.75$ kHz. It was chosen to apply a modulation to the varactor rather than the quantum dot so that the measured response would only

be due to changes in capacitance, rather than a combination of both capacitance and resistance. This modulation gives rise to two side-bands, with frequency $f_c \pm f_m$, by measuring the height of these side-bands it is possible to determine the sensitivity according to equation (14).

$$S_c = \frac{\delta C}{\sqrt{2\triangle f}} 10^{\frac{-SNR}{20}} \tag{11}$$

In this equation SNR is the signal to noise ratio of the side-bands in decibels and $\triangle f$ is the resolution bandwidth [83]. As expected the maximum sensitivity, $S_c = 1.6\ \frac{\text{aF}}{\sqrt{\text{Hz}}}$, is obtained at the resonance with V_S= 13.5 and $f_c = 210.75$ MHz.

The demodulated signal in Figure 31 is sensitive to changes in the capacitance as well as the conductance of the device being measured. In order to measure only the capacitance of the device, it is necessary to measure the demodulated signal while varying the phase shift applied by the demodulation circuit, φ. By doing this both at and far from a Coulomb peak it is, in theory, possible to measure the phase shift of the quantum capacitance, as φ is directly proportional to the phase of Γ. However, due to non-linearities in the demodulation circuit, changes in the conductance of the quantum dot can also affect the phase. Therefore, it is only by measuring and using the DC conductance of the quantum dot that the capacitance can be extracted.

From Figure 31 b it can be seen that quantum dot conductance and capacit-

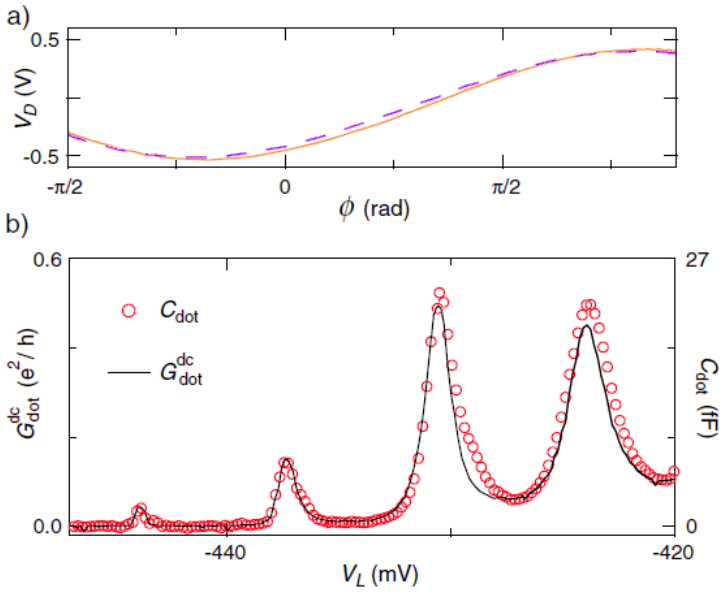

Figure 31: a) Demodulated output of the circuit as a function of the phase shift, φ, for a V_L both on and off resonance shown with a pink dashed line and an orange solid line respectively. This position relative to the resonance affects both the amplitude and the phase of the demodulated output which suggests both a dissipative and dispersive element affecting V_D. b) The imaginary component of the impedance measured as a function of V_L for a series of Coulomb peaks with DC conductance and extracted capacitance shown as a solid line and red circles.

ance are proportional. However, this is not true in the general case and is only possible in the asymmetric limit, $\Gamma_R \ll \Gamma_L$. In this limit Γ_{R} is approximately constant with $\mathrm{V_L}$, and both the capacitance and resistance of the dot are expected to vary with $\mathrm{V_L}$ in the same way as the density of states of the quantum dot [84, 85]. This contrasts with measurements that have been made on devices with more opaque tunnel barriers [86, 87].

4.4 Conclusion

These measurements of quantum dot impedance are very promising for being able to detect singlet-triplet transitions in quantum dots or measuring single-electron events in individual molecules. Using such a measurement technique simplifies the requirements of the design of measurement systems, as a charge sensor is no longer necessary to detect the electrons. By estimating the change in quantum capacitance between two different qubit states to be approximately 10 fF [88], the observed sensitivity of $S_c = 1.6\ \frac{aF}{\sqrt{Hz}}$ should be able to perform single-shot measurements in a time of approximately 13 ns. However, this fails to take into account the fact that the quantum capacitance is greatest for a very narrow bias range close to zero detuning. The single-shot readout time is more accurately determined by considering the value $\mathrm{S_C V_0}$, which takes into account the perturbation caused by the measurement on the delicate states being investigated. By considering $\mathrm{S_C V_0}$ the estimated single-shot measurement time is instead approximated

to be 64 μs [77]. Unfortunately, this is approximately twice the singlet-triplet lifetime in GaAs, necessitating further improvements to achieve singlet-shot readout in these devices. One such improvement would be to optimise the geometric capacitance in the circuit by using superconducting inductors, thus improving the quality factor [89] or using a superconducting amplifier with drastically reduced noise temperature [90].

5 Single-molecule devices

Chapter 4 demonstrated that the circuits which I have built are capable of making the sensitive measurements necessary to explore the complex electronic structure of quantum dot devices. Therefore, it should also be possible to explore single molecule devices. In this chapter the molecules that I have created will be combined with the circuit that I have built and tested to explore the electronic properties of these molecules.

5.1 Introduction

The primary motivation behind my creation of bis-pyrene functionalized fullerene molecules in this D. Phil project was that they should be able to self-assemble into a graphene nanogap, using π-π stacking interactions, and thus allow for measurements to be made by my colleagues on the electrical properties of single fullerene molecules [24]. Fullerenes are a wide class of materials and it is hoped that by exploring the full range of these materials many and varied unique electrical properties will be observed, many of which, such as their thermoelectrical properties, may find practical applications.

5.2 Transport spectroscopy

Once the graphene nanogaps have been created it is possible for the molecules that have been produced to be put into the gaps so that transport measurements

can be performed on those molecules, the presence of graphene either side of the gap contacted by metal electrode will allow a bias voltage to be applied and the 300nm thick SiO_2 layer will act as a back-gate to influence the chemical potential of the molecules. Molecular devices are produced by immersing successful nanogap devices in a 10 μM solution of C_{60} bisadducts in chloroform for 30 min before drying them with N_2 gas. Steric considerations of the different regioisomers of pyrene C_{60} bisadducts means that only the cis-2 or cis-3 regioisomer would be able to bridge the gap. DFT calculations of the relaxed molecule in the nanogap indicate that the cis-3 isomer is the most stable isomer for bridging the gap [24], in addition to being the most abundant of the cis isomers produced from the functionalization of C_{60}, see Chapter 2. The strong favourability for the self-assembly of the isomer cis-3 into the graphene nanogap can be understood by considering the frontier orbitals of the gas-phase molecule, see Figure 32 b. It can be seen that the LUMO is isolated almost entirely on the fullerene core of the molecule, whereas the HOMO is distributed in the pyrene group as well. This electron density in the π conjugated pyrene group means that the molecule is able to form attractive intermolecular π-π stacking interactions with the graphene nanoribbon either side of the gap. The current stability diagram of a single fullerene molecule as a transistor was measured in Figure 32 c as a function of bias V_b and gate V_g voltages at a temperature of 20 mK. The height of the Coulomb diamonds allows for the addition energy between redox states to be determined

asE_{add} ∼160 meV. Assuming the constant interaction model, The addition energy is defined by:

$$E_{add} = E_C + \triangle_{HL}$$

where E_C is the charging energy due to Coulomb interactions of the electrons in the molecule, and $\triangle_{HL}$ is the energy gap between the HOMO and LUMO levels [92]. For a two-fold degenerate system, E_{add} would fluctuate between E_C and E_C + $\triangle_{HL}$ for adjacent levels, while for systems with greater degeneracies, E_{add} is equal to E_C until an orbital is filled. This fact provides evidence that the charge transport observed here is dominated by the HOMO level. This is because DFT calculations suggest that the HOMO and HOMO-1 levels are close to degenerate in energy, -4.59 and -4.60 eV respectively, while the LUMO and LUMO+1 levels have a significant energy separation, -3.12 and -2.86 eV respectively [24]. Therefore 4 electron states exist with similar energy levels for HOMO dominated transport. The other evidence for HOMO transport is that DFT calculations show that the Fermi level of the graphene ribbon will be much closer to that of the HOMO than the LUMO levels on the fullerene.

By focusing on the transition from the N+1 to the N+2 state, labelled P3 in Figure 32 c, as a differential conductance, G, map it is possible to see a number of additional features from excited state transitions. Between Figures 32 b and

c the gate potential for the charge transition changes, this is due a common hysteretic effect likely related to charge traps in the oxide. Those excited states with an energy greater than 33 meV, labelled in white on Figure 32 d, are close in energy to the intrinsic vibrational modes of the pristine C_{60} molecule. Additional excited states can be observed with an energy below 33 meV, labelled in green on Figure 32 d, which instead show good agreement to DFT modelling of the pyrene bisadduct, with the mass of the pyrene tending to infinity to represent the molecule being bound to the graphene nanoribbons. The low energy vibrational modes are therefore only centre of mass oscillations, both translations and rotations, of the fullerene core as movements of the pyrene group are too energetic, see Table 9.

High resolution transport spectra show that there is an extremely low energy vibrational level, with energy of approximately 1.7 meV. By once more studying DFT models it is possible to assign these levels to a vibration breathing mode in the molecule, where the pyrene groups move towards the fullerene core while the fullerene is pushed out of the plane of their motion, the molecule then returns to its equilibrium position before the pyrene groups pull away from the fullerene core, dragging the fullerene towards the plane of the pyrene groups. This is fitting with previous studies that have demonstrated the binding between pyrene and graphene to be significantly stronger perpendicular to the plane of the graphene than parallel to the plane, allowing the pyrene groups to slide over the graphene sheets far more easily than they can move away from the graphene sheet [94].

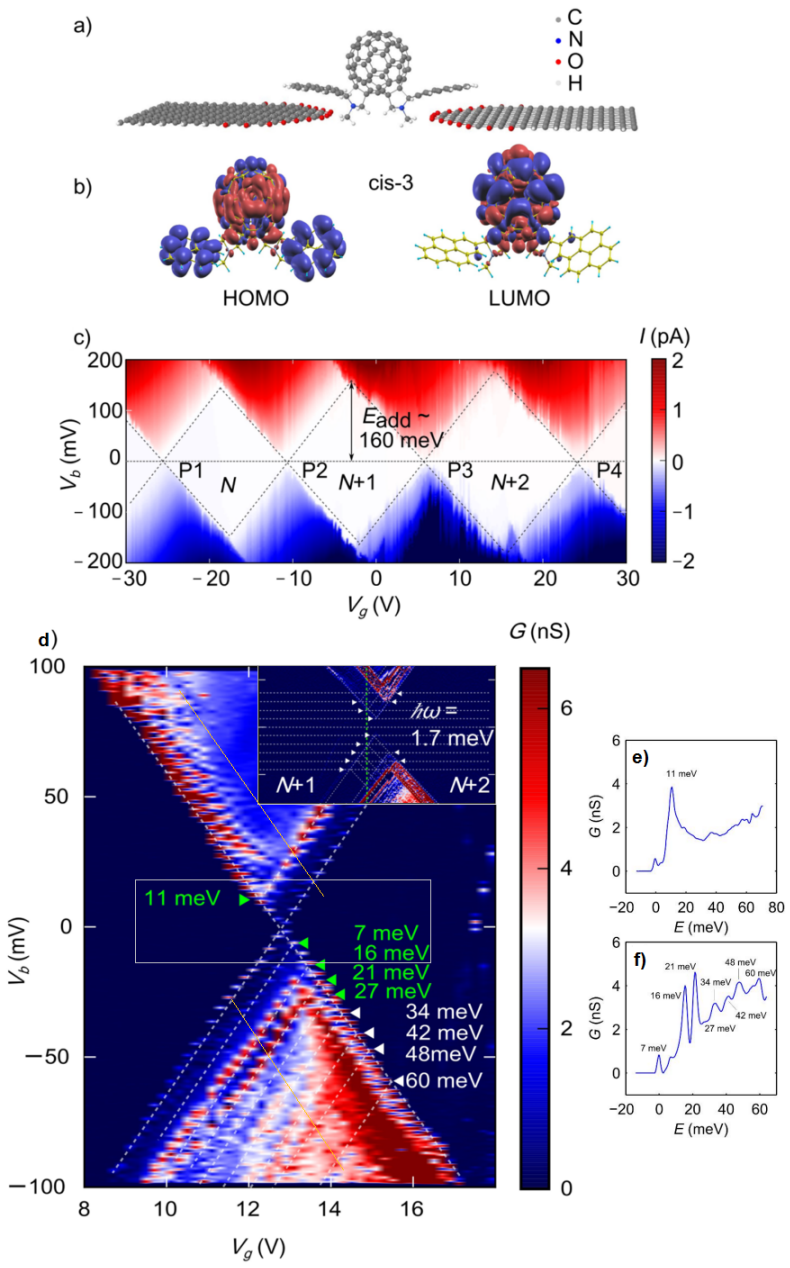

Figure 32: a) DFT calculations of the relaxed structure of the cis-3 isomer bridging a graphene nanogap. The molecules are deposited on the electrodes from a chloroform solution. b) DFT simulations of the HOMO and LUMO iso-surfaces in the cis-3 isomer. c) Current stability diagram of a device. All measurements are performed at 20 mK under high vacuum unless otherwise stated. The redox state of the molecule changes by one between adjacent diamonds. d) Conductance stability diagram of the N+1 to N+2 transition (P3), obtained by taking the numerical derivative of the current measured. Excited states are highlighted with white and green arrows. Inset, a high resolution conductance plot of the region in grey in which spaced vibrational state lines are observed in the low bias regime. e) And f) show the conductance along the yellow lines in d), which more clearly show the excited states.

NB. The low bias current is suppressed due to Franck-Condon blockade, see Chapter 5.3.

Mode	Transport / eV [24]	Raman / eV [24]	DFT / eV [24]	DFT/ eV (pristine fullerene) [93]
CM T_y	7		8	
CM T_x			10	
CM R_z	11	13	12	
CM T_z	16	16	16	
CM R_x	21	19	19	
CM R_y	27	25	21	
$H_g(1)$	34	33	32, 33, 34	33
$T_{2u}(2)$	42			43
$G_u(1)$	42			43
$H_g(2)$	48	55		53
$A_g(1)$	60	61		61

Table 9: Comparison between the measured excitation energies from transport and Raman spectroscopy, calculated values and the intrinsic vibrational modes of pristine C_{60}.
NB: Transport measurements are performed at 20 mK under vacuum with the molecule bound by the pyrene groups to graphene electrodes. Raman spectroscopy is performed under ambient conditions with the molecules drop-cast on gold coated silicon/glass substrates. DFT calculations are performed with the condition that the pyrene mass approaches infinity to simulate the groups being bound to a graphene surface. The values for the vibrational modes of pristine C_{60} are found here [93]. It is found that the deviations between our measurement methods fall within the range of values reported in prior work, where values are obtained from both experiments and ab initio theories, and reports a variation of up to 10 meV [94].

Both the characteristic vibrations of the C60 molecule and the low-bias current suppression, see below, can be observed when focusing on other transition peak within this device and, with reduced clarity, in other devices, see A 13.

5.3 Franck-Condon blockade

It can be seen from the transport spectroscopy in the inset of Figure 32 d that the Coulomb diamonds do not meet at zero applied bias, as would be expected. This is unaffected by the application of a magnetic field, proving that this is not a magnetic effect. As the spacing between the Coulomb diamonds is equal to an integer number of vibrational excitations this feature is attributed to Franck-Condon (FC) blockade. This effect occurs in systems which display strong electron-vibron couplings [95], where electrons tunnelling onto the molecule perturb the equilibrium position of the wave function for the harmonic oscillation of the molecule for the relevant charge states. This amount of perturbation is always proportional to the electron-vibron coupling constant, λ, where $\lambda \gg 1$ is the strong coupling regime, causing a large displacement of the equilibrium position of the N+1 charge state compared to the N charge state. This causes the overlap of the vibronic ground state wave functions for the N and N+1 states to be very small. Therefore, the transition rate, which decreases exponentially with λ, is also very low, leading to low bias for low current. This FC blockade of the transition is lifted when a large enough bias is applied to cause excitations to higher vibrational states. The wave

function then exhibits a node at the equilibrium position and the range of motion in the oscillation is significantly larger, leading to a greater overlap of wave functions and so an increased transition rate.

By fitting the excitations from the inset of Figure 32 d to the rate equation model it is possible to determine $\lambda = 3.0$ for this transition [96]. With this value and by assuming a tunnel coupling which is asymmetric, $t_L = 0.2t_R$, it is possible to achieve a simulated transport spectrum which is extremely similar to the observed spectra, see Figure 33 a and b. Asymmetric coupling is to be expected as neither the graphene nanoribbon nor the pyrene anchor groups are selective for where they will bind to each other and the DFT calculations show that the pyrene anchor groups are not symmetric around the fullerene core.

Another feature of interest which can be observed is that of avalanche transport, which has been observed previously in systems with strong electron-vibron couplings and weak vibron relaxations [95]. Avalanche transport is typified by large fluctuations in the current due, in this case, to rare events occurring which excite the molecule into an excited vibrational state. From these excited states rapid tunnelling can take place for a period of time between vibrational states with a large wave function overlap, before the molecule once more relaxes to the ground vibrational state and the tunnelling is once more suppressed, see Figure 33 c to h.

Changing the bias voltage leads to three distinct regimes for the tunnelling

through the single molecule junction. For the low bias case where $\beta eVb < 2\hbar\omega$, where $\beta \approx 0.5$ is given by the ratio of the source capacitance and the total capacitance, the transitions $N_0 \leftrightarrow N{+}1_0$ and $N_0 \leftrightarrow N{+}1_1$ experience FC blockade, see Figure 33 c, d. For intermediate bias voltages, $2\hbar\omega \leq \beta eVb < 3\hbar\omega$, the $N_0 \leftrightarrow N{+}1_2$ transition is within the bias window and so avalanche transport is observed, see Figure 33 e, f. While the transition rate is higher, the system typically experiences a long wait time with no current while it remains in the vibron ground state. Finally, for large bias, $\beta eVb \geq 3\hbar\omega$, the transfer of charge can proceed through the process of sequential tunnelling using the, now accessible, $N_0 \leftrightarrow N{+}1_3$ transition, see Figure 33 g, h.

Calculations in prior work suggest that by chemically modifying a molecule it should be possible to tune the electron delocalisation and molecular orbital energies such that the thermopower of single-molecule junctions can be increased significantly [97, 98]. Additionally the thermopower of a junction is greatest when the transport through the junction is dominated by a level with low vibrational heat conductance [98], meaning that the extremely long vibron lifetimes observed here make these molecules promising candidates for thermoelectrical devices in addition to being interesting in their own right.

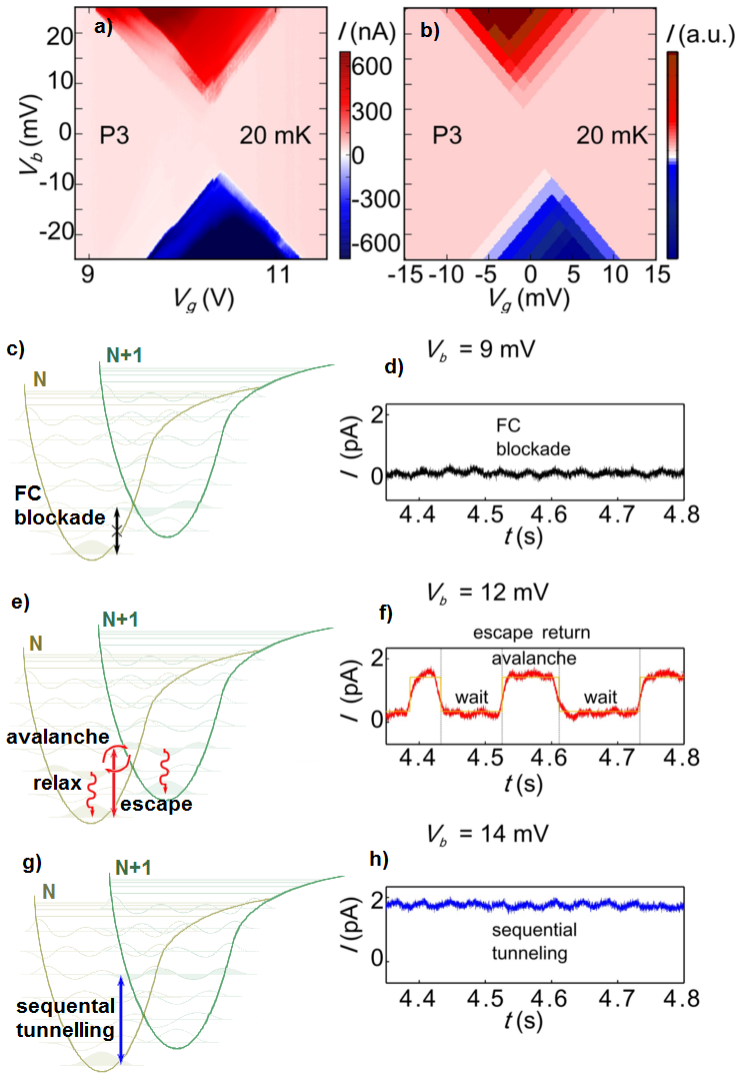

Figure 33: Observed a) and simulated b) current stability diagram of P3 at 20 mK, for b) the coefficient $\lambda = 3$ and $t_L = 0.2t_R$. c), e) and g) Show schematics of the three transport regimes while d), f) and h) show current−time traces at V_b = 9, 12, and 14 mV and Vg = 10.15 V.

5.4 Thermoelectrics

As mentioned above, the ability of a material to generate a potential difference between hot and cold contacts is given by the Seebeck coefficient. Additionally, the dimensionless figure of merit, the thermoelectric efficiency, $ZT = \frac{S^2GT}{\kappa}$, where κ is the thermal conductance due to both phonons and electrons, is of importance in finding the power that could be generated by a thermoelectric device. This is problematic as, in most bulk materials, a high S is associated with a low G, as to build up a large potential difference only a small current may flow. Equally, a high G is associate with a high κ as a material's electrical and thermal conductivity are usually very closely related [99]. However, it has been shown that this is not necessarily true for nanomaterials [100]. Of particular interest is the ability to subtly influence the properties of merit in organic molecules by changing the exact chemical composition of the molecule through a range of techniques [101]. For example, it was shown that by placing two fullerene molecules in close proximity it was possible to increase ZT fourfold [102], while changes made to better align the Fermi levels of the molecule and leads led to an order of magnitude increase in ZT [103]. In spite of these advances, the highest reported Seebeck coefficient for single-molecule systems is still only S = 50 μVK^{-1} [104]. A device was created by Dr. P. Gehring with a geometry as shown in Figure 34 a, contianing a gold micro-heater 1 μm from the device, allowing them to create a temperature gradient across the device [105]. This temperature gradient can be determined by a variety

of methods [106]. By analysing the resistance of the gold contacts near and far from the heater it was possible to find the temperature difference as a function of heater power, P_h, to be $\frac{\triangle T}{P_h} = 43$ KW^{-1} and so a temperature gradient of $\frac{\nabla T}{P_h} = 14$ Kμm^{-1}W^{-1} [106].

The thermoelectric response of the empty graphene nanogap was measured first so that comparisons could be made to the single molecule device. When the heater is turned on the Fermi-Dirac distribution of the contact closer to the heater experiences a greater degree of thermal broadening than the contact further from the heater, opening up a bias window between the contacts through which a current of electrons can flow. This, combined with scanning thermal microscopy measurements of the temperature difference between contacts, allowed for the Seebeck coefficient to be measured as S = 60 μVK^{-1}, which is comparable to other such systems [106].

It was then possible to explore the thermoelectric properties of C_{60}, which have been studied previously in both STM break-junctions [103] and electromigrated gold junctions [107]. Empty gaps were found at 77 K, as in Figure 30 c and were then warmed and immersed in a choloroform solution of bis-pyrene functionalized C_{60} molecules for 60 seconds, where the molecules self-assemble into the graphene nanogap, before being dried with N_2 gas. When cooled to 77 K again, the devices display conductance peaks. Of particular note is the peak at $V_g \approx 25$ V, where the Seebeck coefficient is measured to be a maximum of $S = 0.6 \pm 0.1$ mVK^{-1},

which is over an order of magnitude larger than has been observed in STM break junctions with metal electrodes [103].

However, this does not equate to a similar increase in thermoelectric efficiency. This is because the strength of the tunnel coupling increases the conductance of the device while decreasing the Seebeck coefficient. In this device the tunnel coupling is observed to be 27 times smaller than the value for which it is calculated that thermoelectric efficiency would be maximised, giving rise to the high Seebeck coefficient which is observed at the expense of poor conductance [106]. In order to increase the tunnel coupling it will be necessary to find a way to preserve the conjugation of the fullerene molecule into the functional groups. One way in which this would be possible would be to incorporate a transition metal into the functional group in order to create overlap between the metal d-orbitals and the fullerene conjugated system [108]. If this were done then it may be possible to create single molecule devices with significantly greater thermoelectric efficiencies than are observed in inorganic devices.

5.5 Distribution of Fullerenes on Graphene

The fact that the fullerenes, let alone pyrene fucntionalized fullerenes, bind to the surface of graphene through π-π stacking interactions is well known. However, the exact orientation of the molecules of the surface is not known. In all of the elec-

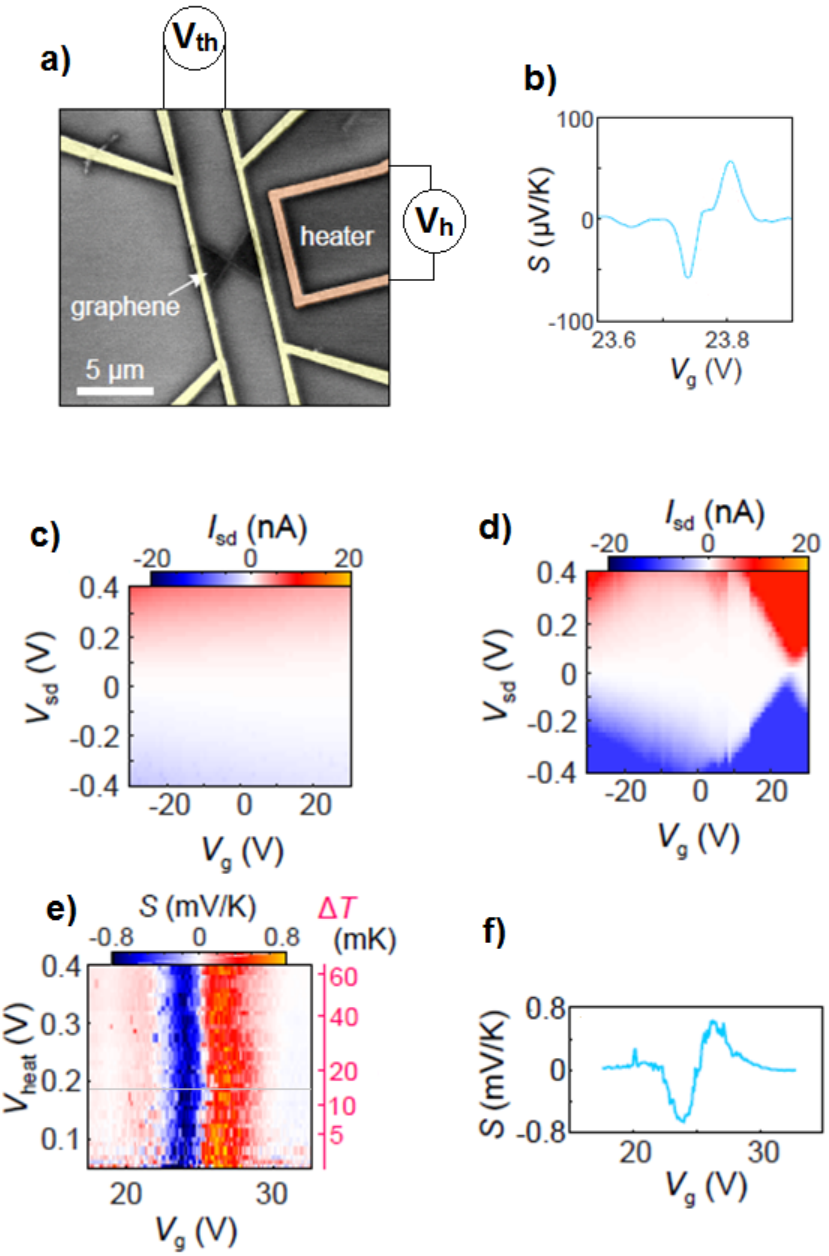

Figure 34: a) False colour SEM micrograph of the device being measured showing the graphene nanoribbon, metal contacts and Au micorheater. b) Measured Seebeck coefficient for the empty graphene nanogap. c) And d) show 77 K stability measurements of the empty and fullerene filled nanogap, respectively. e) Seebeck coefficient for the fullerene containing device at a range of applied voltages to the microheater, which gives rise to a temperature difference, ΔT, across the device. Also shown is the line profile f) for $\triangle T = 16$ mK.

tron transport measurements on different devices we see similar values of current, implying that the transport is taking place through a single molecule in each case. If the transport was taking place through several fullerenes bridging the graphene nanogap I would expect there to be a different number of molecules bridging the gap in each device, and so a very different current would be observed in each device, which is not the case. Members of the group wanted to understand the distribution of functionalized fullerene molecules drop-cast on a graphene surface. While this is the not the exact situation described above, there may be similarities. In order to perform these measurements a solution of the bis-functionalized fullerenes were drop cast onto graphene from a solution of molecules of concentration 1 μM in toluene and allowed to air-dry in a fume hood.

These samples were then studied by atomic force microscopy (AFM), with images taken from these measurements displayed in Figure 35 a and b. These measurements were taken using a Nanoscope III MultiMode atomic force microscope with MikroMasch HQ:NSC15/AL BS probes using the tapping mode. In image 32 a it is possible to observe the fullerenes as small dark spots, which are evenly distributed across the graphene, with an average distance between fullerenes of 75 ± 25 nm. No preference is observed for defects in the graphene. By taking a closer look at the fullerenes on the surface it is possible to see that the fullerenes form small clusters with an average diameter of 15 ± 10 nm. If this were the case then all measurements would be looking at small clusters of fullerene molecules

as opposed to individual molecules. However, as the clusters are well separated and the size seen for the small clusters is very regular it is not outside of the realms of possibility that there are single, well separated molecules on the surface. These appear to be clusters due to convolution of the image with a tip that is approximately 15 nm wide at the point closest to the sample, which is not dissimilar to the typical radius of the MikroMasch tip of 8 nm . There are also some important differences between the deposition and environment of the fullerenes between these AFM measurements and those in the nanogap devices. Firstly, the fullerenes in the nanogap devices were dipped into a 10^{-6} M solution of fullerenes in chloroform and then immediately dried with a nitrogen gun. Both the act of dipping and drying will act to reduce the number of fullerenes on the graphene surface, making it more likely that they will be present as individual molecules. Secondly, in the nanogap devices, there is a gap in the graphene, allowing both of the pyrene anchor groups to contact the graphene while the fullerene does not. This creates a different environment for the molecules, which before could only have a single pyrene unit bind to the graphene, leaving one pyrene unit available to interact with a pyrene unit in subsequent functionalized fullerene molecule, leading to aggregation.

While these measurements provide some information about the binding of pyrene functionalized molecules to graphene in general, it is regrettably of limited use in determining the binding of pyrene functionalized fullerenes in a graphene

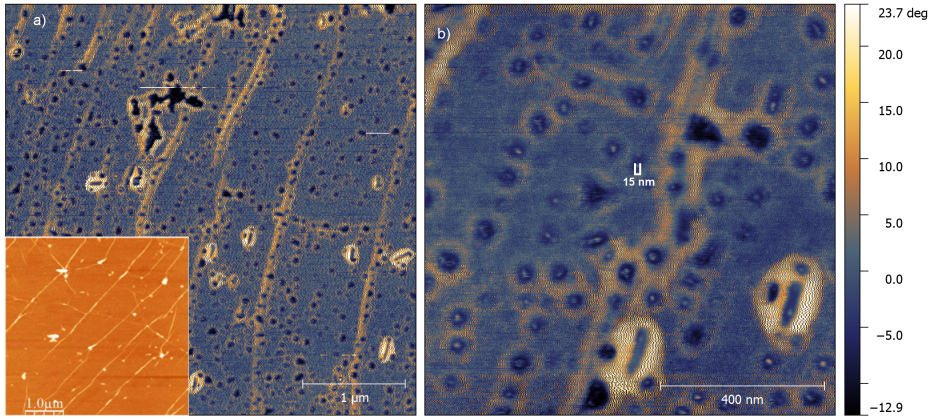

Figure 35: a) The functionalized fullerene molecules distributed across a graphene sheet, inset: AFM of the pristine graphene, showing very widely distributed large spots of impurity. b) A close up of the fullerene molecules showing that they form aggregates of between 10 and 20 nm wide separated by an average of 75 nm.

nanogap device.

5.6 Towards Endohedral Fullerenes

As interesting as the results that have been obtained by studying the fullerene C_{60} are, this is the most abundant fullerene with the best known properties and has had its electrical transport properties studied previously in STM break junctions [109]. Experiments on the more exotic higher fullerenes and endohedral fullerenes would therefore be of greater value, allowing us to determine the electrical transport properties of some molecules for the very first time. Although these experiments have not been carried out, there are some electron transport properties that can be inferred from the electron transport properties of C_{60} and from the known properties of the higher and endohedral fullerenes.

When looking at heavier fullerene molecules of a different size, whether endohedral or empty cages, there will be a significant change to the vibrational modes of the molecule compared to C_{60}. For the empty higher fullerenes there are significantly more vibrations possible, due to the number of chemical bonds and reduced symmetry, and these vibrations primarily occur at at a lower energy, due to the increased mass of the higher fullerenes compared to C_{60} [110]. For the same reason, centre of mass oscillations of the fullerene between the pyrene anchor groups will also decrease in energy, making the quantised nature of the gap between coulomb diamonds less obvious. On moving to endohedral fullerenes the majority of the vibrational spectrum remains identical. However, a number of new vibrational modes appear at very low energies, typically tenths of an electron volt. These are assigned as stretch and deformation modes of the encapsulated species and the fullerene cage together as opposed to the relatively unchanged vibrational modes of the fullerene cage alone [110].

While these changes in the vibrational spectrum, which could be observed through Franck-Condon blockade, would provide evidence for which fullerene cage was under examination in the graphene nanogap, it is possible to improve on this method of identification when moving to the endohedral fullerenes. As mentioned in Chapter 2.5, the endohedral fullerene $Sc_3C_2@C_{80}$ is highly spin active, with unpaired electrons on the endohedral cluster as well as a nuclear spin of $I = 7/2$ on each of the scandium atoms. While much of this spin is localised within the

fullerene cage, it is still likely that electrons in molecular orbitals of the molecule will couple to these different spins, allowing for a number of interesting experiments to be performed. By applying a strong magnetic field to the sample it will be possible to polarise the nuclear spin of the scandium atoms, opening up an energy difference between electron states on the fullerene molecule where the electron spin is aligned parallel or anti-parallel to the nuclear spin. This can then be used to perform spin to charge conversion to determine the direction of the electron spin relative to the nuclear spin, see Figure 36.

This is just one such experiment which could be carried out. With such a rich spin system placed into an electrical circuit I would expect there to be a huge wealth of magnetic field dependent measurements that could be explored, the true extent of which will not be apparent until the these measurements are realised. Assuming that these measurements are successful there are then a host of spin active fullerenes with exciting properties which could be explored, ranging from gadolinium containing molecules which have been shown to be powerful MRI contrast agents [20] to mixed metal fullerenes which display single-molecule magnetism [112].

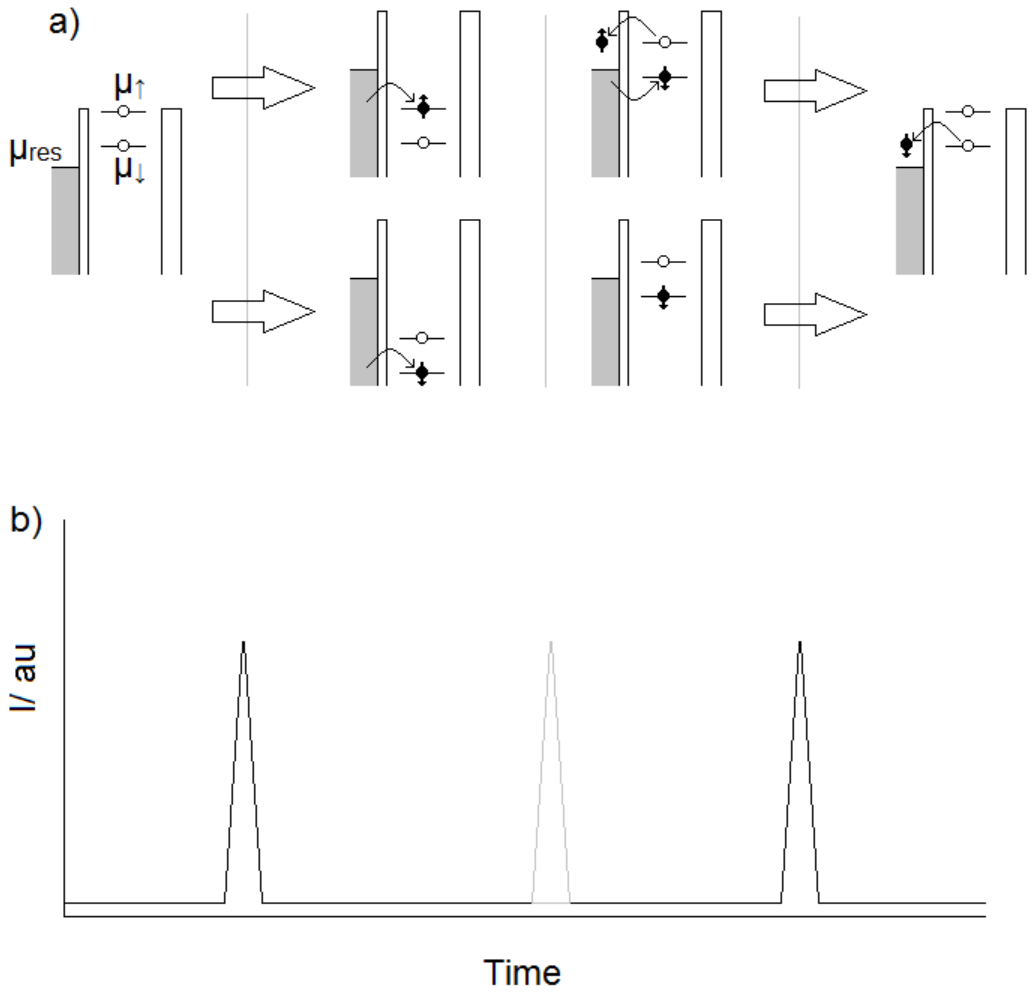

Figure 36: a) The energy scheme for spin read out, showing how one electron spin state is at a higher energy. By careful manipulation of the chemical potential of the reservoir it is possible to determine the spin of the inserted electron using the method in b). b) Shows that there will be an additional current peak if a spin anti-parallel electron is placed on the molecule, allowing us to determine which spin was present.

6 Final Comments and Conclusion

Fullerenes show vast potential for applications in single molecule electronics. This is both due to the fact that it has been shown that fullerenes can undergo a plethora of chemical reactions [2, 3, 4] to alter their physical and chemical properties and there is a wide range of intrinsic properties to be found in different endohedral fullerenes. The potential of fullerenes is particularly apparent when they are combined with other carbon nanomaterials, allowing for non-covalent interactions to be used to build up devices from their individual components, dramatically reducing the requirements for contacting single molecules relative to STM or break-junction based methods, as well as creating an immediate pathway to the scalable production of devices.

In this thesis I have successfully functionalized several empty cage fullerenes in addition to an endohedral fullerene. The reaction on the most abundant cage, C_{60}, was thoroughly investigated leading to integrated rate laws for the formation of the mono and bisadducts, allowing for the reaction conditions to be optimised for the production of bisadducts for use in graphene nanogap devices. Additionally, a comprehensive study of the regioisomerism of the reaction was carried out. The results of this study concluded that there was a dramatic steric influence caused by the pyrene unit. In contrast to multiple reactions with less sterically bulky reagents, which favour the formation of the trans-3 or cis-3 isomer, this reaction favoured the formation of isomers where the two pyrene units were well separ-

ated around the cage, in particular the trans-1 isomer. This reaction produced several molecules which were new to science, allowing for novel studies of the photochemical properties of functionalized empty cage fullerenes. These studies showed that there was an opposite effect seen in the mono and bisadducts of the two fullerenes C_{60} and C_{70} when functionalized with pyrene. These differences were attributed to the effect of the fullerene cage size on the formation of locally excited or charge separated states, leading to dramatically different results for the sensitising of the toxic singlet oxygen radical. This affect on singlet oxygen generation could have dramatic implications for the incorporation of fullerenes into biotechnology. Fullerenes in and of themselves are not toxic, while radical groups are, this discovery could allow for fullerenes with exceptionally low toxicity to be produced. While the existence of charge-separated triplet states is suggested as a mechanism by which the C_{60} bisadduct and C_{70} monoadduct sensitise singlet oxygen, it would be useful to further confirm this hypothesis. One way in which this could be done is to perform DFT calculations on the four molecules. This would give information about the favourability of the triplet state in each of the fullerene mono and bisadducts as well as the distribution of electron density in these states to confirm that they are indeed charge separated excimers. Additionally, such experiments would give the energy and so the emission energy of each molecular orbital, providing a way to test the validity of the results and allowing us to better characterise the features observed in PL spectroscopy. I would suggest

using a hybrid functional approximation such as B3LYP which has been used to successfully study the molecular orbitals in the C_{60} monoadduct previously [113].

In addition to their properties, these molecules are specifically synthesised such that they can self-assemble into a graphene nanogap, allowing for the study of single-molecule electronics in a unique environment. This work lays the foundations for a range of functionalized molecules targeted to self-assemble into graphene nanogaps, with an emphasis on functionalized fullerenes. While molecular engineering, the creation of a molecule for a specific purpose, is still in its infancy, there are severeal key steps taken in this thesis to realise that goal. Firstly, a bisfunctionalized fullerene was produced, which can self-assemble into the graphene nanogap. Secondly, the kinetics of the reaction were studied to optimise the production of the useful bisadduct over the monoadduct or higher adducts. Finally, this reaction shows some regioisomeric control, with the reaction favouring the formation of the trans-1 isomer. By showing that different functional groups can affect the regioisomeric yield it is possible that a reaction could be designed to optimise the yield of a particular regioisomer for incorporation into graphene nanogap devices.

Having produced the molecules necessary for single molecule electronics, I then showed that RF circuits which I have built are capable of making the sensitive measurements necessary to detect single electron states. The circuits that I built then went on to be used to measure such states in GaAs quantum dots, demon-

strating their suitability for single molecule electronics. Finally, the molecules which I have produced were combined with the circuits that I have built in order to carry out electrical measurements on single molecules. The measurements were able to provide overwhelming evidence that a C_{60} molecule was present in the gap through the observation of vibrational excited states, showing good agreement between the energy of these states observed in the transport measurements and a range of other measurement techniques. Finally, an application is presented for the molecules that I have produced, showing the possibility for these molecules to be used in energy generation due to their unusual electronic properties.

However, there are clearly still advances to be made in order to unlock the full potential of fullerenes for use in single molecule electronics. Holding back these devices to the greatest extent is the lack of control over the interaction between the fullerene and the graphene electrode, leading to a lack of reproducibility in the results that are measured. There are several strategies for improving these devices by improving the graphene nanogaps, which are outside of the scope of this thesis. It would be interesting to explore a greater range of functional groups attached to the fullerene to determine if there is anything to be gained by moving to a covalent bond between the fullerene and the graphene. Previous studies have already shown that there is little to be gained in attractive interactions by moving between different sized conjugated systems [114]. However, different functional groups can have a major impact on the molecular orbitals of a molecule,

leading to fine-tuning of the coupling between the relevant molecular orbits in the functionalized fullerene molecule and the graphene electrodes. By moving to a covalent system, such as linking the two materials by an esterification reaction [115], it is expected that there will be significantly greater coupling between the fullerene and the electrodes. This will lead to different conductance behaviours, although it is also likely to reduce the long lifetime vibron states which make the system so appealing for use in thermoelectrics.

It was also not possible to extend the full range of chemical functionalization techniques to the endohedral fullerenes in this thesis, making it impossible to explore magnetic properties in single-molecule devices. Not only would this improve the range of molecular orbitals which can interact with the graphene electrodes, it would also lead to experiments which would show further direct evidence for the presence of specific molecules in the graphene nanogap. It would be exceptionally time consuming to perform an exhaustive study of endohedral fullerenes and possible anchor groups to find those that produce the best quality devices. Therefore, it would be essential to conduct thorough DFT modelling of functionalized fullerene molecules to determine those with promising properties for various applications. For the case of thermoelectric devices, this would be finding a molecule with molecular orbitals that had a greater electron density in the functional groups for a stronger coupling with the graphene, and so an improved electrical conductance, while retaining poor vibron transport through the

molecule, a desirable property from the pyrene functionalized C_{60}.

There is huge potential in the field of molecular electronics to find devices with properties that are simply not found in conventional electronics. However, to realise these properties there needs to be a concerted and interdisciplinary effort to go from identifying promising candidate molecules to their synthesis and incorporation into devices. While this field is in its infancy, it is my firm belief that there are huge gains to be made which would lead to a plethora of exciting technological advances.

References

[1] H. W. Kroto, J. R. Heath, S. C. O'Brien, R. F. Curl, R. E. Smalley, Nature, 1985, 318, 162 - 163

[2] M. Maggini, G. Scorrano, M. Prato. J. Am. Chem. Soc. 1993, 115 (21): 9798 - 9799

[3] C. Bingel, Chemische Berichte., 1993, 126 (8): 1957

[4] B. Kräutler, J. Maynollo, Tetrahedron, 1996, 52 (14), 5033–5042

[5] T. Akasaka, T. Kato, K. Kobayahi, S. Nagase, K. Yamamoto, H. Funasaka, T. Takahashi, Nature, 1995, 374, 600 – 601

[6] Y. Maeda, J. Miyashita, T. Hasegawa, T. Wakahara, T. Tsuchiya, L. Feng, Y. Lian, T. Akasaka, K. Kobayashi, S. Nagase, M. Kako, K. Yamamoto, K. M. Kadish, J. Am. Chem. Soc., 2005, 127, 2143-2146

[7] Dietel E, A. Hirsch, B. Pietzak, M. Waiblinger, K. Lips, A. Weidinger, A. Gruss, K.-P. Dinse, J. Am. Chem. Soc., 1999, 121, 2432

[8] R. Bolskar, A. Benedetto, L. Husebo, R. E. Price, E. F. Jackson, S. Wallance, L. J. Wilson J. Am. Chem. Soc., 2003, 125, 5471–5478

[9] S. Zhou, I. Rašović , G. A. D. Briggs, K. Porfyrakis, Chem. Comm., 2015, 51, 7096-7099

[10] E. B. Iezzi, J. C. Duchamp, K. R. Fletcher, T. E. Glass, H. C., Nano Lett., 2002, 11 (2), 1187–1190

[11] Y. Maeda, J. Miyashita, T. Hasegawa, T. Wakahara, T. Tsuchiya, T. Nakahodo, T. Akasaka, N. Mizorogi, K. Kobayashi, S. Nagase, T. Kato, N. Ban, H. Nakajima, Y. Watanabe, J. Am. Chem. Soc., 2005, 127, 12190-12191

[12] Z. Ge, J. C. Duchamp, T. Cai, H. W. Gibson, H. C. Dorn, J. Am. Chem. Soc., 2005, 127, 16292– 16298

[13] L. Franco, S. Ceola, C. Corvaja, S. Bolzonella, W. Harneit, M. Maggini, Chem. Phys. Lett., 2006, 422, 100–105

[14] P. Dallas, G. Rogers, B. Reid, R. A. Taylor, H. Shinohara, G. A. D. Briggs, K. Porfyrakis. Chem. Phys., 2016, 465-466:28-39

[15] Y.-P. Sun, P. Wang, N. B. Hamilton, J. Am. Chem. Soc., 1993, 115, 6378

[16] Y. He, Y. Li. Phys. Chem. Chem. Phys., 2011, 13, 1970

[17] J. De Ceuster, E. Goovaerts, A. Bouwen, J. C. Hummelen, V. Dyakonov, Phys. Rev. B, 2001, 64, 195206

[18] M. A. Green, K. Emery, Y. Hishikawa, W. Warta, E. D. Dunlop, Prog. Photovoltaics: Res. Appl., 2015, 23, 805

[19] S. K. Sharma, L. Y. Chiang, M. R. Hamblin, Nanomedicine (Lond)., 2011, 6(10): 1813–1825

[20] M. Mikawa, H. Kato, M. Okumura, M. Narazaki, Y. Kanazawa, N. Miwa, H. Shinohara, Bioconjug Chem., 2001, 12(4), 510–4

[21] D. M. Guldi, B. M. Illescas, C. M. Atienza, Chem. Soc. Rev., 2009, 6, 1587-1597

[22] J. J. L. Morton, A. M. Tyryshkin, A. Ardavan , S. C. Benjamin, K. Porfyrakis, S. A. Lyon, G. A. D. Briggs, phys. stat. sol. (b), 2006, 243(13), 3028–3031

[23] C. S. Allen, G. Liu, Y. Chen, A. W. Robertson, K. He, K. Porfyrakis, J. Zhang, G. A. D. Briggs, J. H. Warner, Nanoscale, 2014, 6(1), 572–80

[24] C. S. Lau, H. Sadeghi, G. Rogers, S. Sangtarash, P. Dallas, K. Porfyrakis, J. Warner, C. J. Lambert, G. A. D. Briggs, J. A. Mol, Nano Lett., 2016, 16 (1), pp 170–176

[25] N. J. Tao, Nat. Nanotechnol., 2006, 1, 173–81

[26] D. Xiang, H. Jeong, T. Lee, D. Mayer, Adv. Mater., 2013 25, 4845–4867

[27] M. Tsutsui, M. Taniguchi, Sensors (Basel)., 2012 12, 7259–98

[28] A. R. Champagne, A. N. Pasupathy, D. C. Ralph, Nano Lett., 2005 5, 305–8

[29] C. Durkan, "Current at the Nanoscale :An Introduction to Nanoelectronics" (Imperial College Press, Cambridge, 2007), p.185-192. ISBN: 1-86094-823-5

[30] S. C. Benjamin, A. Ardavan, G. A. D. Briggs, D. A. Britz, D. Gunlycke, J. Jefferson, M. A. G. Jones, D. F. Leigh, B. W. Lovett, A. N. Khlobystov, S. A. Lyon, J. J. L. Morton, K. Porfyrakis, M. R. Sambrook, A. M. Tyryshkin, J. Phys.: Condens. Matter, 2006, 18, S867–S883

[31] A. F. Ioffe, "Semiconductor Thermoelements, and Thermoelectric Cooling" (Infosearch, London, 1957), p. 15, ISBN: 0-85086-039-3

[32] J.P. Heremans, M. S. Dresselhaus, L. E. Bell, D. T. Morelli, Nat. Nano., 2013, 8, 471–473

[33] L. Rincón-García, C. Evangeli, G. Rubio-Bollingerac, N. Agraït, Chem. Soc. Rev., 2016, 45, 4285–4306

[34] K. Kordatos, S. Bosi, T. Da Ros, A. Zambon, V. Lucchini, M. Prato. J. Org. Chem., 2001, 66, 2802-2808

[35] M. R. Ceron, M. Izquierdo, A. Aghabali, J. A. Valdez, K. B. Ghiassi, M. M. Olmstead, A. L. Balch, F. Wudl, L. Echegoyen. J. Am. Chem. Soc., 2015, 137(23):7502-7508

[36] A. Hirsch, I. Lamparth, H. R. Karfunkel. Angew. Chem. Int. Ed., 1994, 33, 437

[37] P. W. Atkins, J. de Paula, "Physical Chemistry" (8th edition, Oxford University Press, Oxford, 2006), p.811. ISBN: 019-8700725

[38] Q. Lu, D. Schuster, S. Wilson. J. Org. Chem., 1996, 61, 4764-4768

[39] D. Milic, M. Prato. Eur. J. Org. Chem., 2010, 476-483

[40] N. Chen, L. Z. Fan, K. Tan, Y. Q. Wu, C. Y. Shu, X. Lu,C. R. Wang, J. Phys. Chem. C, 2007, 111, 11823

[41] J. R. Pinzon, D. C. Gasca, S. G. Sankaranarayanan, G. Bottari, T. Torres, D. M. Guldi, L. Echegoyen, J. Am. Chem. Soc., 2009, 131, 7727

[42] S. Aroua, Y. Yamakoshi, J. Am. Chem. Soc., 2012, 134, 20242

[43] T. Wang, J. Wu, Y. Feng, Y. Ma, L. Jiang, C. Shu, C. Wang, Dalton Trans., 2012, 41, 2567

[44] C. Thilgen, F. Diederich, Chem. Rev., 2006, 106(12):5049-5135

[45] K. Kordatos, T. Da Ros, M. Prato, R.V. Bensasson, S. Leach, Chem. Phys., 2003, 293(2):263-280

[46] Y. Nakamura, K. O-kawa, M. Matsumoto, J. Nishimura, Tetrahedron, 200, 56:5429-5434

[47] T. Wang., J. Wu, W. Xu, J. Xiang, X. Lu, B. Li , L. Jiang., C. Shu , C. Wang, Ang. Chem. Int. Ed, 2010, 49: 1786–1789

[48] H. Shinohara, H. Sato, M. Ohkohchi, Y. Ando, T. Kodama, T. Shida, T. Kato, Y. Saito, Nature 1992, 357, 52–54

[49] L. Echegoyen, C. J. Chancellor, C. M. Cardona, B. Elliott, J. Rivera, M. M. Olmstead, A. L. Balch, Chem. Commun. 2006, 2653–2655

[50] C. M. Cardona , B. Elliott , L. Echegoyen, J. Am. Chem. Soc., 2006, 128 (19), 6480–6485

[51] R. Sijbesma, G. Srdanov, F. Wudl, J.A. Castoro, C. Wilkins, S. H. Friedman, D. L. DeCamp, G. L. Kenyon. J. Am. Chem. Soc., 1993, 115, p. 6510

[52] M. Gallego, J. Calbo, J. Arago, M.R.K. Calderon, F. H. Liquido, T. Iwamoto, A. K. Greene, A. A. Jackson, E. M. Perez, E. Orti, D. M. Guldi, L. T. Scott, N. Martin. Angew. Chem. Int. Ed., 2014, 53, p. 2170

[53] M. B. Zimmt, D. H. Waldeck. J. Phys. Chem. A, 2003, 107, p. 3580

[54] A. Kahnt, J. Karnbratt, L.J. Esdaile, M. Hutin, K. Sawada, H.L. Anderson, B. Albinsson. J. Am. Chem. Soc., 2011, 133, p. 9863

[55] I.D. Petsalakis, G. Theodorakopoulos. Chem. Phys. Lett., 2008, 466, p. 189

[56] C. K. Tai, W. Y. Hsieh, P. L. Yeh, H. L. Chiu, B. C. Wang. J. Chin. Chem. Soc., 2013, 60, p. 251

[57] T. Numata, T. Murakami, F. Kawashima, N. Morone, J. E. Heuser, Y. Takano, K. Ohkubo, S. Fukuzumi, Y. Mori, H. Imahori. J. Am. Chem. Soc., 2012, 134, p. 6092

[58] J. W. Aborgast, A. P. Darmanyan, C.S. Foote, F. N. Diederich, Y. Rubin, F. Diederich, M. Alvarez, S. J. Anz, R. L. Whetten. J. Phys. Chem. 1991, 95, p. 11

[59] T. Ozben. J. Pharm. Sci., 2007, 96 (9): 2181–96

[60] D. M. Guldi, F. Spanig, D. Kreher, I. F. Perepichka, C. Van der Pol, M. R. Bryce, K. Ohkubo, S. Fukuzumi. Chem. Eur. J. 2008, 14, p. 250

[61] S. D. Snow, J. Lee, J.-H. Kim. Environ. Sci. Technol. 2012, 46, 13227−13234

[62] L. Pineiro, M. Novo, W. Al-Soufi. Adv. Colloid. Interface Sci. 2015, 215, p. 1

[63] M. B. Zimmt, D. H. Waldeck. J. Phys. Chem. A. 2003, 107, p. 3580

[64] K. A. Zachariasse, S. I. Druzhinin, S. A. Kovalenko. J. Chem. Phys., 2009, 131, p. 224313

[65] Y. P. Sun, G. E. Lawson, J. E. Riggs, B. Ma, N. Wang, D. K. Moton. J. Phys. Chem. A, 1998, 102, p. 5520

[66] D. M. Guldi, K. D. Asmus. J. Phys. Chem. A., 1997, 101, p. 1472

[67] T. Gareis, O. Kothe, J. Daub. Eur. J. Org. J., 1998, 1549

[68] A. S. D. Sandanakaya, Y. Araki, O. Ito, G. R. Deviprasad, P. M. Smith, L. M. Rogers, M. E. Zandler, F. D. D'Souza. Chem. Phys., 2006, 325, p. 452

[69] F. Liao, Y. Saitoh, N. Miwa. Oncol Res., 2011, 19(5): 203-16

[70] B. P. Karsten, R. K. M. Bouwer, J. C. Hummelen, R. M. Williams, R. A. J. Janssen. Photochem. Photobiol. Sci., 2010, 9, p. 1055

[71] R. J. Schoelkopf. Science, 1998, 280, p. 1238

[72] A. Aassime, G. Johansson, G. Wendin, R. J. Schoelkopf, P. Delsing, Phys. Rev. Lett., 2001, 86, 3376

[73] T. Hasler, M. Jung, V. Ranjan, G. Puebla-Hellmann, A. Wallraff, C. Schönenberger, Phys. Rev. Applied, 2015, 4, 054002

[74] B. Xu, N. J. Tao. Science, 2003, 301, p. 1221

[75] T. Müller, B. Küng, S. Hellmüller, P. Studerus, K. Ensslin, T. Ihn, M. Reinwald, W. Wegscheider, Appl. Phys. Lett., 2010, 97, 202104

[76] S. Hellmüller, M. Pikulski, T. Müller, B. Küng, G. Puebla- Hellmann, A. Wallraff, M. Beck, K. Ensslin, T. Ihn, Appl. Phys. Lett., 2012, 101, 042112

[77] N. Ares, F. J. Schupp, A. Mavalankar, G. Rogers, J. Griffiths, G. A. C. Jones, I. Farrer, D. A. Ritchie, C. G. Smith, A. Cottet, G. A. D. Briggs, E. A. Laird, Phys. Rev. Applied, 2016, 5, 034011

[78] D. M. Pozar, "Microwave Engineering" (4th edition, John Wiley and Sons, New York, 2012), p.63. ISBN: 047-0631554

[79] D. T. McClure, P.H.D. dissertation, Harvard University. 2012 (access on 28/03/2014 at http://qdev.nbi.ku.dk/student_theses/pdf_files/McClure_Thesis.pdf)

[80] F. Pobell, "Matter and Methods at Low Temperatures", (Springer, Berlin, 2007). p 70. ISBN: 3-540-46356-9

[81] C. Durkan, "Current at the Nanoscale :An Introduction to Nanoelectronics" (Imperial College Press, Cambridge, 2007), p.185-192. ISBN: 1-86094-823-5

[82] A. Mavalankar, S. J. Chorley, J. Griffiths, G. A. C. Jones, I. Farrer, D. A. Ritchie, C. G. Smith, Appl. Phys. Lett., 2013, 103, 133116

[83] H. Brenning, S. Kafanov, T. Duty, S. Kubatkin, P. Delsing, J. Appl. Phys., 2006, 100, 114321

[84] Y. Meir, N. S.Wingreen, P. A. Lee, Phys. Rev. Lett., 1991, 66, 3048

[85] Ya.M. Blanter, M. Büttiker, Phys. Rep., 2000, 336, 1

[86] S. J. Chorley, J. Wabnig, Z.V. Penfold-Fitch, K. D. Petersson, J. Frake, C. G. Smith, M. R. Buitelaar, Phys. Rev. Lett., 2012, 108, 036802

[87] J. Gabelli, G. Fève, J.-M. Berroir, B. Plaçais,A. Cavanna, B. Etienne, Y. Jin, D. C. Glattli, Science, 2006, 313, 499

[88] K. D. Petersson, C. G. Smith, D. Anderson, P. Atkinson, G. A. C. Jones, D. A. Ritchie, Nano Lett., 2010 10, 2789

[89] J. I. Colless, A. C. Mahoney, J.M. Hornibrook, A. C. Doherty, H. Lu, A. C. Gossard, D. J. Reilly, Phys. Rev. Lett., 2013 110, 046805

[90] J. Stehlik, Y. Y. Liu, C. M. Quintana, C. Eichler, T. R. Hartke, J. R. Petta, Phys. Rev. Applied, 2015, 4, 014018

[91] C. S. Lau, J. A. Mol, J. H. Warner and G. A. D. Briggs, Phys. Chem. Chem. Phys., 2014, 20398–20401

[92] K. Kaasbjerg, K. Flensberg, Nano Lett., 2008, 8, 3809−14

[93] R. Heid, L. Pintschovius, J. M. Godard, Phys. Rev. B: Condens. Matter Mater. Phys., 1997, 56, 5925−5936

[94] S. Bailey, D. Visontai, C. J. Lambert, M. R. Bryce, H. Frampton, D. Chappell, J. Chem. Phys., 2014, 140, 054708

[95] J. Koch, F. Von Oppen, Phys. Rev. Lett., 2005, 94, 206804

[96] J .Koch, F. Von Oppen, Y. Oreg, E. Sela, Phys. Rev. B: Condens. Matter Mater. Phys., 2004, 70,1−12

[97] Y. Kim, W. Jeong, K. Kim, W. Lee, P. Reddy, Nat. Nano., 2014, 9, 881−885

[98] P. Reddy, S.-Y. Jang, R. A. Segalman, A. Majumdar, Science, 2007, 315, 1568−1571

[99] J. P. Heremans, M. S. Dresselhaus, L. E. Bell, D. T. Morelli, Nat. Nano., 2013, 8, 471–473

[100] R. Venkatasubramanian, E. Siivola, T. Colpitts, B. O'Quinn, Nature, 2001, 413, 597–602

[101] K. Baheti , J. A. Malen, P. Doak, P. Reddy, S.-Y. Jang, T. D. Tilley, A. Majumdar, R. A. Segalman, Nano. Lett., 2008, 8, 715–719

[102] C. Evangeli, K. Gillemot, E. Leary, M. T. González, G. Rubio-Bollinger, C.J. Lambert, and N. Agraït, Nano. Lett., 2013, 13, 2141–2145

[103] S. Y. Yee, J. A. Malen, A. Majumdar, R. A. Segalman, Nano. Lett., 2011, 11, 4089–4094

[104] L. Rincon-Garcia, C. Evangeli, G. Rubio-Bollinger, N Agraït, Chem. Soc. Rev., 2016, 45, 4285–4306

[105] J. P. Small, K. M. Perez, P. Kim, Phys. Rev. Lett., 2003, 91, 256801

[106] P. Gehring, A. Harzheim, J. Spièce, Y. Sheng, G. Rogers, C. Evangeli, A. Mishra, B. J. Robinson, K.s Porfyrakis, J. H. Warner, O. V. Kolosov, G. A. D. Briggs and J. A. Mol. Nano. Lett., 2017, 17 (11), 7055-7061

[107] Y. Kim, W. Jeong, K. Kim, W. Lee, P. Reddy, Nature Nano., 2014, 9, 881–885

[108] D. Soto, R. Salcedo, Molecules, 2012, 17, 7151-7168

[109] C. Joachim, J. K. Gimzewski, R. R. Schlitter, and C. Chavy, Phys. Rev. Lett., 1995, 74, 2102

[110] M. Krause, M. Hulman, H. Kuzmany, P. Kuran, L. Dunsch, T. J. S. Dennis, M. Inakuma, H. Shinohara, J. Mol. Sruct., 2000, 521, 325

[111] S. Thiele, F. Balestro, R. Ballou, S. Klyatskaya, M. Ruben, W. Wernsdorfer, Science, 2014, 344:6188, 1135-1138

[112] R. Westerström, J. Dreiser, C. Piamonteze, M. Muntwiler, S. Weyeneth, H. Brune, S. Rusponi, F. Nolting, A. Popov, S. Yang, L. Dunsch, T. Greber, J. Am. Chem. Soc., 2012, 34 (24), 9840–9843

[113] C. Van Der Pol, *Oligouorene molecular wires in donor-acceptor conjugate*s, Durham theses, Durham University. 2007 Available at Durham E-Theses Online: http://etheses.dur.ac.uk/2451/

[114] S. Bailey, D. Visontai, C. J. Lambert, M. R. Bryce, H. Frampton, D. Chappell, J. Chem. Phys., 2014, 140, 054708

[115] Y. Zhang, L. Ren, S. Wang, A. Marathe, J. Chaudhurib, G. Li, J. Mater. Chem., 2011, 21, 5386

Appendix A

Photo-luminescent spectra

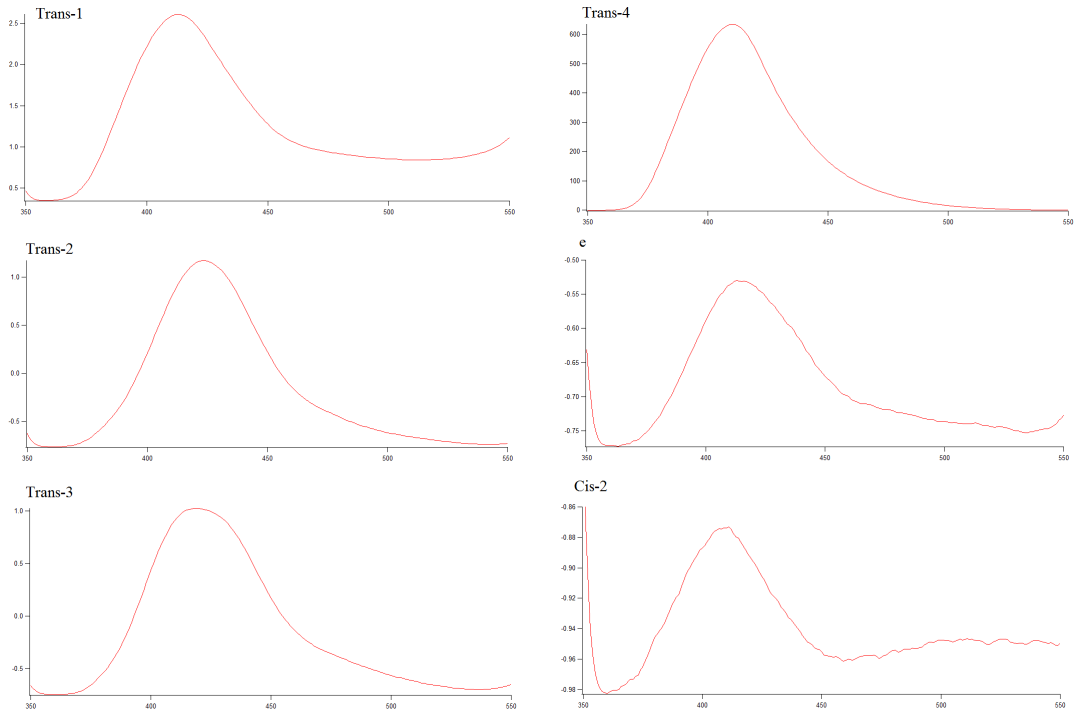

Figure A1: Photo-luminescent (PL) spectra for excitation with 330 nm light, which targets the pyrene group. The spectra are extremely similar for all regio-isomers showing that the pyrene groups are not affected by their relative position on the cage for molecules produced in this reaction.

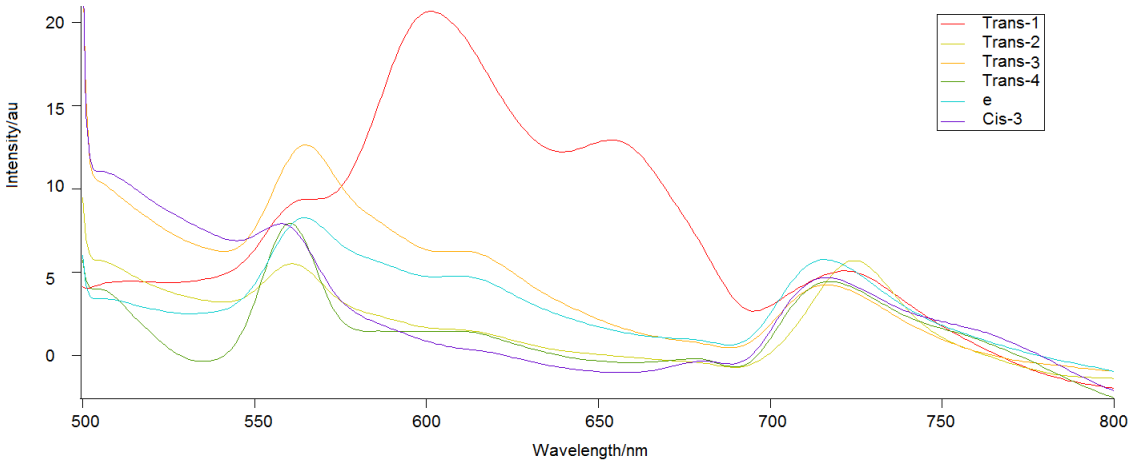

Figure A2: PL spectra for excitation with 480 nm light. This is the optimum excitation wavelength for the fullerene, C_{60} core. The main fullerene emission peak can be seen at $\lambda_{em} \approx 720$nm. The trans-3, trans-4, e and cis-3 show peaks at identical wavelengths. The trans-1 and trans-2 isomers show a peak at slightly longer wavelength. For a simple particle-in-a-box model, this implies a larger area of delocalisation. This can be understood by the pyrene groups being as far apart as possible, and so allowing delocalisation of electrons into these pyrene functional groups to occur to a greater extent.

^{1}H NMR

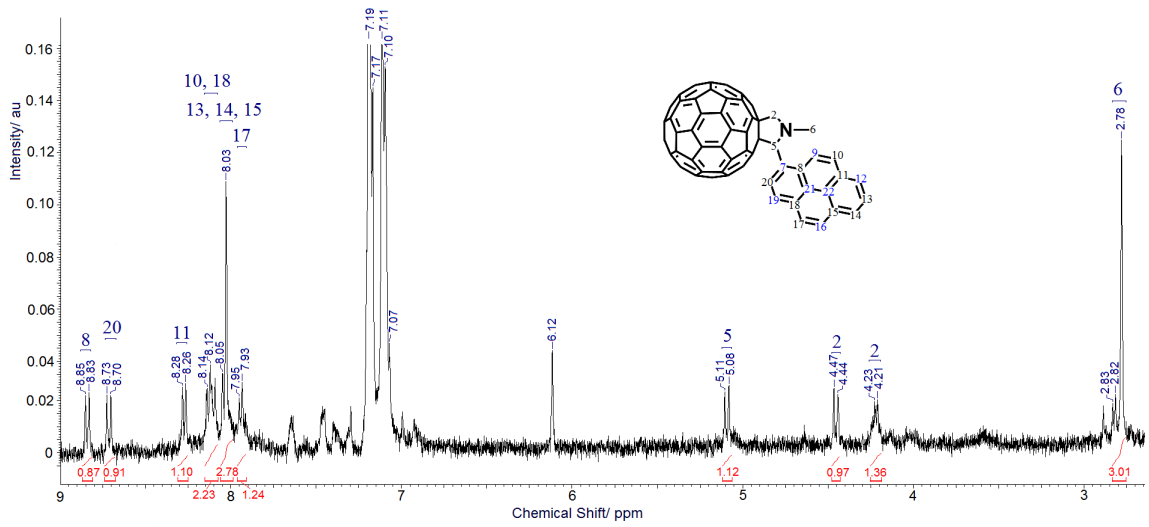

Figure A3: ^{1}H spectra for Monoadduct. For full annotation see main text.

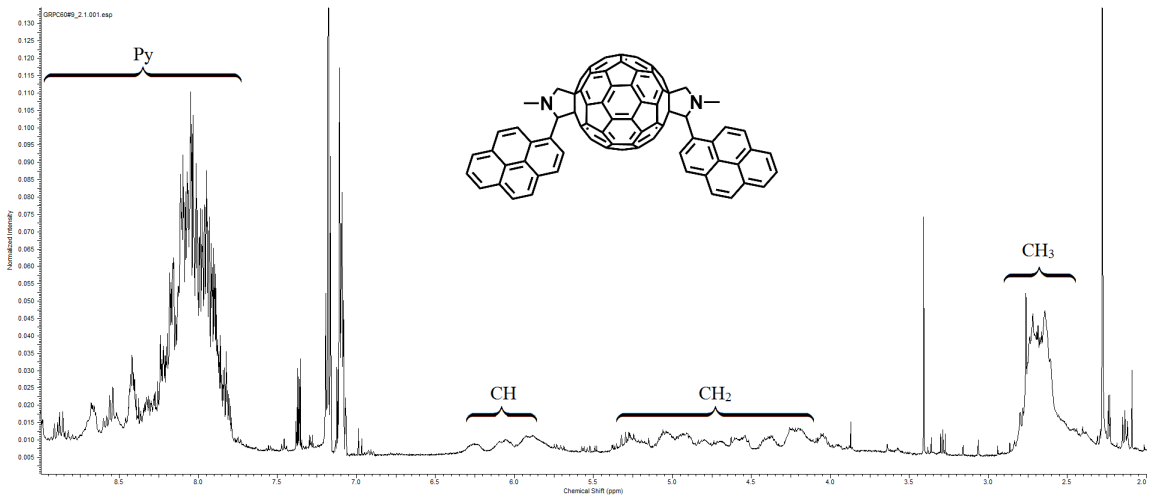

Figure A4: ^{1}H spectra for Trans-2 isomer. For full annotation see main text.

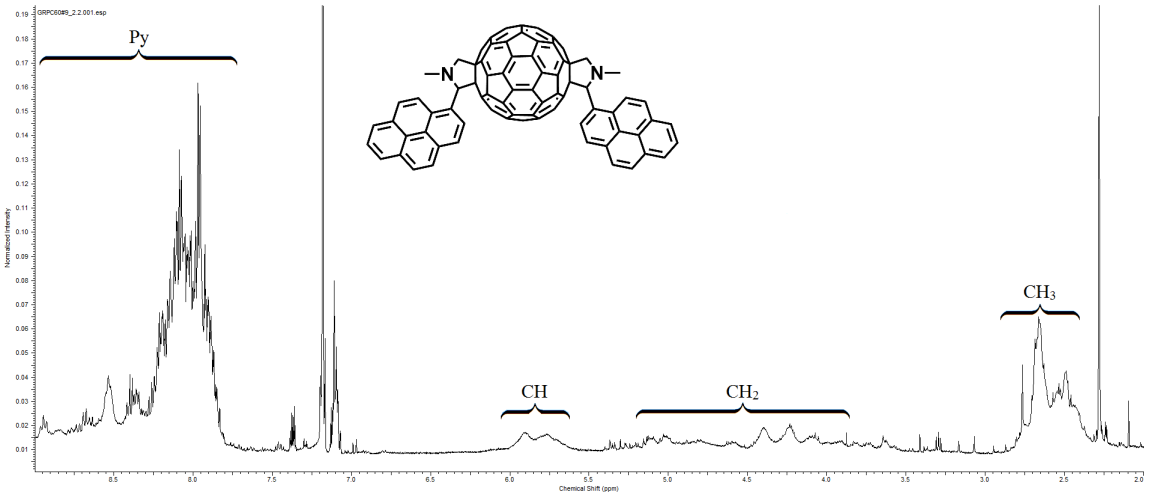

Figure A5: ^{1}H spectra for Trans-3 isomer. For full annotation see main text.

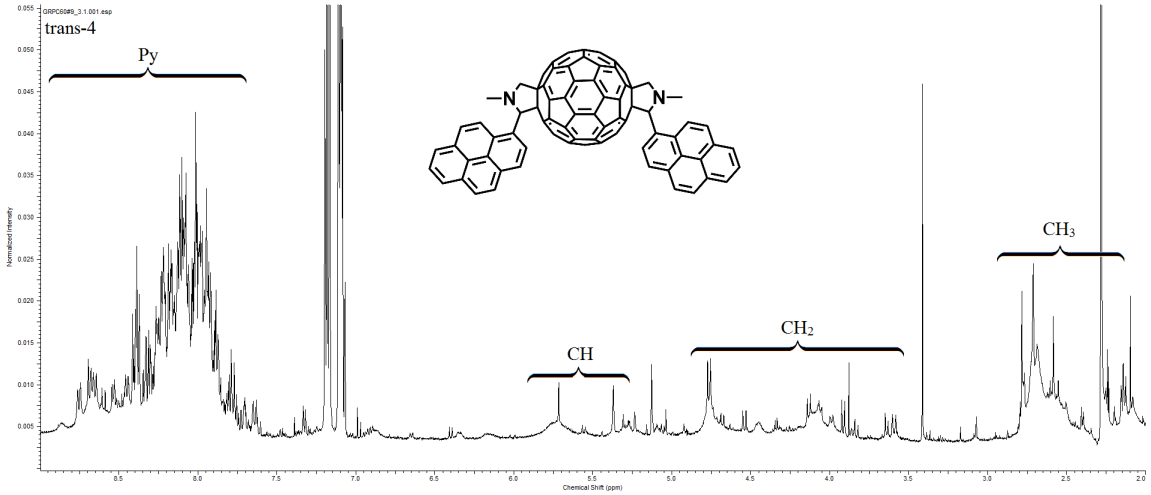

Figure A6: ^{1}H spectra for Trans-4 isomer. For full annotation see main text.

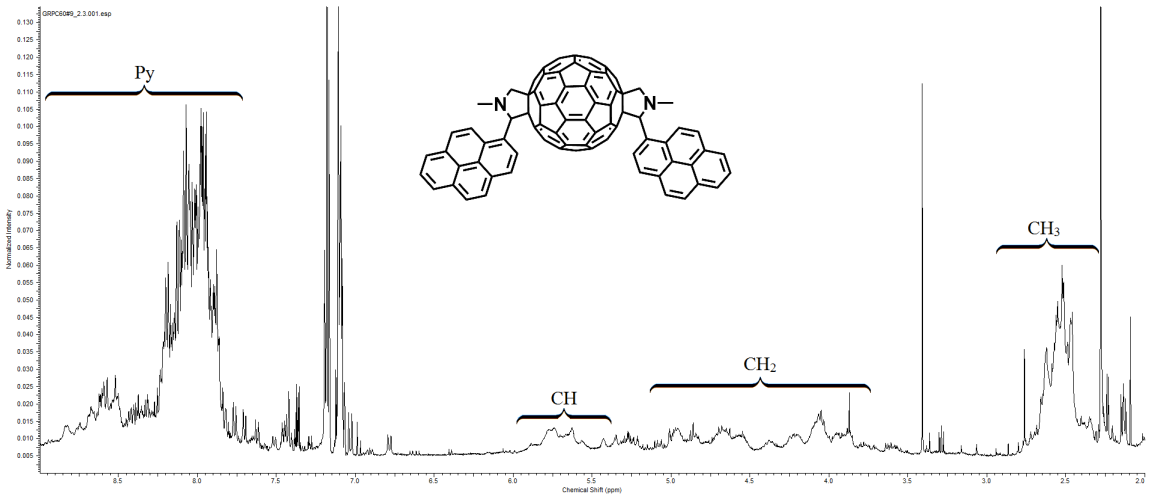

Figure A7: ^{1}H spectra for Equatorial isomer. For full annotation see main text.

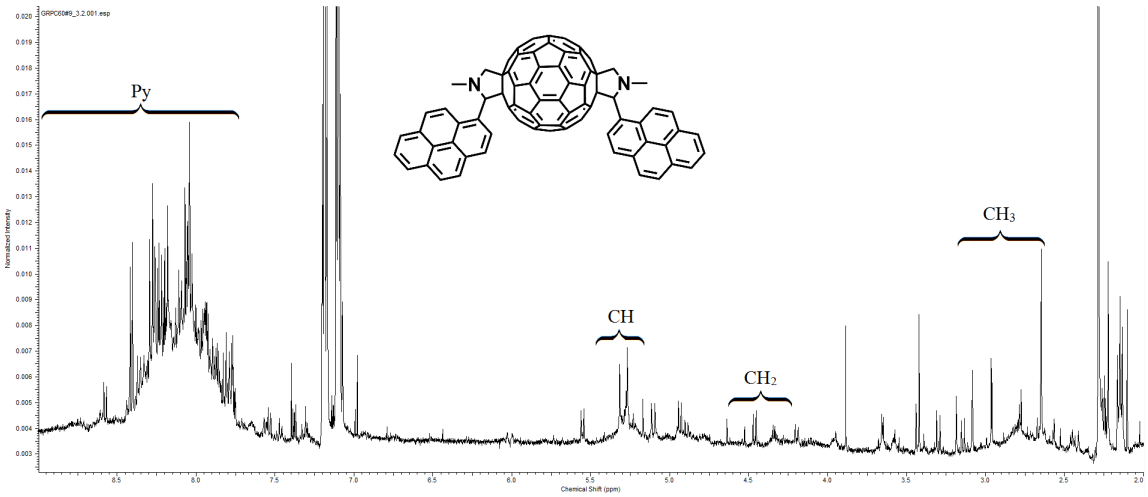

Figure A8: ^{1}H spectra for Cis-3 isomer. For full annotation see main text.

^{13}C NMR

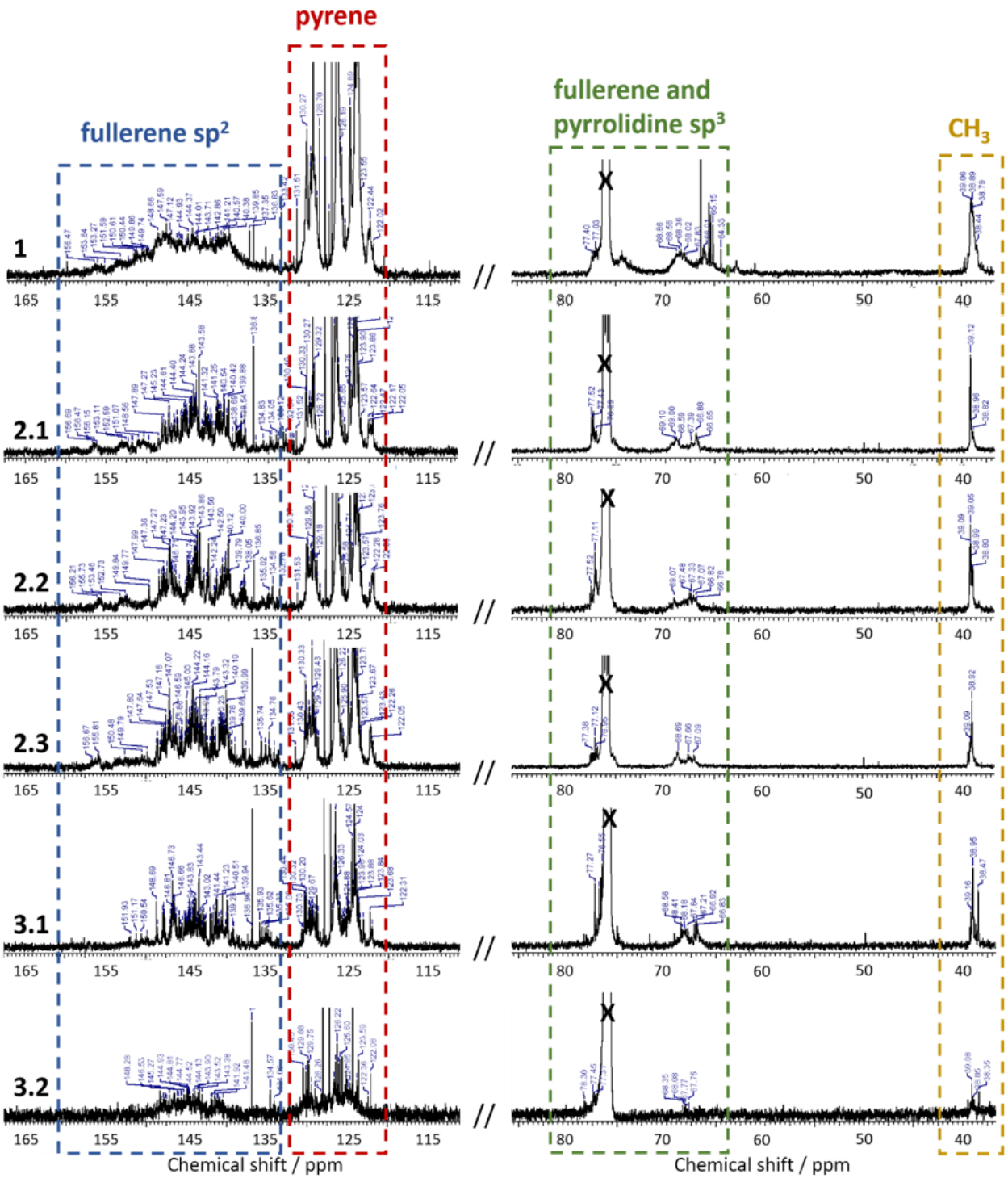

Figure A9: ^{13}C NMR spectra of fractions 1, 2.1, 2.2, 2.3, 3.1 and 3.2, corresponding to trans-1, trans-2, trans-3, trans-4, e-, and cis-3 isomers respectively. Blue box indicates the sp^2 signals corresponding to the fullerene cage, red

box indicates pyrene sp^2 signals, green box shows the region of fullerene sp^3 and pyrrolidine carbons, and yellow box shows the methyl group.

Temperature Studies

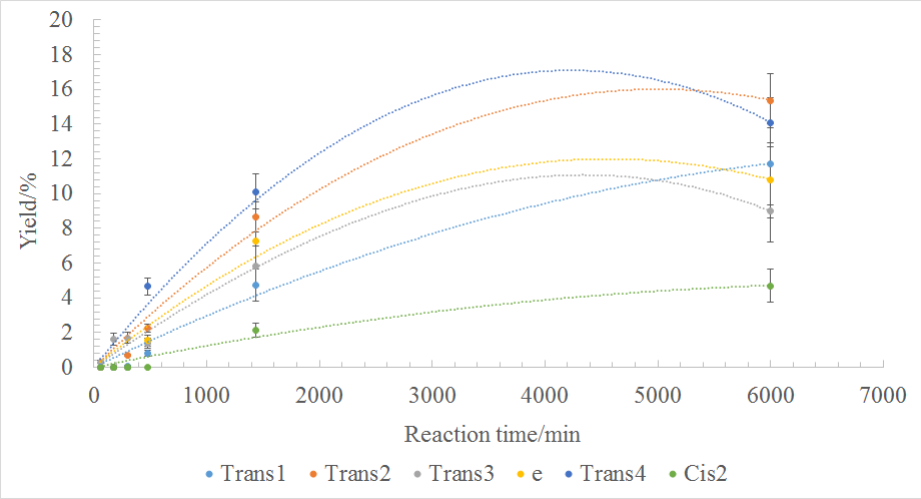

Figure A10: Formation of bis regioisomers at 90°C.

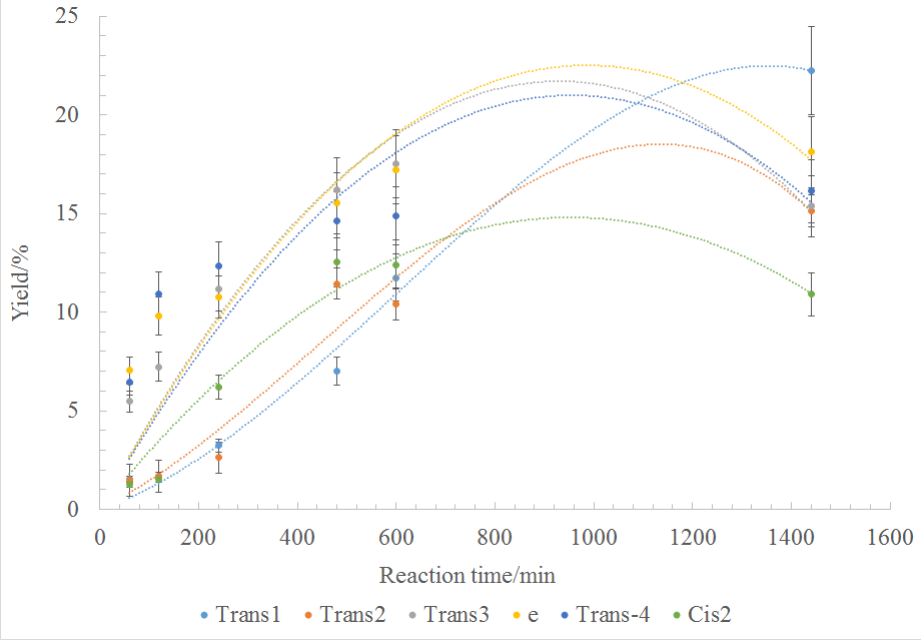

Figure A11: Formation of bis regioisomers at 130°C.

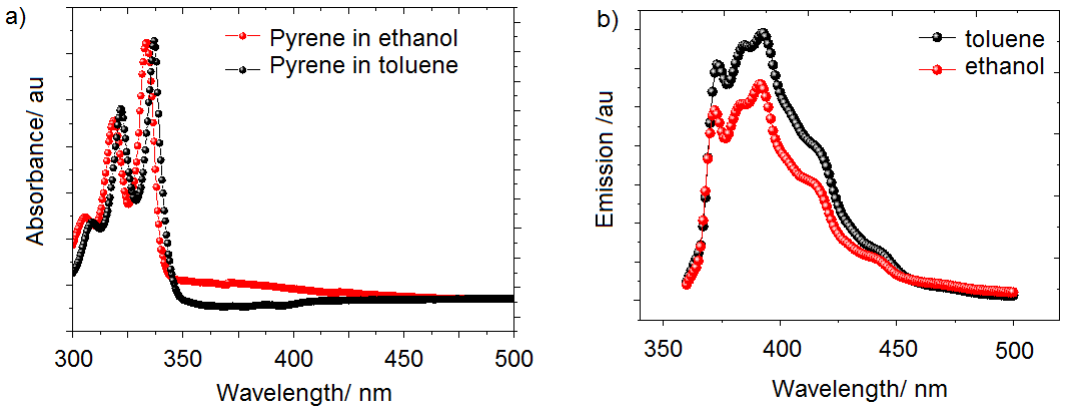

Figure A12: a) absorbance and b) emission spectroscopy of the pyrene-1-carboxaldehyde reagent in both ethanol and toluene, showing very little difference in the spectra between solvents.

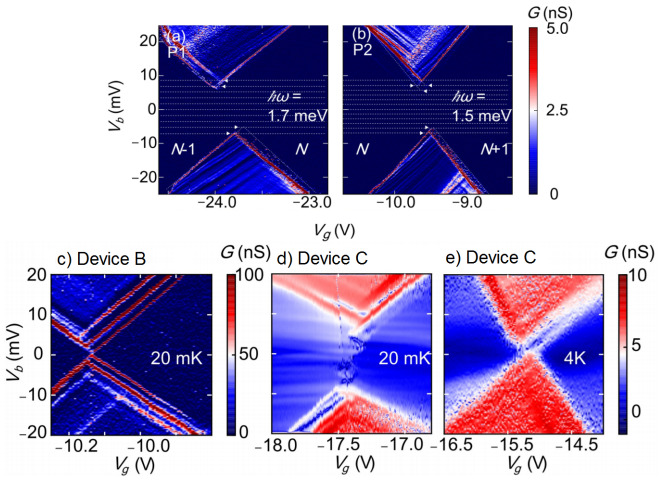

Figure A13: a) and b) Shows the high definition transport spectra for peaks 1 and 2 in device A, the same device as is presented in the main text. These contain both the characteristic fullerene vibrational excited states and current suppression at zero bias. c) Shows a peak in a second device, B, this contains the fullerene vibrational excited states but no current suppression. d) and e) shows a third device, C, in which it is not possible to see the excited states, presumably due to

the additional noise in the spectra. However current suppression at low applied bias voltages which is lifted when the temperature is increased, as in device A, is seen.